

Quantitative Phase Imaging of Magnetic Nanostructures

Using Off-Axis Electron Holography

by

Kai He

A Dissertation Presented in Partial Fulfillment
of the Requirements for the Degree
Doctor of Philosophy

Approved November 2010 by the
Graduate Supervisory Committee:

Martha R. McCartney, Co-Chair
David J. Smith, Co-Chair
Ralph V. Chamberlin
Peter A. Crozier
Jeff Drucker

ARIZONA STATE UNIVERSITY

December 2010

ABSTRACT

The research of this dissertation has involved the nanoscale quantitative characterization of patterned magnetic nanostructures and devices using off-axis electron holography and Lorentz microscopy. The investigation focused on different materials of interest, including monolayer Co nanorings, multilayer Co/Cu/Py (Permalloy, Ni₈₁Fe₁₉) spin-valve nanorings, and notched Py nanowires, which were fabricated via a standard electron-beam lithography (EBL) and lift-off process.

Magnetization configurations and reversal processes of Co nanorings, with and without slots, were observed. Vortex-controlled switching behavior with stepped hysteresis loops was identified, with clearly defined onion states, vortex states, flux-closure (FC) states, and Ω states. Two distinct switching mechanisms for the slotted nanorings, depending on applied field directions relative to the slot orientations, were attributed to the vortex chirality and shape anisotropy. Micromagnetic simulations were in good agreement with electron holography observations of the Co nanorings, also confirming the switching field of 700–800 Oe.

Co/Cu/Py spin-valve slotted nanorings exhibited different remanent states and switching behavior as a function of the different directions of the applied field relative to the slots. At remanent state, the magnetizations of Co and Py layers were preferentially aligned in antiparallel coupled configuration, with predominant configurations in FC or onion states. Two-step and three-step hysteresis loops were quantitatively determined for nanorings with slots perpendicular, or parallel to the applied field direction, respectively, due to the intrinsic coercivity difference and interlayer magnetic coupling between Co and Py layers. The field to reverse both layers was on the order of ~800 Oe.

Domain-wall (DW) motion within Py nanowires (NWs) driven by an *in situ* magnetic field was visualized and quantified. Different aspects of DW behavior,

including nucleation, injection, pinning, depinning, relaxation, and annihilation, occurred depending on applied field strength. A unique asymmetrical DW pinning behavior was recognized, depending on DW chirality relative to the sense of rotation around the notch. The transverse DWs relaxed into vortex DWs, followed by annihilation in a reversed field, which was in agreement with micromagnetic simulations.

Overall, the success of these studies demonstrated the capability of off-axis electron holography to provide valuable insights for understanding magnetic behavior on the nanoscale.

*This dissertation is dedicated to my parents,
who made everything possible.*

ACKNOWLEDGMENTS

I would like to express most sincere thanks to my advisors Professor Martha R. McCartney and Regents' Professor David J. Smith for their esteemed support and guidance that made everything I achieved toward my PhD degree possible. Their open minds, unlimited enthusiasm, precise insights and meticulous attitudes towards doing research have educated me with good characteristics and discipline necessary for my future career. I would also like to thank my dissertation committee members, Professors Ralph Chamberlin, Peter Crozier, and Jeff Drucker, for their generous time and helpful suggestions.

I would like to acknowledge the faculty and staff members as well as the use of facilities in the John M. Cowley Center for High Resolution Electron Microscopy (CHREM) and the Center for Solid State Electronics Research (CSSER) at Arizona State University. Special thanks are due to Karl Weiss and Grant Baumgardner in CHREM, and to Dr. Stefan Myhajlenko and Arthur Handugan in CSSER, for their technical support and assistance throughout my research. The financial support from US Department of Energy (Grant No. DE-FG02-04ER46168) is gratefully acknowledged.

I appreciate our collaborators Prof. J. Cumings (University of Maryland) and Dr. J. Shaw (NIST) who provided samples, expertise, and personal concerns during my PhD research. I also thank my colleagues at ASU, especially Dr. Hua Wang for training me on cleanroom facilities, and Samuel Tobler for coating TEM samples.

Particular thanks and best wishes go to all the group members — Dr. Lin Zhou, Dr. Nipun Agarwal, Dr. Changzhen Wang, Dr. Titus Leo, Dr. M.G. Han, Dr. Suk Chung, Dr. David Cullen, Luying Li, Lu Ouyang, Wenfeng Zhao, Michael Johnson, Allison Boley, Sahar Hihath, Jae Jin Kim, Aram Rezikya, Dinghao Tang, Dexin Kong, and *et al.* for their friendship and kindness. My experiences with the “M&D Gang” have brought

me a lot of joyful memories.

I appreciate the China Scholarship Council and the Ministry of Education for awarding me the prestigious “Chinese Government Award for Outstanding Self-Financed Students Abroad” towards my achievements during the Ph.D. studies. This recognition from my mother country is the highest honor to inspire me heading forward.

Last but not least, I express the most heartfelt gratitude to my family, for their infinite love and support that I could never pay back.

TABLE OF CONTENTS

	Page
LIST OF TABLES	ix
LIST OF FIGURES	x
CHAPTER	
1. INTRODUCTION	1
1.1. Background	1
1.1.1. Fundamentals of magnetism.....	1
1.1.2. Development of magnetic storage.....	4
1.2. Nanopatterned Magnetic Recording Media	6
1.2.1. Fabrication.....	7
1.2.2. Characterization	12
1.2.3. Magnetic properties.....	15
1.2.4. Advances and challenges	22
1.3. Magnetic Domain Wall and Related Devices	23
1.3.1. Racetrack memory.....	23
1.3.2. Domain-wall logic.....	25
1.3.3. Research progress and challenges	27
1.4. Outline of Dissertation	28
References.....	30
2. EXPERIMENTAL DETAILS	35
2.1. Instrumentation	35
2.1.1. Electron beam lithography	35
2.1.2. Transmission electron microscopy.....	37
2.2. Fabrication	38

CHAPTER	Page
2.3. Micromagnetic Simulations	42
2.4. Characterization	44
2.4.1. Lorentz microscopy	44
2.4.2. Off-axis electron holography	46
2.5. Examples of Quantitative Phase Imaging	55
2.5.1. Kagome lattices	55
2.5.2. Ferromagnetic triangles	61
References	64
3. MAGNETIZATION CONFIGURATIONS AND VORTEX-CONTROLLED SWITCHING BEHAVIOR OF Co NANORINGS	66
3.1. Introduction	66
3.2. Remanent States and Switching Behavior of Co Nanorings	69
3.3. Remanent States and Switching Behavior of Slotted Co Nanorings	72
3.4. Comparison Between Experimental Results and Simulations	78
3.5. Discussion	83
3.5.1. Effects of vortex chirality on switching mechanisms	83
3.5.2. Effects of shape anisotropy on switching fields	84
3.6. Conclusions	86
References	87
4. MAGNETIZATION CONFIGURATIONS AND SWITCHING BEHAVIOR OF Co/Cu/Py SPIN-VALVE SLOTTED NANORINGS	89
4.1. Introduction	89
4.2. Magnetization Configurations and Interlayer Coupling at Remanent State	91

CHAPTER	Page
4.3. Switching Behavior of Slotted Nanorings.....	95
4.3.1. Applied field perpendicular to slot direction.....	95
4.3.2. Applied field parallel to slot direction.....	98
4.4. Conclusions.....	102
References.....	103
5. MAGNETIC DOMAIN-WALL MOTION IN NOTCHED PERMALLOY NANOWIRES	104
5.1. Introduction.....	104
5.2. Remanent States.....	106
5.3. Asymmetrical Domain-Wall Pinning Behavior.....	108
5.4. Domain Wall Relaxation and Annihilation.....	113
5.5. Discussion.....	118
5.6. Conclusions.....	120
References.....	122
6. SUMMARY AND FUTURE WORK	124
6.1. Summary	124
6.2. Future Work.....	126
6.2.1. Electron holography of nanomagnet arrays.....	126
6.2.2. Current-induced DW motion.....	127
APPENDIX RELEVANT PUBLICATIONS	129

LIST OF TABLES

Table	Page
2.1. Essential parameters used for practical micromagnetic simulations.	43
3.1. Switching fields measured from experimental and simulated hysteresis loops.	78

LIST OF FIGURES

Figure	Page
1.1. Typical hysteresis loop of a ferromagnetic material.....	2
1.2. Schematic of DW structures and domain configurations. (a) Bloch wall; (b) Néel wall; (c) – (f) domain configurations, where closure domain (f) has lowest energy.....	4
1.3. Road map of magnetic recording technology [10].	5
1.4. Schematic of: (a) conventional longitudinal thin film media; (b) patterned media with in-plane magnetization; and (c) patterned media with perpendicular magnetization [11]......	6
1.5. Schematic of procedures for fabricating patterned media: (a) patterning followed by electrodeposition; (b) patterning followed by evaporation; (c) deposition followed by patterning through etch mask. The trilayer.....	8
1.6. Typical images of nanopatterned element arrays using EBL technique.....	9
1.7. TEM cross-sectional view of Co nanowires and nanoparticles array, as well as corresponding length distribution and microstructures [56].....	10
1.8. TEM images showing monodispersed FePt nanoparticle arrays [57].	11
1.9 Schematic diagram of MOKE magnetometer apparatus [62]......	13
1.10. Schematic diagram showing principle of MFM.	14
1.11. Schematic diagram showing the principle of SEMPA [68]......	15
1.12. Experimentally determined phase diagram showing different magnetic reversal mechanisms in terms of (○) vortex, or (●) single domain behavior [73].	17
1.13. Electron holographic phase images of magnetic elements with shape of triangle, square, pentagon, and hexagon, indicating twisted magnetization	

Figure	Page
patterns at remanent state [49].....	18
1.14. Electron holographic phase images of magnetic elements with different magnetization patterns at remanent state: (a) disk with “S”-state; (b) disk with FC state; (c) ring with “Onion” state; (d) slotted-ring with FC	19
1.15. MFM images of elliptical Permalloy elements with aspect ratios varying from 2 to 10 at the remanent state: (a) 23 nm in thickness after saturation to the right, and (b) 42 nm in thickness after saturation to the.....	20
1.16. Schematic showing the effect of dipole interaction between two magnetic particles [61].	21
1.17. Schematic showing principle of racetrack memory using pulse-triggered DW motion along magnetic NWs [75].....	24
1.18. Summary of conventional CMOS circuit elements and corresponding DW logic elements to realize different logic functionalities [79].....	26
1.19. Examples of typical studies on racetrack memory and DW logic [76, 79]	27
2.1. Electron optics system of JBX-6000FS/E [1].....	36
2.2. Schematic for a TEM and its electron optics scheme.....	37
2.3. Schematics showing the geometry and dimensions of the membrane samples: (a) top view; (b) side view. (c) Actual image.	39
2.4. Schematic outline of EBL process: (a) cleaning membrane; (b) spinning and baking PMMA; (c) EBL exposure; (d) resist development; (e) deposition of magnetic material; (f) lift off.....	40
2.5. Schematic of (a) Lorentz force, and (b) Fresnel Lorentz imaging. Electrons passing through the magnetic sample are deflected due to the in-plane magnetic field, and form DW magnetic contrast at under- or	45

Figure	Page
2.6. Schematic illustrating the typical configuration used for off-axis electron holography in the TEM (Philips CM200-FEG) [14].	46
2.7. Schematic illustration contrasting the origin of phase shifts for holography of electrostatic and magnetic fields [14].....	48
2.8. Image reconstruction process for extracting phase shifts from hologram	51
2.9. Different representation schemes for phase shifts related to magnetic field. (a) Pseudo-color phase image; (b) 8× amplified phase contours; (c) x- and (d) y-gradient of phase in (a); (e) magnetic induction map.....	51
2.10. (a) Schematic diagram showing the use of specimen tilt to provide the in-plane component of the applied field needed for in situ magnetization reversal experiments. (b) Hall probe measurements of.....	54
2.11. (a) In-focus, and (b) defocused, Lorentz TEM image of kagome structure. Fresnel contrast indicates clockwise and counterclockwise closed loops. [27].....	55
2.12. Phase images of kagome lattice composed of Py and corresponding line profiles in remanent state with: (a) saturation field pointing to bottom-left; (b) saturation field pointing to top-right; and (c) pure.....	57
2.13. Phase contour map (12× amplified), magnetic induction map, and magnetic contour map of (a)–(c) 500-nm-diagonal kagome lattice, and (d)–(f) enlarged box area, respectively. Magnetization directions	59
2.14. (a) Lorentz TEM image of as-fabricated Y-junctions. (b) Hologram of an individual Y-junction in boxed area of (a). (c) Phase contour map (12× amplified), (d) magnetic induction map, and (e) magnetic contour.....	60
2.15. Micromagnetic simulations showing remanent configuration: (a) Y state	

Figure	Page
in a sharp triangle; and (b), (c) buckle states in rounded triangles [29].....	61
2.16. Lorentz images of Py triangles with different sizes, and corresponding phase contours (4× amplified) as function of in-plane applied field. Applied field along the long axis of the triangles.....	63
3.1. Schematics showing the geometry of Co nanoring and slotted Co nanoring, grown on thin silicon nitride TEM membranes: (a) Side view; and plan view of (b) nanoring; and (c) slotted nanoring.....	68
3.2. (a) Lorentz TEM image showing Co nanoring array (Scale bar indicates 500 nm). (b) Reconstructed holographic phase image of an individual nanoring showing FC state at remanence, with phase.....	69
3.3. Hysteresis loop of an individual Co nanoring where a–d correspond to specific states visible in phase images: (a) onion state at saturation; (b) excitation of double-vortex; (c) FC state; (d) onion state at reverse.....	71
3.4. Lorentz images of Co slotted nanorings, with slot directions (a) parallel, and (b) perpendicular, to applied field directions (indicated by double arrow). Reconstructed phase images showing individual Co.....	73
3.5. (a) Three-step, and (b) one-step, hysteresis loops for Co elements with applied field parallel, and perpendicular, to the slot direction, respectively. The inset schematics indicate the different magnetization.....	75
3.6. Phase images of Co nanoring (SR1) illustrating the magnetization configurations for corresponding states in the hysteresis loop in 3.5 (a): (a) onion state; (b) excitation of vortex at remanence; (c) FC state; and.....	76
3.7. Phase images of Co nanoring (SR2) illustrating the magnetization configurations for corresponding states in the hysteresis loop shown in	

Figure	Page
Figure 3.5 (b): (a) Ω state; (b) FC state of CW; (c) FC state of CCW;	76
3.8. (a)–(c) Experimental, and (d)–(f) simulated, hysteresis loops for Co nanoring, slotted nanoring with applied field parallel to slot (SR1), and slotted nanoring with applied field perpendicular to slot (SR2).....	79
3.9. Magnetic induction maps for (1) Co ring, (2) SR1, and (3) SR2, comparing the experimental results (upper row) and simulations (lower row). Letter labels refer to corresponding states in Figure 3.8. Applied	81
3.10. Schematics showing vortex controlled switching mechanism for nanorings: (a) vortex motion rule; (b) onion-FC-onion transition; and (c) coherent onion rotation.	84
3.11. Demagnetization energy as a function of applied field for Co nanoring and SR1 shape, as calculated from OOMMF simulations. The calculation is obtained from the forward hysteresis half-cycle.	85
4.1. Schematics illustrating (a) the structure of trilayer stack, and (b) the shape of slotted ring, for Co/Cu/Py SV elements.	91
4.2. (a) In-focus image showing as-prepared array of Co/Cu/Py SV elements (OD/ID= 400/200nm, $\alpha = 60^\circ$); (b) defocused Fresnel image of single Co/Cu/Py SV element in remanent state.....	92
4.3. Reconstructed holographic phase images of Co/Cu/Py SV elements showing different remanent configurations: (a) onion state; (b) FC state. Initial saturation direction from bottom-left to top-right. Color bar.....	93
4.4. Phase images of (a) parallel- and (b) antiparallel-coupled configurations of slotted SV element at remanent state. (c) Corresponding line profiles after removal of MIP contributions.	94

Figure	Page
4.5	Hysteresis loops for Co/Cu/Py SV element through major and minor cycles. Applied field perpendicular to the slot direction. Insert schematics indicate different magnetic coupling between Co and Py 96
4.6.	Phase contour (4× amplified) images showing representative magnetization states corresponding to labels a–c in Figure 4.7: (a) parallel coupled Ω -state; (b) parallel coupled FC; (c) antiparallel 97
4.7.	Three-step hysteresis loops for Co/Cu/Py SV nanoring with applied magnetic field parallel to the slot direction. Insert schematics indicate different magnetic coupling between Co and Py layers with onion 98
4.8.	Phase contour (4× amplified) images of SV element illustrating the magnetization configurations of corresponding states in the hysteresis loop of Figure 4.7. Applied fields are parallel to the slot direction, 100
4.9.	(a) Schematic hysteresis loop after Figure 4.7. Magnetic components separated to represent the individual behavior of (b) Co, and (c) Py layers..... 101
5.1.	Schematic drawings showing the design of Py NWs: (a) plan-view showing shape and dimensions; (b) 3D view showing Py NW on the amorphous nitride membrane. 106
5.2.	(a) Lorentz image of Py nanowire as fabricated, with inset showing enlarged view of trapezoid notch. (b) Phase shift; (c) reconstructed magnetic induction map; and (d) calculated magnetic induction map; of 107
5.3.	Montage showing representative states during DW motion indicated in Fresnel images (top) and corresponding magnetic induction maps (bottom), as extracted from pairs of holograms. (I) DW nucleation, (II) 110

Figure	Page
5.4. (a) Schematics of representative configurations, corresponding to states I – VII in Figure 5.3, respectively. (b) Simulated hysteresis loop showing extra plateau labeled III due to asymmetrical DW pinning	112
5.5. Defocused Fresnel images showing (a) TDW pinning at the notch with applied field (H) of ~72 Oe, and (b) relaxation of VDW at remanent state.....	113
5.6. (a) Experimental, and (b) simulated, magnetic induction maps for DW pinning state. (c) Experimental, and (d) simulated, magnetic induction maps of VDW obtained after NW relaxation in zero field.....	114
5.7. (a) Defocused Fresnel images showing representative states during DW annihilation: (I) DW pinning at the notch; (II) DW depinning from the notch; (III) two DWs attracting each other; (IV) DW annihilation..	116
5.8. (a) Schematics of representative configurations, corresponding to states I – IV in Figure 5.7, respectively. (b) Distribution of critical fields needed to emerge specific well-defined states (I, II, and IV) during DW.....	117
5.9. Schematic diagram illustrating the entire process and representative stages during DW propagation, also indicating correlation between chiralities of the nucleation pad, DWs, and notch.....	119
6.1. SEM images showing (a) overview, and (b) enlarged view, of Py NW with integrated testing electrodes. (c) TEM images showing a notched Py NW attached to two electrodes.....	128
6.2. Schematics showing: (a) Py NWs with electrodes integrated on a silicon nitride membrane window; (b) in situ biasing TEM specimen holder having a special 2-point contact cartridge to load the membrane	128

CHAPTER 1

INTRODUCTION

1.1. Background

1.1.1. Fundamentals of magnetism

Magnetism has been a subject of much interest for thousands of years. As early as 600 BC, magnets were discovered by Greek philosophers, and they were used as compasses by the Chinese in 400 BC. However, it was not until the 1800s that magnetism was considered as a scientific discipline, when the relationship between electricity and magnetism was proposed by Oersted [1]. Nowadays, the principles of magnetism are well established, and the fundamental concepts [2-4] can be summarized, as found below.

Materials behave differently when they are exposed to an external magnetic field. In the classical point of view, the basic parameters are magnetic field strength (H), magnetization (M), and magnetic induction (or magnetic flux density, B), where magnetization is a measure of material response to applied field, and magnetic induction is net magnetic flux density inside the material. The relationships between these parameters are described by the following equations:

$$M = \chi H \quad (1.1)$$

$$B = \mu_0(M + H) \text{ (SI units); or } B = M + 4\pi H \text{ (cgs units)} \quad (1.2)$$

According to their different response (so-called susceptibility χ) to an applied magnetic field, materials are classified as diamagnetic, paramagnetic, ferromagnetic, antiferromagnetic, and ferrimagnetic.

Our particular interest here is in ferromagnetic materials, such as iron, cobalt, nickel, and their alloys. The magnetic moments in ferromagnetic materials are

spontaneously aligned in a regular manner, resulting in strong net magnetization even without any applied field. Ferromagnetic materials have the property of hysteresis, which can be technically characterized by a hysteresis loop, plotting out magnetization M (or magnetic induction B) versus applied field H . Figure 1.1 shows a typical hysteresis loop of a ferromagnetic material. The ferromagnet is initially not magnetized, and application of the field H causes magnetic induction to increase in the field direction. If H is increased indefinitely the magnetization eventually reaches saturation at a value which is designated as M_s . When the external field is reduced to zero, the remaining magnetic induction is called the remanent magnetization M_r . The magnetic induction can be reduced to zero by applying a reverse magnetic field of strength H_c , which is known as the coercivity.

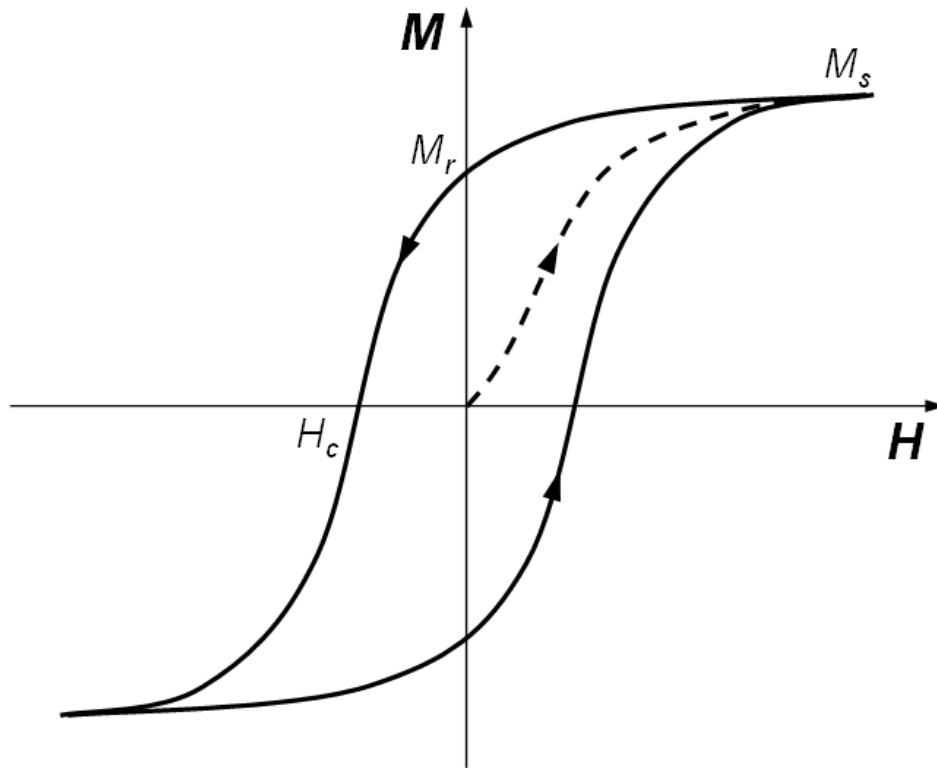


Figure 1.1. Typical hysteresis loop of a ferromagnetic material.

The shape of a hysteresis loop reflects the properties of the ferromagnet. The area inside the hysteresis is proportional to the energy needed to rotate the magnetic moments. Based on the strength of the coercive field, ferromagnets can be roughly defined as hard or soft magnetic materials. Hard (or permanent) magnets have coercivity as high as 2×10^6 A/m (or 25000 Oe), and are widely used in electric motors, generators, loudspeakers, frictionless bearings, magnetic levitation systems, and various forms of holding magnets such as door catches. Soft magnets have much lower coercivity such as 1.0 A/m (or 12 mOe), and are mainly used in transformers, inductors, and magnetic sensors. Between these two extremes are magnetic recording media, which require medium coercivity (typically ranging from 10^4 A/m to 10^5 A/m), high M_r/M_s ratio, and good squareness of hysteresis loop so as to ensure a sharp binary transition with low noise.

Two additional important concepts important for understanding the behavior of magnetic materials are magnetic domains and domain walls (DWs). A magnetic domain describes a region within a material which has uniform magnetization. The regions separating magnetic domains are called DWs where the direction of the magnetization rotates, usually coherently, from one domain to the adjacent domain [5]. The existence of domains is a consequence of energy minimization [6]. Figure 1.2 shows schematics that illustrate DW structures and domain configurations. To reduce the magnetostatic (MS) energy, the spins inside the Bloch wall rotate through the plane of the wall, unlike the Néel wall where the spins rotate in the plane of the wall. As shown in Figure 1.2 (c) – (f), the introduction of 180° DWs reduces the MS energy but raises the DW energy, whereas 90° closure DWs can eliminate MS energy but increase the DW energy. Closure domain formation is favored for large magnetization, small anisotropy, and small wall energy.

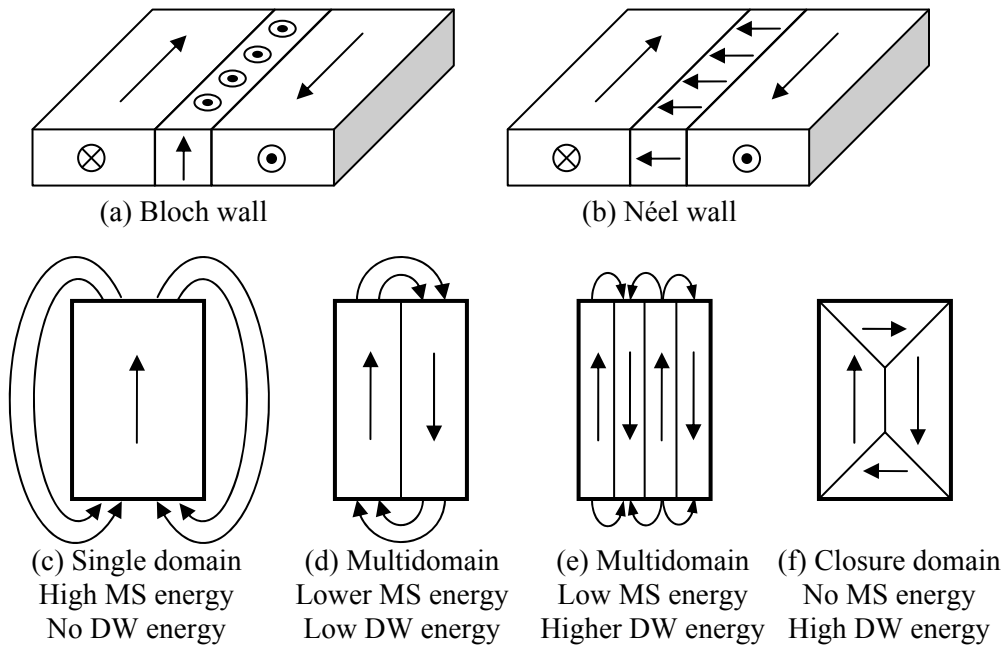


Figure 1.2. Schematic of DW structures and domain configurations. (a) Bloch wall; (b) Néel wall; (c) – (f) domain configurations, where closure domain (f) has lowest energy.

1.1.2. Development of magnetic storage

Magnetic storage was first suggested by Oberlin Smith in 1888 [7]. However, the first working magnetic recorder was invented in 1898 by Valdemar Poulsen, who recorded a signal on a wire wrapped around a drum [8]. It was another three decades before Fritz Pfleumer in 1928 developed the first magnetic tape recorder [9]. Early magnetic storage devices were designed to record analog audio signals. Modern digital recording for computer information storage was developed by IBM and the first magnetic hard disk drive (HDD), which became available in 1957, had a data storage density of only 2000 bit/in² [10]. Since then, the data storage density has increased by many orders of magnitude. Today, the present storage density is approaching 500 Gbit/in². The rate of increase in storage density has accelerated dramatically in recent years due to a new

generation of thin film recording media, and advanced read/write heads with improved signal-to-noise ratio (SNR), as illustrated in the HDD road map shown in Figure 1.3.

Since data is being stored magnetically, the intrinsic property of superparamagnetism will become a major limitation for conventional longitudinal recording media as grain sizes get smaller and smaller. Thus, the energy required to change the direction of the magnetic moment of a particle becomes comparable to the ambient thermal fluctuations, which means that randomization of the domain orientations becomes significant and data would be lost.

In recent years, new techniques such as bit-patterned recording, perpendicular recording, thermal-assisted magnetic recording, and racetrack memory, have been proposed for achieving higher storage density [11–13]. Two of these promising candidates, namely, patterned recording media and racetrack memory, are described in the following sections.

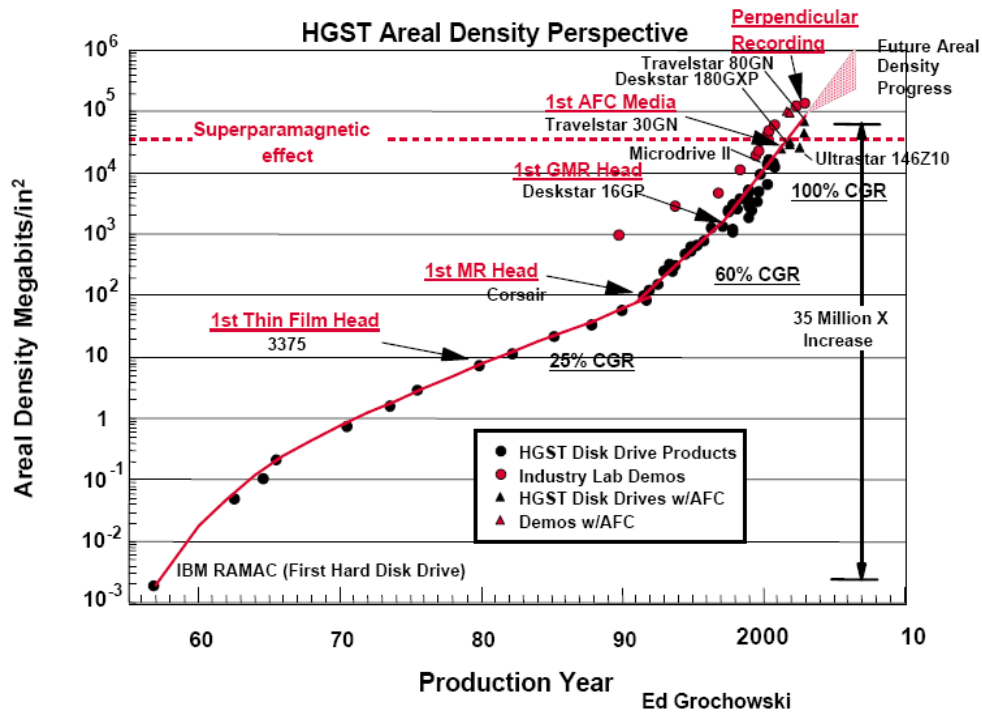


Figure 1.3. Road map of magnetic recording technology [10].

1.2. Nanopatterned Magnetic Recording Media

Figure 1.4 shows schematics of conventional longitudinal thin-film media, patterned media and perpendicular media. In longitudinal thin-film media, each bit cell may contain tens or hundreds of grains, which are separated by the transitions between oppositely magnetized regions. In patterned media, single domain bits, which can be either polycrystalline or single crystal, are defined with period p . The media consists of arrays of such elements, each of which has uniaxial magnetization lying either in-plane of the film or perpendicular to the film. Depending on different magnetization states, each element represents one binary bit (up – “1”; down – “0”).

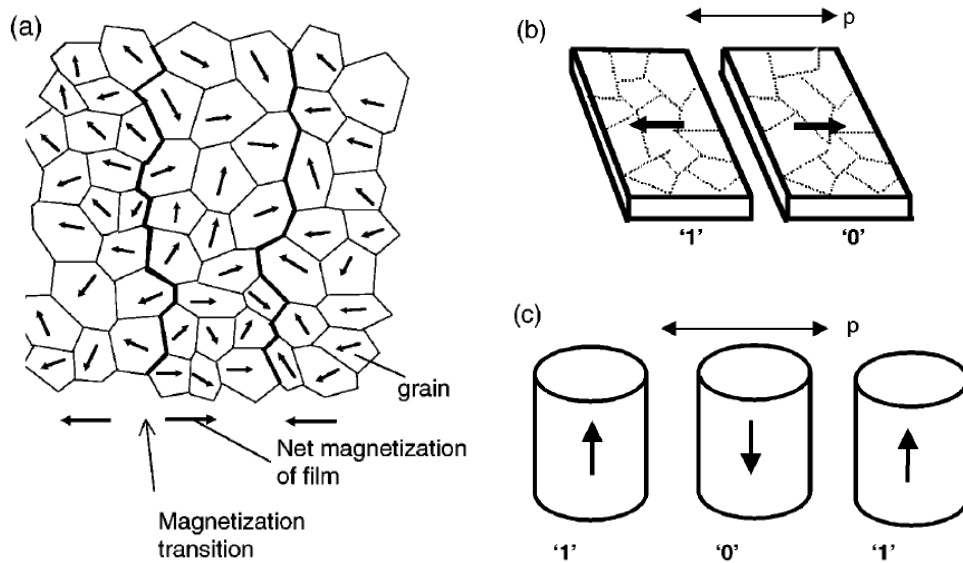


Figure 1.4. Schematic of: (a) conventional longitudinal thin film media; (b) patterned media with in-plane magnetization; and (c) patterned media with perpendicular magnetization [11].

Patterned media can approach higher recording density because of two major advantages. One reason is that transition noise is eliminated due to the physically well-defined bit elements. The other is that the usual stability criterion refers to the volume and anisotropy of the entire element, rather than the individual grains of which it is composed. However, many technical issues still need investigation. Recent progress and challenges are briefly reviewed in the following sections.

1.2.1. Fabrication

Fabrication has become one of the most demanding processes for increased storage density. In order to achieve recording density of 1 Tbit/in², the lateral dimension for one bit is about 25 nm. Taking the interaction between adjacent bits into account, which should obviously be eliminated as much as possible, the effective lateral dimension for a single element is only around 12 nm. Fabrication of large-area arrays of elements with dimensions on the sub-100-nm scale requires advanced lithography or accurate self-assembly techniques. Several commonly used techniques including nanolithography, template-assisted growth, and self assembly, are summarized.

- Nanolithography

For features on and below the sub-micron scale, several lithography techniques, including electron-beam, X-ray, ion-beam, nanoimprint, and interference lithographies can be utilized [14]. Among these techniques, electron-beam lithography (EBL) still represents the most flexible and effective way to pattern materials at the nanoscale for scientific research purposes. However, its relative high cost and through-put are still major limitations for commercial use. The EBL technique has often been used to produce prototype structures, followed by magnetic materials deposition and pattern transfer processes. Patterns can be transferred into the magnetic materials by additive or

subtractive processes. In an additive process, material is deposited by electrodeposition or evaporation after EBL patterning, as illustrated in Figures 1.5 (a) and (b). In a subtractive process, material is deposited first, followed by etching through a lithographically generated mask, as shown in Figure 1.5 (c). Additive process followed by liftoff has been widely used to fabricate element arrays, where electrodeposition is commonly used for elements with high aspect ratio, while evaporation is used for flat elements or conical particles. The subtractive process provides the most flexible choices of materials and microstructures, such as complex alloys, and epitaxial or multilayered thin films.

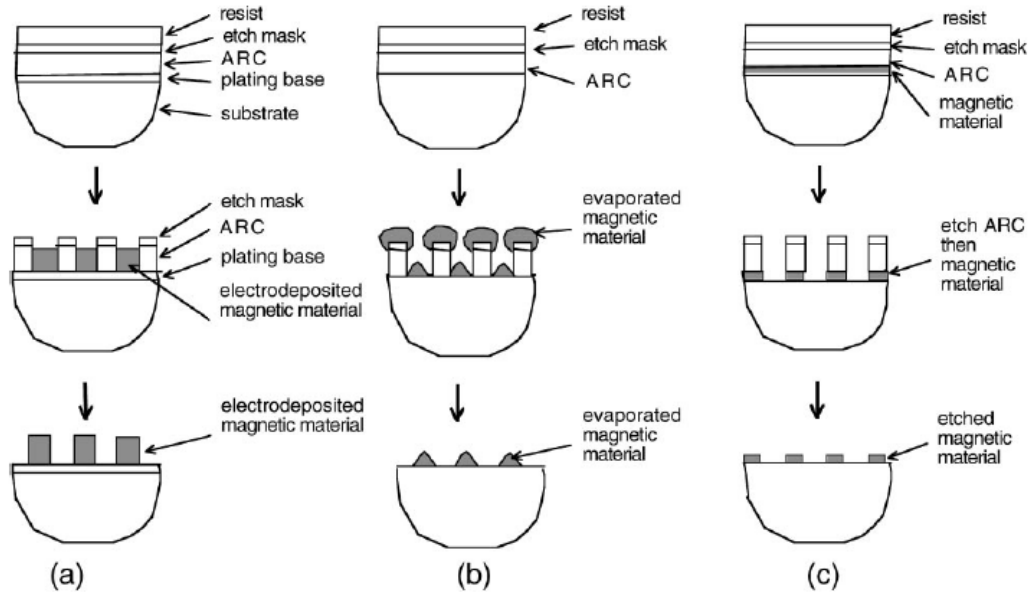


Figure 1.5. Schematic of procedures for fabricating patterned media: (a) patterning followed by electrodeposition; (b) patterning followed by evaporation; (c) deposition followed by patterning through etch mask. The trilayer resist stack shown above consists of resist, etch mask, and antireflective coating (ARC) [11].

Ferromagnetic element arrays with different shapes, such as triangles, squares, rectangles, diamonds, pentagons, hexagons, disks, rings, ellipses, elliptical-rings, pac-mans, slotted-rings, etc., have been fabricated using the EBL technique, followed by evaporation or sputtering [15–53]. Typical images of such element arrays are shown in Figure 1.6 [15, 36, 52].

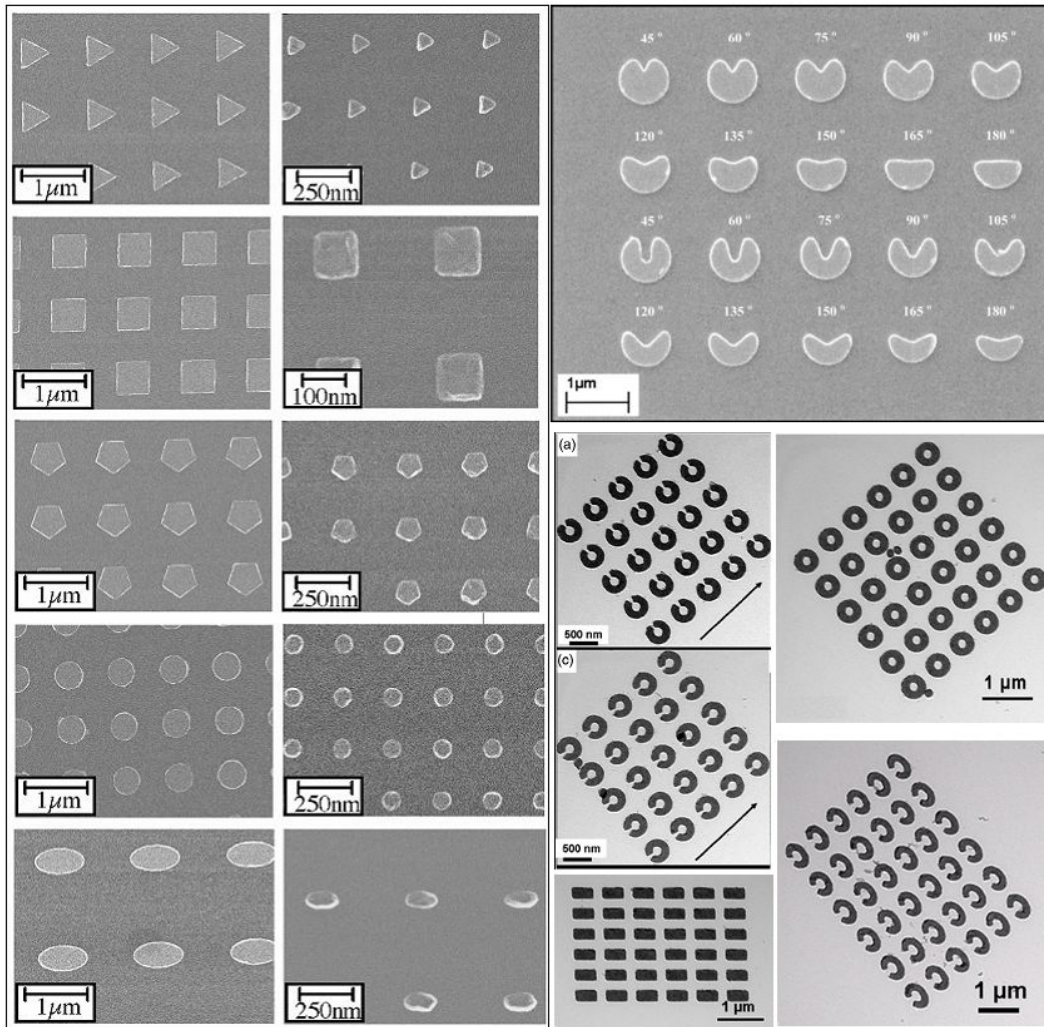


Figure 1.6. Typical images of nanopatterned element arrays using EBL technique [15, 36, 52].

- Template-assisted growth

Self-organized templates have been utilized to make arrays of magnetic nanostructures. The templates may have ordered porous structures with dimensions even smaller than achievable through nanolithography. The templates can be used as a mask for etching magnetic material, or as a mold for deposition of magnetic material, similar to lithography. The most common process is the use of anodized aluminum oxide templates followed by electrodeposition. This method is suitable for fabrication of arrays of long nanowires, but it is difficult to control the length distribution of short pillars [54–56]. Figure 1.7 shows Co nanowire and nanoparticle arrays fabricated using alumina templates [56]. A major disadvantage of this approach is that the template-assisted array structures have poor long-range order, which is an aspect that still needs exploration.

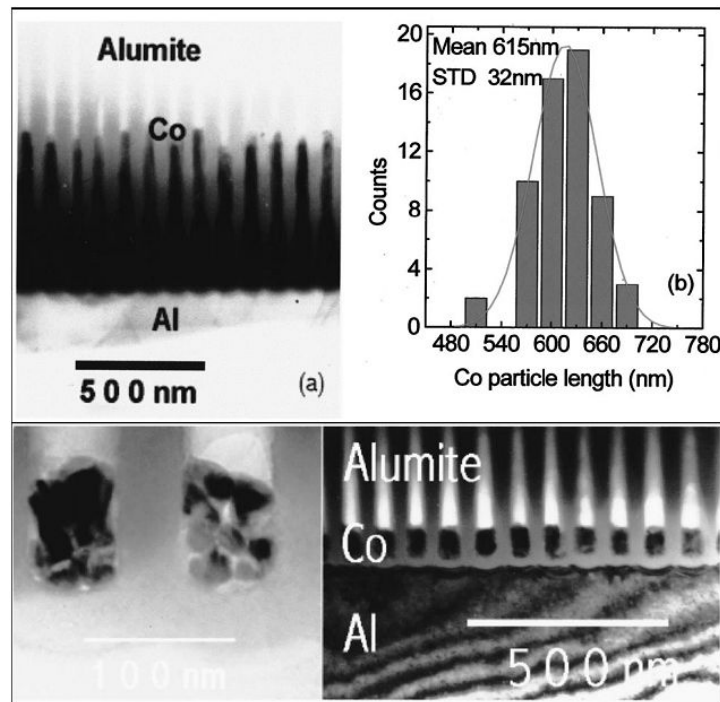


Figure 1.7. TEM cross-sectional view of Co nanowires and nanoparticles array, as well as corresponding length distribution and microstructures [56].

- Self assembly

Self assembly is a process whereby a system can organize itself to form a well-ordered structure or pattern. Nanoparticles can be self-assembled onto a substrate to form a regular array with very fine-scale structures over a large-scale area. This rapid, fine-featured, large-scaled synthesis has great potential for applications if the following drawbacks can be solved. The most critical problem is the need to control the particle size distribution to obtain uniform magnetic properties. Moreover, oxidation and agglomeration may affect the structure and separation of array elements, especially for magnetic nanoparticles. Monodispersed magnetic nanoparticle (FePt, Co, etc.) arrays with narrow size distribution and readily controlled composition [57–60], as shown in Figure 1.8, have been synthesized through a solution phase route. It was also suggested that self-assembly combined with templates could be used to improve the long-range order.

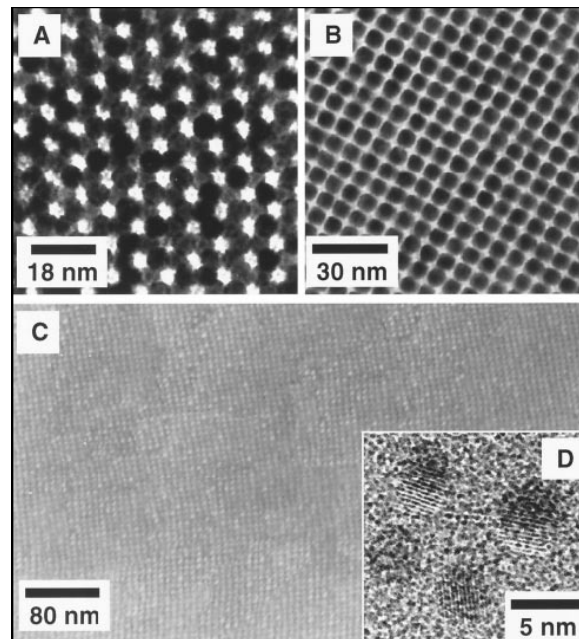


Figure 1.8. TEM images showing monodispersed FePt nanoparticle arrays [57].

1.2.2. Characterization

For magnetic recording media, scanning electron microscopy (SEM) and atomic force microscopy (AFM) can be used for characterization of morphology and surface topography, while transmission electron microscopy (TEM) is suitable for microstructure observation and analytical spectroscopy. In practice, due to the difficulty of detecting the small signal from a single nanoparticle, magnetic properties are usually measured by averaging over large arrays of identical nanoelements, using, for example, vibrating sample magnetometry (VSM), superconducting quantum interference device (SQUID), etc. [61]. In addition, several microscopic techniques can also be used to characterize magnetic structures and switching behavior for either individual nanoelements or large-scale arrays. Several of these commonly used techniques are described below.

The Magneto-Optic Kerr Effect (MOKE) involves measurement of the reflected light from a magnetized surface which is changed in both polarization and reflectivity. Since the change in polarization or reflectivity is directly proportional to the magnetization close to the surface, MOKE has been used to measure magnetic hysteretic response, especially in thin films [62–64]. Depending on the different geometries of the magnetization vector with respect to the reflecting surface and the plane of incidence, the technique can be categorized in three forms which are referred to as polar, longitudinal, and transverse MOKE. Unlike other quantitative techniques, i.e. SQUID and VSM, MOKE cannot yield an absolute value for magnetization; typical hysteresis loops are averaged and normalized to unity at saturation. Moreover, MOKE cannot measure the properties of an individual nanoscale element due to the detection limit. A typical MOKE magnetometer is schematically shown in Figure 1.9 [62].

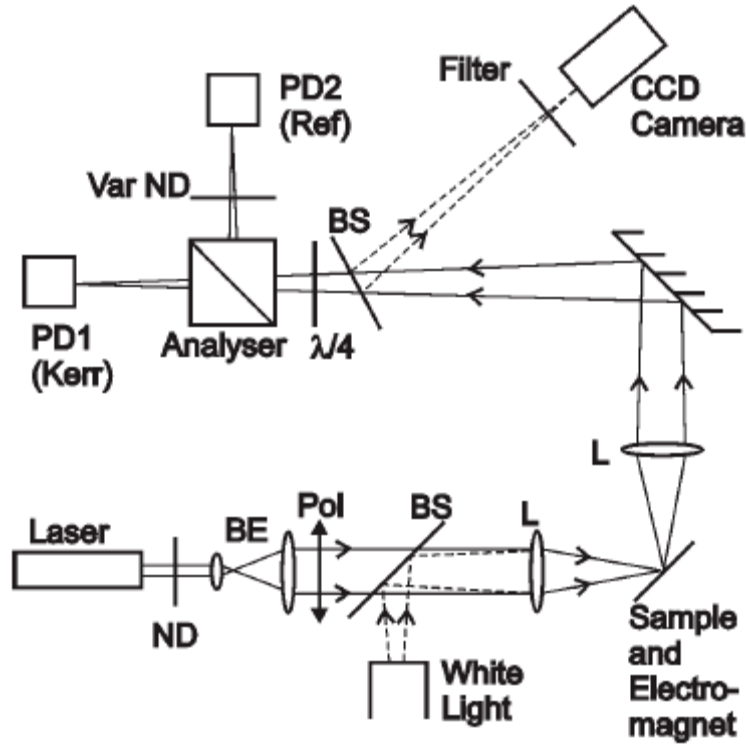


Figure 1.9 Schematic diagram of MOKE magnetometer apparatus [62].

Magnetic force microscopy (MFM) is a special type of AFM. The principle of MFM is based on AFM, but the probe consists of magnetic material so that magnetic interactions between probe and specimen can be detected [65, 66]. The MFM can thus image the stray magnetic field above the surface of a sample, as depicted in Figure 1.10. A magnetic tip is brought into close proximity with the surface and scanned over the surface to reveal the magnetic domain structure of the sample at up to 50 nm resolution. Since it is possible to apply external magnetic fields during measurement, the field dependence of domain structures and magnetic reversal processes can be observed. The advantages of MFM include that minimal sample preparation is required, and smaller single elements can be examined. However, MFM imaging contains information about both the topography and the magnetic properties of a surface, and the complicated

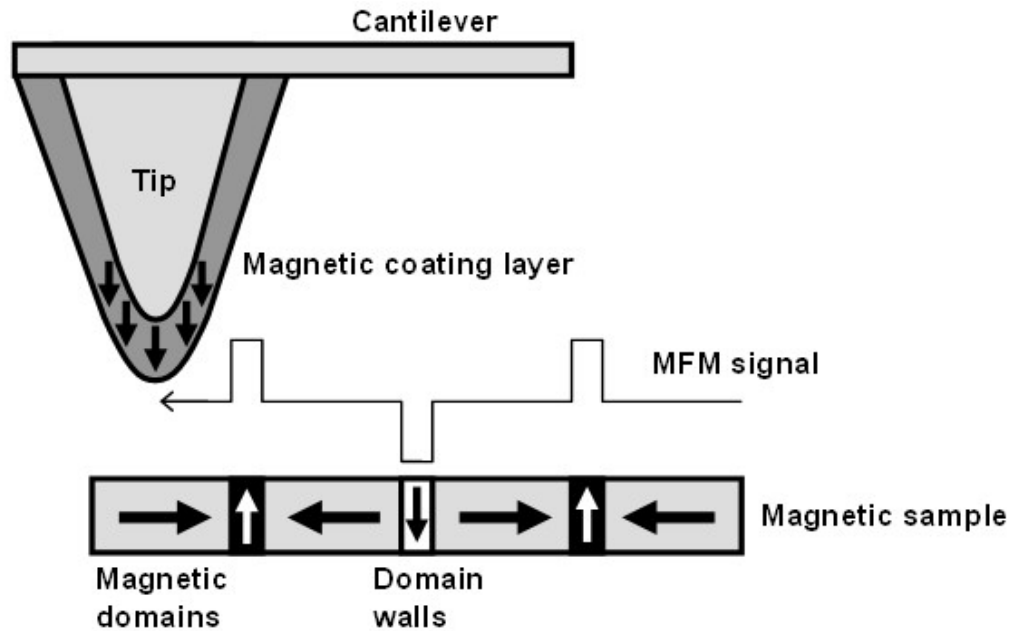


Figure 1.10. Schematic diagram showing principle of MFM.

interaction between the magnetic tip and the specimen surface makes quantitative interpretation very difficult [67].

Scanning Electron Microscopy with Polarization Analysis (SEMPA) is a special SEM technique developed for characterizing very small magnetic structures. SEMPA images magnetization by measuring the spin polarization of secondary electrons emitted in a SEM. Since secondary electron spin polarization is directly related to the magnetization of the sample, SEMPA produces a direct image showing the magnitude and direction of the magnetization in the region probed by the incident electron beam, as sketched in Figure 1.11 [68]. SEMPA takes advantage of the SEM characteristics of high spatial resolution (~ 10 nm), long working distance, and large depth of field, and also allows magnetization measurements independent of the topographic structures. However, the surface sensitivity (~ 1 nm depth) clearly limits its application for bulk materials.

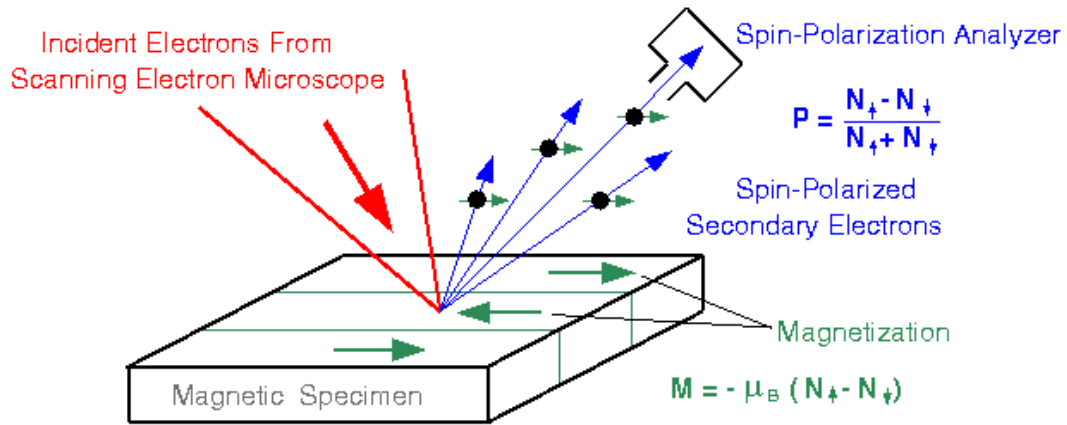


Figure 1.11. Schematic diagram showing the principle of SEMPA [68].

Photoemission electron microscopy (PEEM) is an imaging technique that uses the secondary electrons emitted from a sample surface upon absorption of photons in ionizing radiation [69]. Modern PEEMs can routinely approach 10 nm resolution or better, and are sensitive to specimen surface. Using circularly polarized x-rays to stimulate photoelectrons, magnetic contrast can be added through the X-ray magnetic circular dichroism (XMCD) effect. By combining the element sensitivity of time-resolved XMCD with the spatial resolution of PEEM, XMCD-PEEM is a very powerful technique for investigating magnetization dynamics in thin-film systems, especially vortex propagation and DW motion in nanomagnets [70–72].

TEM-based magnetic imaging techniques, such as Lorentz microscopy and electron holography, are the primary characterization methods in this dissertation research. Details of these techniques are described in a later section (§2.4).

1.2.3. Magnetic properties

For the purpose of data recording applications, the ideal properties for patterned media are well-defined remanent states, reproducible magnetization reversal process, and

narrow switching field distribution. In practice, there are two major factors that affect the magnetic properties of nanomagnets – size and anisotropy.

It is well known that when the physical dimensions of a system become comparable to characteristic length scales of a given physical property, these properties can be severely affected. In the case of magnetism, the main characteristic length scales are the exchange length (l_{ex}), and the magnetic DW thickness (δ), which are on the order of ten to several tens of nanometers for most common magnetic materials. From the energy point of view, the magnetic properties of nanomagnets depend sensitively on the balance of exchange energy, magnetostatic energy, anisotropy energy, and Zeeman energy [11, 61]. Exchange coupling aligns the spins parallel to each other so that the existence of a uniform state of magnetization within the material minimizes the exchange energy. On the other hand, the competing tendency to minimize magnetostatic energy favors closed magnetization states, which can be achieved by the formation of DWs or vortices. The magnetic microstructure and behavior of a magnetic material are highly size-dependent: as the dimensions become on the order of l_{ex} , the magnetization configuration of the material will go from a multidomain state to a closure domain state. Moreover, when the size becomes smaller than l_{ex} , the magnetization evolves from closure domain to single domain; and if the size becomes sufficiently small, the magnetization will finally go from a single domain state to superparamagnetic [61].

Effects of size dependence on remanent configuration and switching behavior as functions of sample diameter and thickness have been determined experimentally, as illustrated in the phase diagram in Figure 1.12 [73]. This study showed a transition from multidomain or vortex states to a single-domain state as the element size was decreased, and similar tendencies were found as the thickness was decreased. Switching fields typically increase as the particles become smaller, and their behavior approximates more

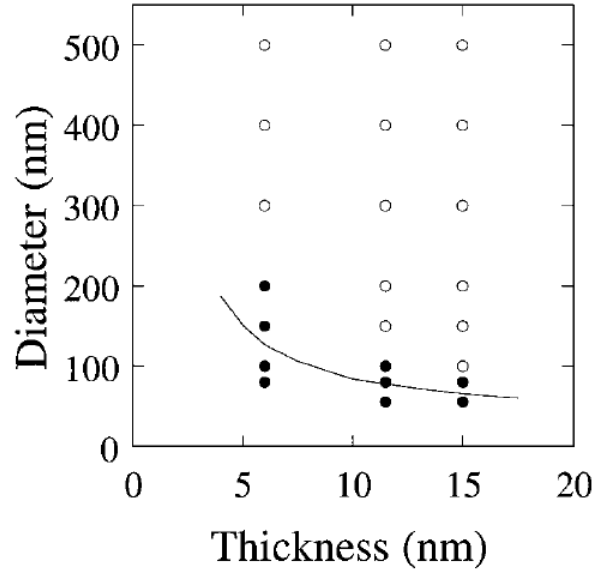


Figure 1.12. Experimentally determined phase diagram showing different magnetic reversal mechanisms in terms of (○) vortex, or (●) single domain behavior [73].

closely to coherent rotation. However, particles with dimensions of 100 nm or above generally show non-uniform reversal [11].

Anisotropy controls magnetic properties in terms of the tendency to align magnetization along the easy axis of magnetic particles. Magnetic anisotropies include magnetocrystalline anisotropy, which represents an intrinsic material property, and shape anisotropy, which can be defined by controlling the shape of individual particles. For patterned magnetic media, especially for polycrystalline systems that minimize the intrinsic anisotropy by averaging over random orientations, shape anisotropy plays a critical role in determining their magnetic behavior. Nanopatterned magnetic elements with different shapes have been studied. The patterns include linear shapes, such as triangles, squares, pentagons, hexagons [15, 32, 49], and circular shapes, such as disks [17, 25], ellipses [30, 34, 35, 53], rings [19–24, 48], elliptical rings [26, 27], and slotted elements [36–42, 47, 50, 52].

For polygonal elements, the magnetization can appear as vortices, or complex twisted patterns, depending on the element size and geometry, initial saturation field, and presence of any defects. Due to the asymmetry between demagnetization and element geometry (shape anisotropy), the magnetization would tend to be parallel to the element edges, and twist inside the element, as indicated in Figure 1.13 [49]. However, since many parameters are involved but few can be easily interpreted, it is very difficult to draw useful conclusions from existing results.

Circular shapes were designed with the intent to obtain simple flux-closure (FC) states with opposite chiralities (Figure 1.14 (b)), which could technically be used as binary storage bits [49]. However, high-energy vortex cores were often introduced during magnetization reversal, and “S”-states were formed by shifting the FC center away from the geometric disk center, as shown in Figure 1.14 (a). To eliminate the presence of such vortex cores, ring-shaped elements were proposed, and so-called “onion” states were observed at remanence, as shown in Figure 1.14 (c). Furthermore, slots were also introduced as a geometric restriction to force the formation of stable flux closures, as indicated in Figure 1.14 (d).

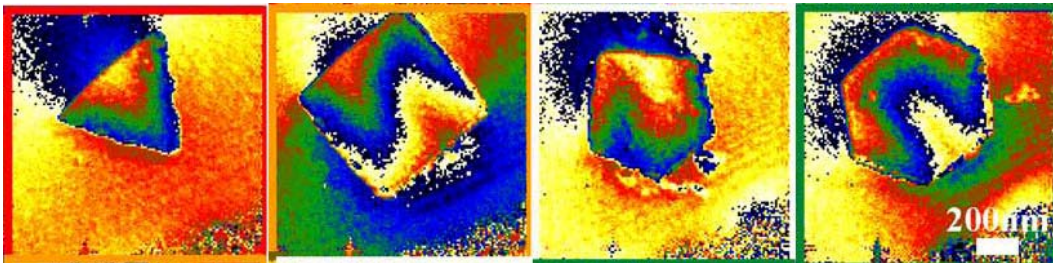


Figure 1.13. Electron holographic phase images of magnetic elements with shape of triangle, square, pentagon, and hexagon, indicating twisted magnetization patterns at remanent state [49].

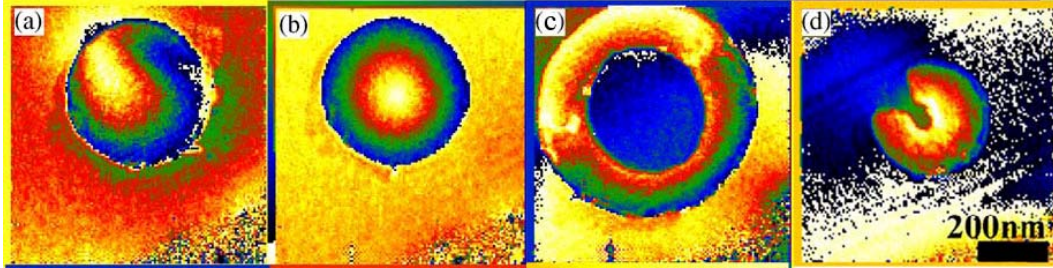


Figure 1.14. Electron holographic phase images of magnetic elements with different magnetization patterns at remanent state: (a) disk with “S”-state; (b) disk with FC state; (c) ring with “Onion” state; (d) slotted-ring with FC state [49].

Elements with different shapes exhibit different magnetization reversal mechanisms. For elements with solid shapes, vortices are generally involved in reversal processes. For polygons with the same area, the field needed for sweeping out the vortex increases as the shape becomes more like a disk [32]. Due to the sensitivity of shape fluctuations and edge roughness, linear shapes usually have more complicated switching processes than circular shapes. For ring-shaped elements, magnetization reverses between flux-closures and onion states by means of the movement of head-to-head DWs [19], and the switching fields are found to be strongly dependent of the ratio of inner and outer diameters [48].

For magnetic particles with a specific geometry, shape anisotropy is directly dependent on the lateral aspect ratio. Figure 1.15 shows MFM images of elliptical elements with different aspect ratios at remanent state [74]. The single-domain configuration was observed in elements with an aspect ratio larger than 5. A typical vortex state was visible in thinner elements (23 nm) with aspect ratios of 2 and 3, but thicker elements (42 nm) showed more diverse domain structure and complex configurations, including two-vortex state, mixed state (vortex and cross-tie walls), and

cross-tie walls, with aspect ratios of 2, 3, and 4, respectively. It was also found that the switching fields of small elements with aspect ratio less than 5 were significantly dependent on the aspect ratio, due to shape anisotropy. However, the switching fields of the ellipses with aspect ratios larger than 5 did not show obvious dependence on the aspect ratio. In other words, the switching fields of uniform magnetization reversal were almost independent of the aspect ratio.

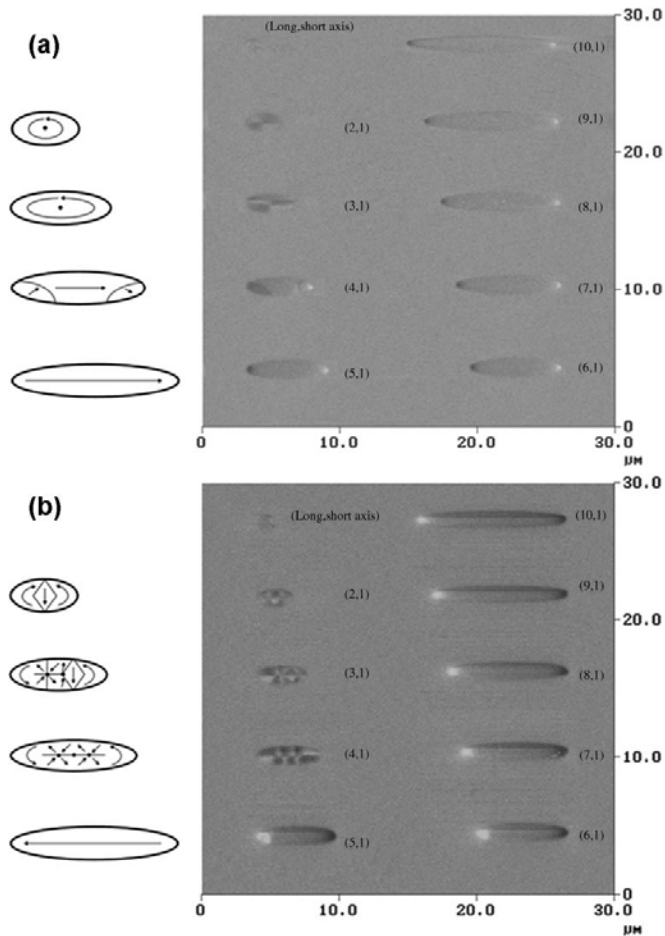


Figure 1.15. MFM images of elliptical Permalloy elements with aspect ratios varying from 2 to 10 at the remanent state: (a) 23 nm in thickness after saturation to the right, and (b) 42 nm in thickness after saturation to the left. The schematic diagrams on the left indicate the magnetization configurations for clarity [74].

When individual elements are patterned in arrays, the interactions between these elements introduce new anisotropies into the system. This anisotropy can be treated, to a first-order approximation, as the effect of dipole interaction (or fringing field) within the entire arrays. Depending on the different arrangements of individual dipolar fields relative to the characteristic anisotropy of the array, the overall switching mechanism can be represented in terms of two different hysteresis loops, as shown in Figure 1.16 [61]. Moreover, due to the high demands of storage density, magnetic elements are being patterned more and more densely in arrays. Therefore, another non-negligible interaction is the effect of magnetostatic fields. A direct drawback of these effects is to cause a spread of switching field distribution: the shearing of hysteresis loops and the occurrence of steps can be considered as experimental evidence of such interactions.

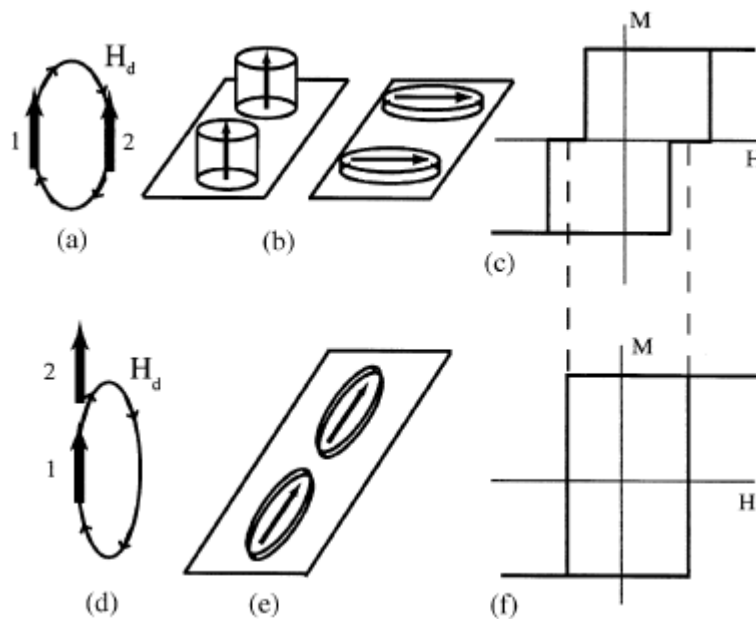


Figure 1.16. Schematic showing the effect of dipole interaction between two magnetic particles [61].

1.2.4. Advances and challenges

Patterned magnetic nanostructures are being researched and developed because of the demand for ultrahigh-density storage technology. As the extension of conventional longitudinal recording, patterned media are well on the way to reach 1 Tbit/in² by continuous scaling-down of bit size and improving noise performance. Moore's Law is the current guideline for the evolution of this technology [10]. However, these developments will eventually approach the physical limits of atomic structures due to thermal instability, or the so-called superparamagnetic limit, where the anisotropy energy K_uV is not sufficiently large enough relative to the environmental thermal energy $k_B T$, and the magnetization becomes randomized losing any stored information. Alternative approaches to circumvent these physical limits are expected to emerge by either utilizing novel materials or via new emerging technologies. Practical engineering issues can intervene to block progress towards the physical limits. For example, inevitable defects during fabrication can cause non-negligible irregularities in device performance, which will result in a tradeoff between the area of patterning and the shape accuracy. Another concern relates the characterization methods and instrumentation. More and more sensitivity is required due to the ongoing miniaturization of recording bit elements. Although micromagnetic simulations can be of great value for designing structures and understanding their magnetic behavior, new analytical methods need to be developed in order to realize better resolution and accuracy, direct visualization, and quantitative data acquisition, as well as demonstrating technical feasibility for industrial applications.

1.3. Magnetic Domain Wall and Related Devices

1.3.1. Racetrack memory

In a magnetic nanowire (NW), the magnetization of each domain should be confined along the long axis of the wire, aligning along one of two possible directions. Domains having two opposite magnetization configurations could be used to represent binary information, and thus precise control of the DW in between the adjacent recording domains (or bits) would enable read/write processes in a NW-based device. Based on this principle, Parkin and co-workers proposed and developed the so-called “racetrack memory” as an emerging technology for non-volatile magnetic random access memory (MRAM) devices [75–77]. In the racetrack memory, the series motion of DWs along a magnetic NW shift register would be controlled using spin-polarized current pulses. The physical effect in current-driven DW motion is based on a spin-momentum transfer torque (or spin torque) that is exerted by spin-polarized conduction electrons on the magnetic moments in the wire, so that the DW would move as the torque rotates the moments. In contrast to current magnetic hard drives where a disk mechanically spins under a head that reads the data stored on the disk at fixed positions, the current pulses would trigger the DW movements electronically to a locally fixed read-out sensor, as illustrated in Figure 1.17 [75]. This novel concept would combine the advantages of both solid-state and magnetic memory devices, and make ultrahigh recording density possible by squeezing the NWs in a three-dimensional (3D) arrangement. However, there are several open questions blocking the transition from theoretical principles to practical technology, which still need better understanding of the physics and materials involved.

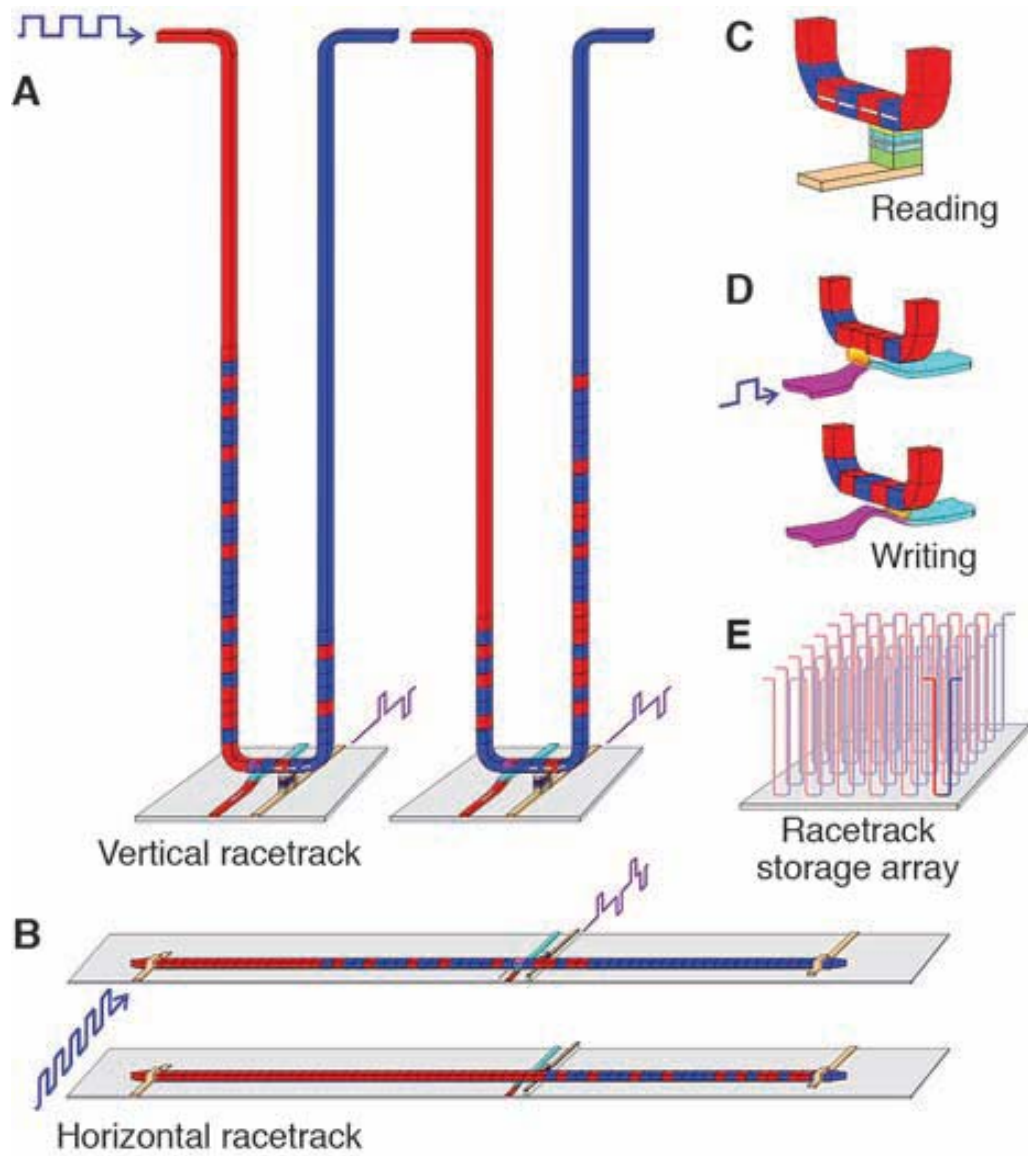


Figure 1.17. Schematic showing principle of racetrack memory using pulse-triggered DW motion along magnetic NWs [75].

1.3.2. Domain-wall logic

Although NW/DW-based devices are being used as memory elements in hard disk and MRAM devices, they are limited to the extent that information can only be stored, but not manipulated in magnetic form. Cowburn and his group expanded the scope and proposed DW logic gates, which would make computation between the magnetic data bits possible [78]. A basic logic gate would be built using one or more ferromagnetic NWs patterned in special designs to realize specific Boolean logic functionality, including AND, NOT, fan-out, and cross-over, as summarized in Figure 1.18 [79]. The underlying principle of these logic gates is to use the swap of DWs as a switch between input and output signals. These basic logic building blocks could be linked together into complex NW networks, and controlled in-plane by an applied oscillating magnetic fields.

In contrast to conventional semiconductor-based logic circuits, these DW logic devices would use no diodes or transistors, and thus offer great potential for an increase in integration density and reduction in power dissipation over current microelectronic technology. The planar layout of the entire NW network would in principle enable numerous layers of such networks to be stacked on top of each other to realize 3D architectures, resulting in dramatic improvement of device minimization. In addition, because the DW logic operations would be carried out by magnetic-field-driven DW motion, current would not be involved, nor would much heating be generated that would cause data switching.

The prospects for these developments appear bright, though there are many questions and issues being discussed. Much in-depth investigation will be needed as the devices are scaled down and integrated with electronic circuits.

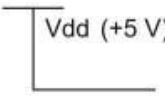
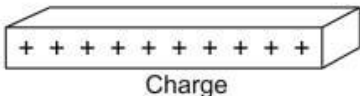

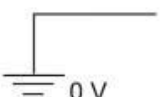
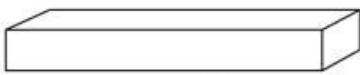
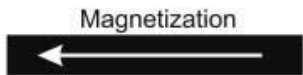
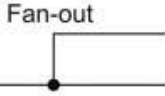
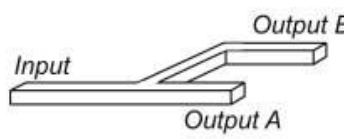
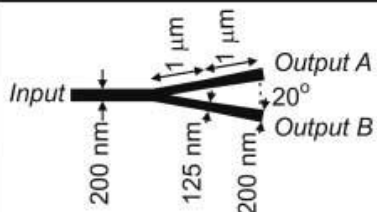
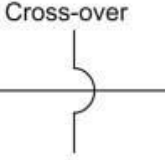
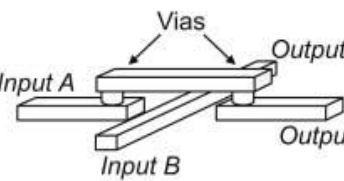
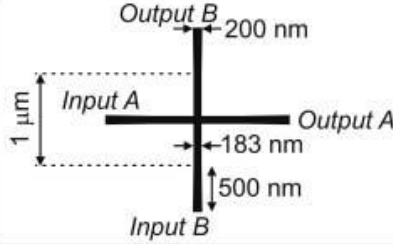
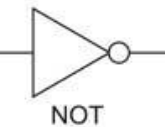
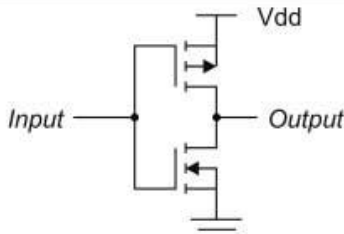
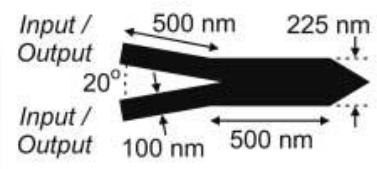
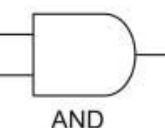
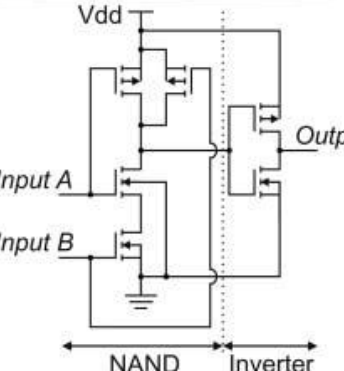
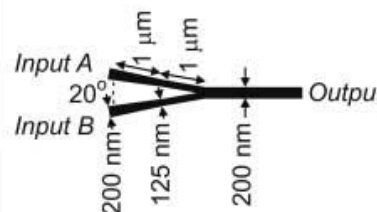
Symbol	CMOS Circuit	Domain Wall Logic Circuit
	 Charge	 Magnetization
	 No charge	 Magnetization
	 Input Output A Output B	 Input Output A Output B
	 Input A Input B Output A Output B Vias	 Input A Output A Input B Output B
 NOT	 Input Output Vdd	 Input / Output Input / Output
 AND	 Input A Input B Output Vdd NAND Inverter	 Input A Input B Output

Figure 1.18. Summary of conventional CMOS circuit elements and corresponding DW logic elements to realize different logic functionalities [79].

1.3.3. Research progress and challenges

A comprehensive understanding of magnetic DW properties is essential for successful development of these memory and logic devices. Relevant research topics include DW propagation and motion (nucleation, injection, pinning, depinning, etc.), driven forces (spin-polarized currents, or magnetic fields), DW types and configurations (transverse/vortex, head-to-head/tail-to-tail), DW velocity, correlation of current (density, pulse length) and DW pinning fields, DW dynamics, and many other aspects [75–88].

Figure 1.19 shows examples of DW motion in Permalloy (Py, $\text{Ni}_{81}\text{Fe}_{19}$) NW or NW networks within racetrack memory and DW logic devices [76, 79]. As indicated in this figure, and oftentimes in the literature, the DW motion is probed by indirect measurements of magnetization hysteresis loops and magnetoresistance (MR) changes of the entire NW or regions distant from the DW interaction site. However, these techniques

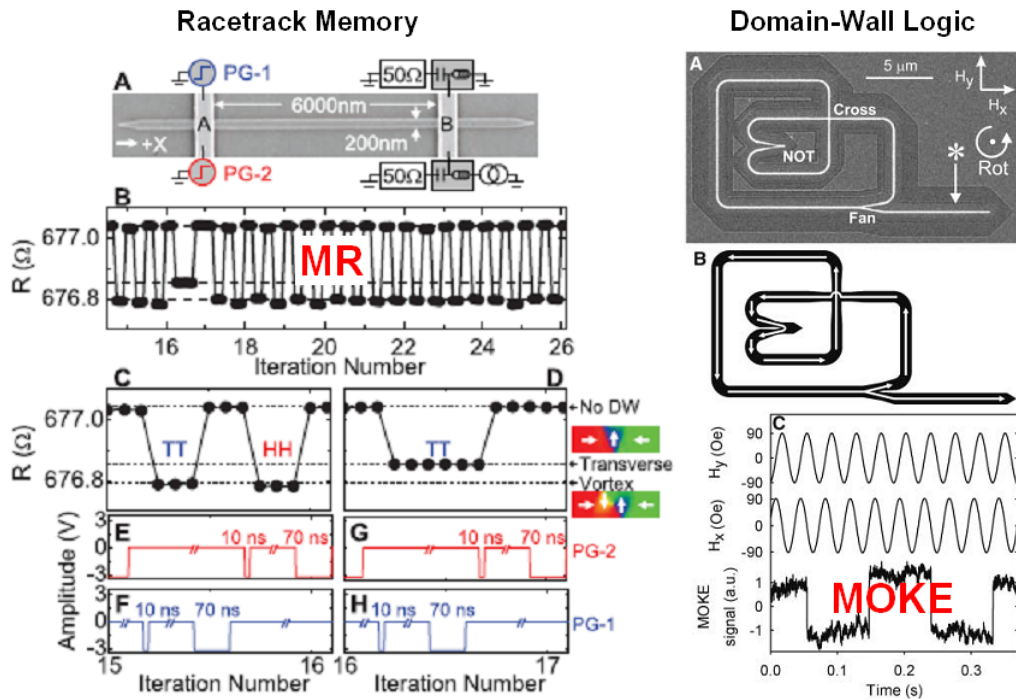


Figure 1.19. Examples of typical studies on racetrack memory and DW logic [76, 79].

lack the ability to provide direct visualization of DW behavior, e.g., type and position. Moreover, quantification and direct observation cannot simultaneously be achieved using these conventional techniques, for studies of both current- and magnetic-field-driven DW propagation. Thus, quantitative nanoscale magnetic imaging is critical to provide basic information about nanomagnetism and spintronic materials.

1.4. Outline of Dissertation

The research of this dissertation has concentrated on quantitative magnetic characterization of patterned magnetic nanostructures and devices using advanced electron microscopy techniques, namely off-axis electron holography, and Lorentz microscopy. The investigation can be roughly separated into three major parts, according to different materials of interest: (i) monolayer Co nanorings; (ii) multilayer spin-valve nanorings; (iii) Py notched nanowires.

Chapter 2 summarizes experimental details of this dissertation research, including nanofabrication, characterization, and micromagnetic simulations.

Chapter 3 shows the results of remanent states and magnetization reversal of Co nanorings with and without slots, where vortex-controlled switching behavior is identified and comparison between observation and simulation is also carried out.

Chapter 4 describes different remanent and switching behaviors of Co/Cu/Py spin-valve nanorings, as a function of the different applied field directions relative to the slot directions. In addition, interlayer coupling and multi-step hysteresis loops are also quantified.

Chapter 5 illustrates DW motion in Py NWs driven by *in situ* magnetic field. DW propagations, including nucleation, injection, pinning and depinning, are directly observed, and critical switching fields are statistically analyzed. A unique asymmetrical

DW pinning behavior is also recognized, depending on DW chirality relative to the sense of rotation around the notch.

Chapter 6 summarizes the important conclusions and advances achieved in this work, as well as providing prospective scope for future studies.

References

- [1] H. C. Oersted, *Annals of Philosophy*. 16, 273 (1820).
- [2] D. Jiles, *Introduction to Magnetism and Magnetic Materials*, Chapman & Hall, London (1998).
- [3] R. C. O'Handley, *Modern Magnetic Materials*, Wiley, New York (2000).
- [4] S. Blundell, *Magnetism in Condensed Matter*, Oxford University Press, New York (2001).
- [5] A. Hubert, R. Schäfer, *Magnetic Domains: the Analysis of Magnetic Microstructures*, Springer-Verlag, Berlin (1998).
- [6] L. D. Landau and E. M. Lifschitz, *Physik Z. Sowjetunion*. 8, 153 (1935).
- [7] O. Smith, *The Electrical World*. 12, 116 (1888).
- [8] F. Engel, *J. Audio Eng. Soc.* 36, 170 (1986).
- [9] H. H. K. Thiele, *J. Audio Eng. Soc.* 36, 396 (1988).
- [10] E. Grochowshi and D. A. Thompson, *IEEE Trans. Magn.* 24, 2476 (1994).
- [11] C. A. Ross, *Annu. Rev. Mater. Res.* 31, 203 (2001).
- [12] A. S. Hoagland, *IEEE Trans. Magn.* 39, 1871 (2003).
- [13] J. J. M. Ruigrok, R. Coehoorn, S. R. Cumpson, and H. W. Kesteren, *J. Appl. Phys.* 87, 5398 (2000).
- [14] J. C. Lodder, *J. Magn. Magn. Mater.* 272–276, 1692 (2004).
- [15] R. P. Cowburn, *J. Phys. D: Appl. Phys.* 33, R1 (2000).
- [16] R. P. Cowburn and M. E. Welland, *Science*. 287, 1466 (2000).
- [17] R. P. Cowburn, *J. Appl. Phys.* 93, 9310 (2003).
- [18] D. K. Koltsov and M. E. Welland, *J. Appl. Phys.* 94, 3457 (2003).
- [19] J. Rothman, M. Kläui, L. Lopez-Diaz, C. A. F. Vaz, A. Bleloch, J. A. C. Bland, Z. Cui, and R. Speaks, *Phys. Rev. Lett.* 86, 1098 (2001).
- [20] S. P. Li, W. S. Lew, J. A. C. Bland, M. Natali, A. Lebib, and Y. Chen, *J. Appl. Phys.* 92, 7397 (2002).
- [21] M. Kläui, C. A. F. Vaz, J. Rothman, J. A. C. Bland, W. Wernsdorfer, G. Faini, and E. Cambri, *Phys. Rev. Lett.* 90, 097202 (2003).

- [22] M. Kläui, C. A. F. Vaz, J. A. C. Bland, L. J. Heyderman, F. Nolting, A. Pavlovska, E. Bauer, S. Cherifi, S. Heun, and A. Locatelli, *Appl. Phys. Lett.* 85, 5637 (2004).
- [23] M. Laufenberg, D. Backes, W. Bühner, D. Bedau, M. Kläui, U. Rüdiger, C. A. F. Vaz, J. A. C. Bland, L. J. Heyderman, F. Nolting, S. Cherifi, A. Locatelli, R. Belkhou, S. Heun, and E. Bauer, *Appl. Phys. Lett.* 88, 052507 (2006).
- [24] Y. B. Xu, A. Hirohata, L. Lopez-Diaz, H. T. Leung, M. Tselepi, S. M. Gardiner, W. Y. Lee, and J. A. C. Bland, *J. Appl. Phys.* 87, 7019 (2000).
- [25] L. J. Heyderman, S. Czekaj, F. Nolting, E. Müller, P. Fischer, Ph. Gasser, and L. Lopez-Diaz, *J. Appl. Phys.* 99, 063904 (2006).
- [26] F. J. Castaño, C. A. Ross, and A. Eilez, *J. Phys. D: Appl. Phys.* 36, 2031 (2003).
- [27] C. A. Ross, F. J. Castaño, E. Rodriguez, S. Haratani, B. Vögeli, and H. I. Smith, *J. Appl. Phys.* 97, 053902 (2005).
- [28] W. Jung, F. J. Castaño, D. Morecroft, C. A. Ross, R. Menon, and H. I. Smith, *J. Appl. Phys.* 97, 10K113 (2005).
- [29] T. Kasama, P. Barpanda, R. E. Dunin-Borkowski, S. B. Newcomb, M. R. McCartney, F. J. Castaño, and C. A. Ross, *J. Appl. Phys.* 98, 013903 (2005).
- [30] K. J. Kirk, J. N. Chapman, and C. D. W. Wilkinson, *J. Appl. Phys.* 85, 5237 (1999).
- [31] R. D. Gomez, T. V. Luu, A. O. Pak, K. J. Kirk, and J. N. Chapman, *J. Appl. Phys.* 85, 6163 (1999).
- [32] K. J. Kirk, S. McVitie, J. N. Chapman, and C. D. W. Wilkinson, *J. Appl. Phys.* 89, 7174 (2001).
- [33] K. J. Kirk, M. R. Scheinfein, J. N. Chapman, S. McVitie, M. F. Gillies, B. R. Ward, and J. G. Tennant, *J. Phys. D: Appl. Phys.* 34, 160 (2001).
- [34] X. Liu, J. N. Chapman, S. McVitie, and C. D. W. Wilkinson, *Appl. Phys. Lett.* 84, 4406 (2004).
- [35] X. Liu, J. N. Chapman, S. McVitie, and C. D. W. Wilkinson, *J. Appl. Phys.* 96, 5173 (2004).
- [36] M. H. Park, Y. K. Hong, S. H. Gee, D. W. Erickson, and B. C. Choi, *Appl. Phys. Lett.* 83, 329 (2003).
- [37] M. H. Park, Y. K. Hong, S. H. Gee, D. W. Erickson, T. Tanaka, and B. C. Choi, *J. Appl. Phys.* 95, 7019 (2004).
- [38] B. R. Pujada, J. Svendsen, K. O. Chipeniuk, B. C. Choi, M. H. Park, Y. K. Hong,

- S. H. Gee, and D. W. Erickson, *J. Appl. Phys.* 96, 4362 (2004).
- [39] B. C. Choi, J. Ho, Y. K. Hong, M. H. Park, H. Han, S. H. Gee, and G. W. Donohoe, *IEEE Trans. Magn.* 41, 2709 (2005).
- [40] B. R. Pujada, B. C. Choi, M. H. Park, Y. K. Hong, S. H. Gee, H. Han, and G. W. Donohoe, *J. Appl. Phys.* 97, 073904 (2005).
- [41] B. C. Choi, B. R. Pujada, Y. K. Hong, M. H. Park, H. Han, S. H. Gee, and G. W. Donohoe, *IEEE Trans. Magn.* 41, 3109 (2005).
- [42] H. Han, Y. K. Hong, M. H. Park, B. C. Choi, S. H. Gee, J. F. Jabal, G. Abo, A. Lyle, B. Wong, and G. W. Donohoe, *IEEE Trans. Magn.* 41, 4341 (2005).
- [43] R. E. Dunin-Borkowski, M. R. McCartney, B. Kardynal, and D. J. Smith, *J. Appl. Phys.* 84, 374 (1998).
- [44] D. J. Smith, R. E. Dunin-Borkowski, M. R. McCartney, B. Kardynal, and M. R. Scheinfein, *J. Appl. Phys.* 87, 7400 (2000).
- [45] R. E. Dunin-Borkowski, M. R. McCartney, B. Kardynal, M. R. Scheinfein, and D. J. Smith, *J. Microsc.* 200, 187 (2000).
- [46] R. E. Dunin-Borkowski, M. R. McCartney, B. Kardynal, M. R. Scheinfein, D. J. Smith, and S. S. P. Parkin, *J. Appl. Phys.* 90, 2899 (2001).
- [47] H. Hu, H. Wang, M. R. McCartney, and D. J. Smith, *J. Magn. Magn. Mater.* 290-291, 234 (2005).
- [48] H. Hu, H. Wang, M. R. McCartney, and D. J. Smith, *J. Appl. Phys.* 97, 054305 (2005).
- [49] H. Wang, H. Hu, M. R. McCartney, and D. J. Smith, *J. Magn. Magn. Mater.* 303, 237 (2006).
- [50] H. Hu, H. Wang, M. R. McCartney, and D. J. Smith, *Phys. Rev. B* 73, 153401 (2006).
- [51] N. Agarwal, H. Wang, D. J. Smith, and M. R. McCartney, *IEEE Trans. Magn.* 42, 2414 (2006).
- [52] N. Agarwal, M. R. McCartney, and D. J. Smith, *J. Appl. Phys.* 102, 023911 (2007).
- [53] K. S. Buchanan, P. E. Roy, M. Grimsditch, F. Y. Frandini, K. Yu. Guslienko, S. D. Bader, and V. Novosad, *Nature Phys.* 1, 172, (2005).
- [54] J. M. García, A. Asenjo, J. Velázquez, D. García, M. Vázquez, P. Aranda, and E. Ruiz-Hitzky, *J. Appl. Phys.* 85, 5480 (1999).
- [55] R. M. Metzger, V. V. Konovalov, M. Sun, T. Xu, G. Zangari, B. Xu, M. Benakli,

- and W. D. Doyle, *IEEE Trans. Magn.* 36, 30 (2000).
- [56] M. Sun, G. Zangari, M. Shamsuzzoha, and R. M. Metzger, *Appl. Phys. Lett.* 78, 2964 (2001).
- [57] S. H. Sun, C. B. Murray, D. Weller, L. Folks, and A. Moser, *Science*. 287, 1989 (2000).
- [58] S. H. Sun, E. E. Fullerton, D. Weller, and C. B. Murray, *IEEE Trans. Magn.* 37, 1239 (2001).
- [59] A. Moser, K. Takano, D. T. Margulies, M. Albrecht, Y. Sonobe, Y. Ikeda, S. H. Sun, and E. E. Fullerton, *J. Phys. D: Appl. Phys.* 35, R157 (2002).
- [60] B. D. Terris and T. Thomson, *J. Phys. D: Appl. Phys.* 38, R199 (2005).
- [61] J. I. Martín, J. Nogués, K. Liu, J. L. Vicente, and I. K. Schuller, *J. Magn. Magn. Mater.* 256, 449 (2003).
- [62] D. A. Allwood, G. Xiong, M. D. Cooke, and R. P. Cowburn, *J. Phys. D: Appl. Phys.* 36, 2175 (2003).
- [63] Z. Q. Qiu and S. D. Bader, *Rev. Sci. Instrum.* 71, 1243 (2000).
- [64] M. Grimsditch and P. Vavassori, *J. Phys.: Condens. Matter* 16, R275 (2004).
- [65] Y. Martin and H. K. Wickramasinghe, *Appl. Phys. Lett.* 50, 1455 (1987).
- [66] D. Rugar, H. J. Mamin, P. Guethner, S. E. Lambert, J. E. Stern, I. McFayden, and T. Yogi, *J. Appl. Phys.* 68, 1169 (1990).
- [67] A. Wadas and P. Grütter, *Phys. Rev. B* 39, 12013 (1989).
- [68] M. R. Scheinfein, J. Unguris, M. H. Kelley, D. T. Pierce, and R. J. Celotta, *Rev. Sci. Instrum.* 61, 2501 (1990).
- [69] S. Anders, H. A. Padmore, R. M. Duarte, T. Renner, T. Stammner, A. Schöll, M. R. Scheinfein, J. Stohr, L. Séve, and B. Sinkovic, *Rev. Sci. Instrum.* 70, 3973 (1999).
- [70] T. Taniuchi, M. Oshima, H. Akinaga, and K. Ono, *J. Appl. Phys.* 97, 10J904 (2005).
- [71] X. F. Han, M. Grimsditch, J. Meersschat, A. Hoffmann, Y. Ji, J. Sort, J. Nogue's, R. Divan, J. E. Pearson, and D. J. Keavney, *Phys. Rev. Lett.* 98, 147202 (2007).
- [72] V. Uhlíř, S. Pizzini, N. Rougemaille, J. Novotný, V. Cros, E. Jiménez, G. Faini, L. Heyne, F. Sirotti, C. Tieg, A. Bendounan, F. Maccherozzi, R. Belkhou, J. Grollier, A. Anane, and J. Vogel, *Phys. Rev. B* 81, 224418 (2010).

- [73] R. P. Cowburn, D. K. Koltsov, A. O. Adeyeye, M. E. Welland, and D. M. Tricker, *Phys. Rev. Lett.* 83, 1042 (1999).
- [74] C. C. Chang, Y. C. Chang, W. S. Chung, J. C. Wu, Z. H. Wei, M. F. Lai, and C. R. Chang, *IEEE Trans. Magn.* 41, 947 (2005).
- [75] S. S. P. Parkin, M. Hayashi, and L. Thomas, *Science* 320, 190 (2008).
- [76] M. Hayashi, L. Thomas, R. Moriya, C. Rettner, and S. S. P. Parkin, *Science* 320, 209 (2008).
- [77] M. Hayashi, L. Thomas, R. Moriya, C. Rettner, X. Jiang, and S. S. P. Parkin, *Phys. Rev. Lett.* 97, 207205 (2006).
- [78] D. A. Allwood, G. Xiong, C. C. Faulkner, D. Atkinson, D. Petit, and R. P. Cowburn, *Science* 306, 1688 (2005).
- [79] D. A. Allwood, Gang Xiong, M. D. Cooke, C. C. Faulkner, D. Atkinson, N. Vernier, and R. P. Cowburn, *Science*, 296, 2003 (2002).
- [80] D. Petit, A.V. Jausovec, D. Read, and R. P. Cowburn, *J. Appl. Phys.* 103, 114307 (2008).
- [81] H. T. Zeng, D. Read, D. Petit, A.V. Jausovec, L. O'Brien, E.R. Lewis, and R. P. Cowburn, *Appl. Phys. Lett.* 94, 103113 (2009).
- [82] D. McGrouther, S. McVitie, and J. N. Chapman, *Appl. Phys. Lett.* 91, 022506 (2007).
- [83] K. J. O'Shea, S. McVitie, J. N. Chapman, and J. M. R. Weaver, *Appl. Phys. Lett.* 93, 202505 (2008).
- [84] S. Lepadatu, A. Vanhaverbeke, D. Atkinson, R. Allenspach, and C. H. Marrows, *Phys. Rev. Lett.* 102, 127203 (2009).
- [85] W. C. Uhlig, M. J. Donahue, D. T. Pierce, and J. Unguris, *J. Appl. Phys.* 105, 103902 (2009).
- [86] M. Y. Im, L. Bocklage, P. Fischer, and G. Meier, *Phys. Rev. Lett.* 102, 147204 (2009).
- [87] A. Yamaguchi, T. Ono, S. Nasu, K. Miyake, K. Mibu, and T. Shinjo, *Phys. Rev. Lett.* 92, 077205 (2004).
- [88] T. A. Moore, M. Kläui, L. Heyne, P. Möhrke, D. Backes, J. Rhensius, U. Rüdiger, L. J. Heyderman, T. O.Mentes, M. A. Nino, A. Locatelli, A. Potenza, H. Marchetto, S. Cavill, and S. S. Dhesi, *J. Magn. Mater.* 322, 1347 (2010).

CHAPTER 2

EXPERIMENTAL DETAILS

This chapter provides detailed information about the facilities and instruments, as well as the procedures of sample preparation and characterization, that were involved in this dissertation research. The chapter also describes the principle of micromagnetic modeling and the essential materials parameters used for typical simulations. Details about electron hologram acquisition, phase reconstruction, quantification, and magnetic representation are introduced, followed by several practical examples of quantitative phase imaging of magnetic fields in different materials.

2.1. Instrumentation

2.1.1. Electron beam lithography

A typical EBL system consists of the following parts: (i) electron source that supplies electrons; (ii) column of electron lenses and deflection coils that control and focus the electron beam; (iii) mechanical stage that positions the sample under the electron beam; and (iv) computer system that controls the instrument [1].

The JEOL JBX-6000FS/E EBL system located in the Center for Solid State Electronics Research (CSSER) has been used in this research. This instrument is a vector-scanning-type EBL system which has two operation modes: the 4th-lens mode and the 5th-lens mode. The former mode is used for submicron lithography while the latter mode is used for ultra-fine lithography. The lens system consists of two intermediate lenses (2nd and 3rd lenses) and one objective lens (4th or 5th lens), as shown in Figure 2.1. A high-brightness electron gun using zirconium-oxide-coated tungsten thermal-field-emitter (ZrO/W TFE) and an in-lens deflector has been employed. The acceleration voltage is

usually set at 50 kV. In the 5th-lens mode, the electron beam has a minimum spot diameter of 5 nm. Workpiece stage movement is driven by the step-and-repeat method, with the stage position increment of 0.62 nm controlled by a laser interferometer.

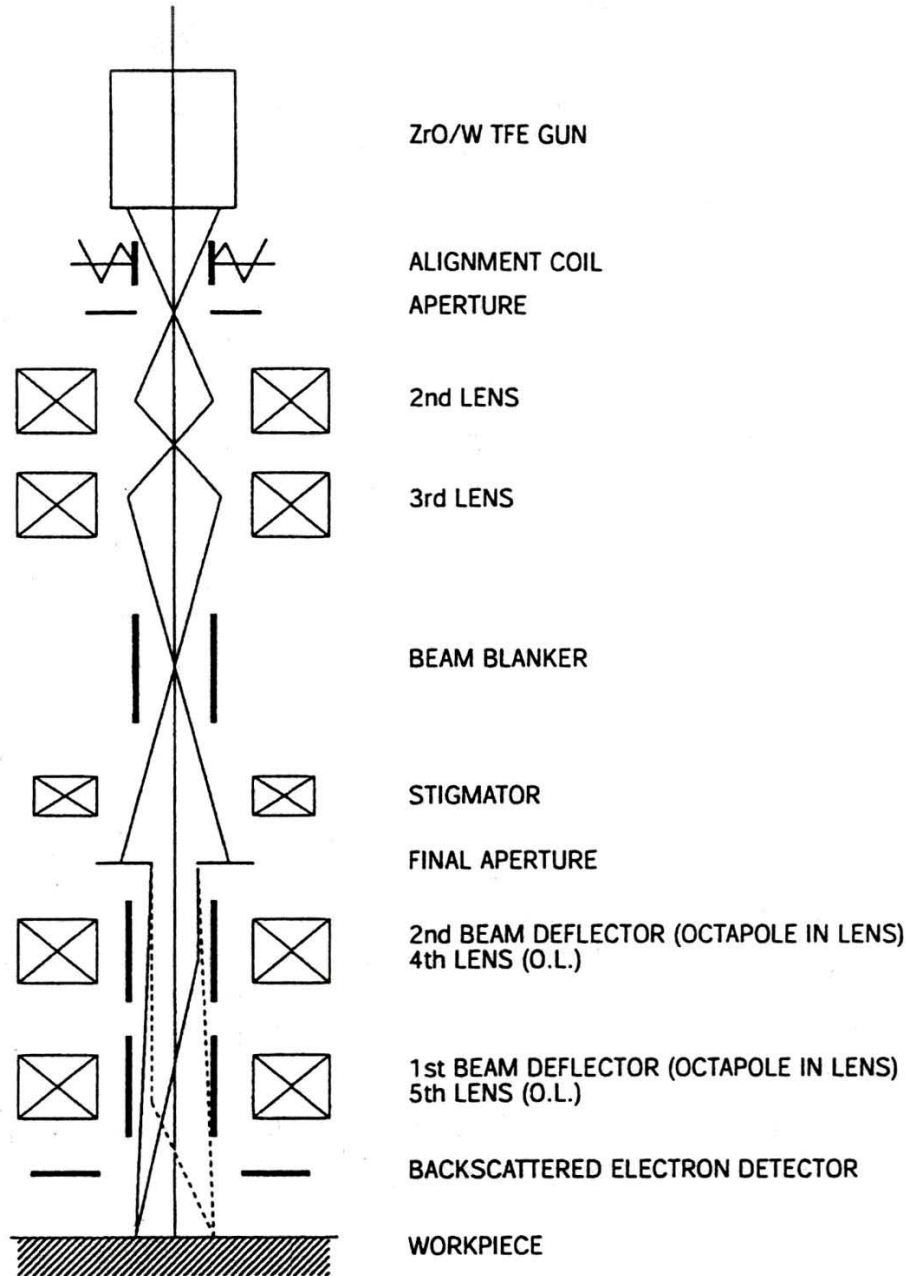


Figure 2.1. Electron optics system of JBX-6000FS/E [1].

2.1.2. Transmission electron microscopy

Transmission electron microscopy (TEM) is an imaging technique that allows high-resolution observation of materials at the atomic scale. Inside the TEM column, a beam of electrons is emitted by an electron gun, accelerated by high voltage (usually 100–400 kV), focused by electrostatic or electromagnetic lenses, and then transmitted through an ultrathin specimen, interacting with the specimen as it passes through. An image is formed by an objective lens from the electrons transmitted through the specimen, which is then magnified onto the final imaging screen or detector. Images can be viewed on a fluorescent screen, and recorded by photographic film, or a charge-coupled device (CCD) camera. A typical TEM is schematically shown in Figure 2.2.

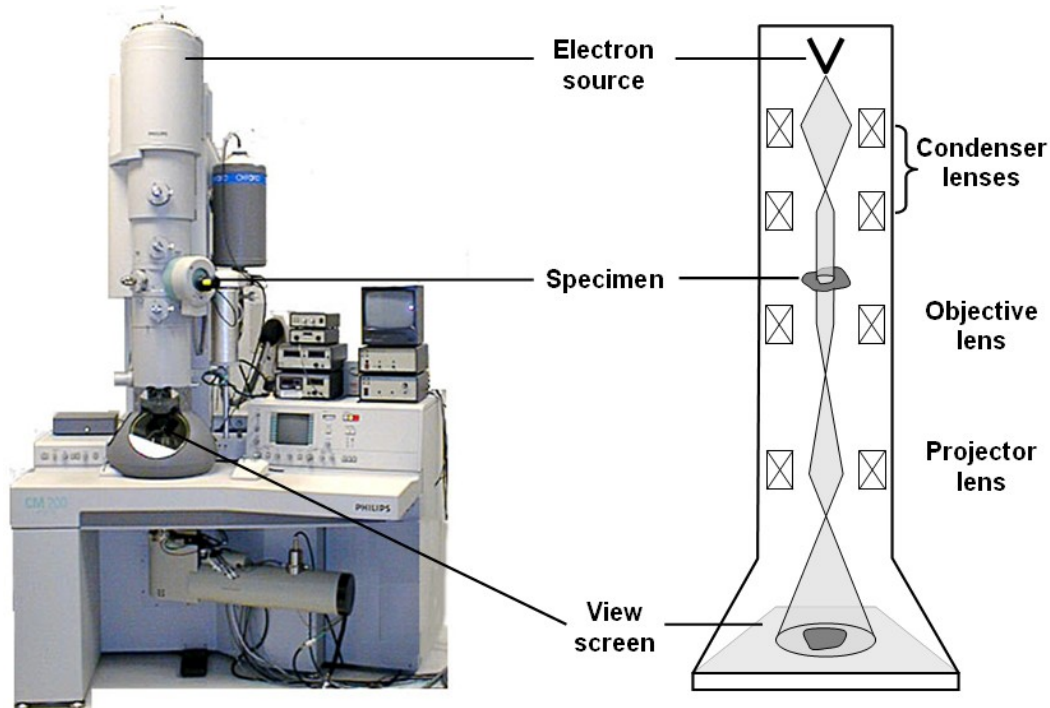


Figure 2.2. Schematic for a TEM and its electron optics scheme.

The Philips-FEI CM200-FEG TEM in the John M. Cowley Center for High Resolution Electron Microscopy (CHREM) has been used in this research. This TEM is normally operated at 200 kV, and it is equipped with a Schottky field-emission gun (FEG) to provide highly coherent electron illumination, an electrostatic biprism located in the selected-area aperture plane to enable the function of electron holography, and a 1024×1024 pixel Gatan 794 slow-scan CCD camera (later updated to a Gatan Orius SC600 with 2680×2688 pixels) for digital recording. A special minilens (so-called Lorentz lens, with $C_s = 8$ m and 1.2 nm line resolution at 200 kV) located in the bore of the objective lens pole-piece, allows images to be obtained at magnifications of up to 50kx with the main objective lens switched off and the sample located in almost field-free conditions. In addition, an X-ray detector and an energy-selecting Gatan imaging filter (GIF) are also attached to provide analytical characterization, such as energy-dispersive X-ray spectroscopy (EDS) and electron-energy-loss spectroscopy (EELS).

2.2. Fabrication

Ferromagnetic nano-elements with different shapes can be fabricated by direct patterning onto 50-nm-thick self-supporting electron-transparent 500×500μm silicon-nitride TEM membrane windows using the EBL technique and a standard lift-off process [2]. The processing was carried out in the CSSER class-100 cleanroom. Figure 2.3 illustrates the geometry of the membrane samples used as substrates, with (a) top view, (b) side view, and (c) actual image, respectively.

Before EBL processing, the desired shapes and distribution of the nanopatterned arrays were written into data files using a combination of auto-computer-aided design (Auto-CAD) software and JEOL machine code. The pattern data files were then converted to the internal format of the EBL machine codes and debugged free of any

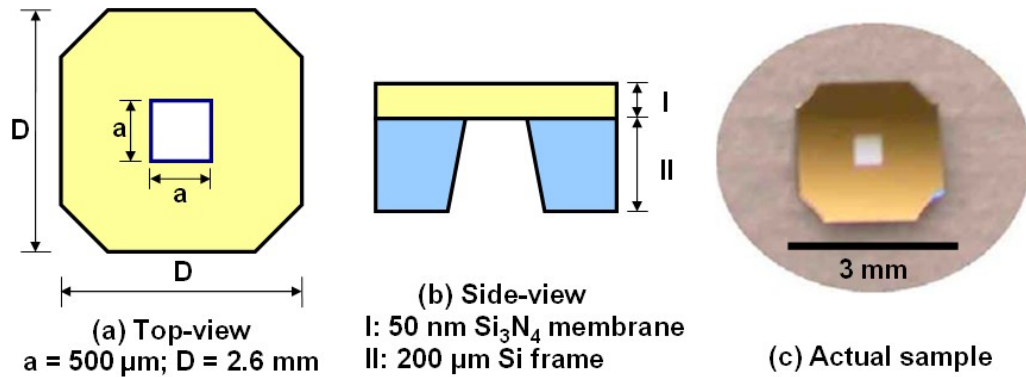


Figure 2.3. Schematics showing the geometry and dimensions of the membrane samples: (a) top view; (b) side view. (c) Actual image.

errors before exposure to the electron beam took place. One or two corner points of the sample were usually used as reference marks to obtain the offset required for locating the patterns on the membrane window. A few scratches were drawn on the frame to help in fine-focusing of the sample surface during alignment of the EBL system.

Figure 2.4 illustrates the major processing steps during EBL fabrication. The silicon nitride membranes were pre-cleaned in warm acetone for 15 minutes and then rinsed in isopropyl alcohol (IPA) for 5 minutes, followed by nitrogen blow-drying. The cleaning process ensured that the Si_3N_4 membranes were free from any contamination. A 2% polymethyl-methacrylate (PMMA) (in chlorobenzene) solution was spun at 5000 rpm for 30 seconds onto the Si_3N_4 membranes, and then baked at 170°C in an oven for 1–2 hours. The baking time had to be long enough to ensure that the polymer resist was fully baked and did not disintegrate catastrophically when exposed to the high-energy electron beam. According to the pre-calibration curve of resist thickness as function of spin speed, about 100-nm thickness of PMMA layer was obtained on the membranes after baking. This PMMA thickness is a tradeoff between the preference for a thin resist layer required

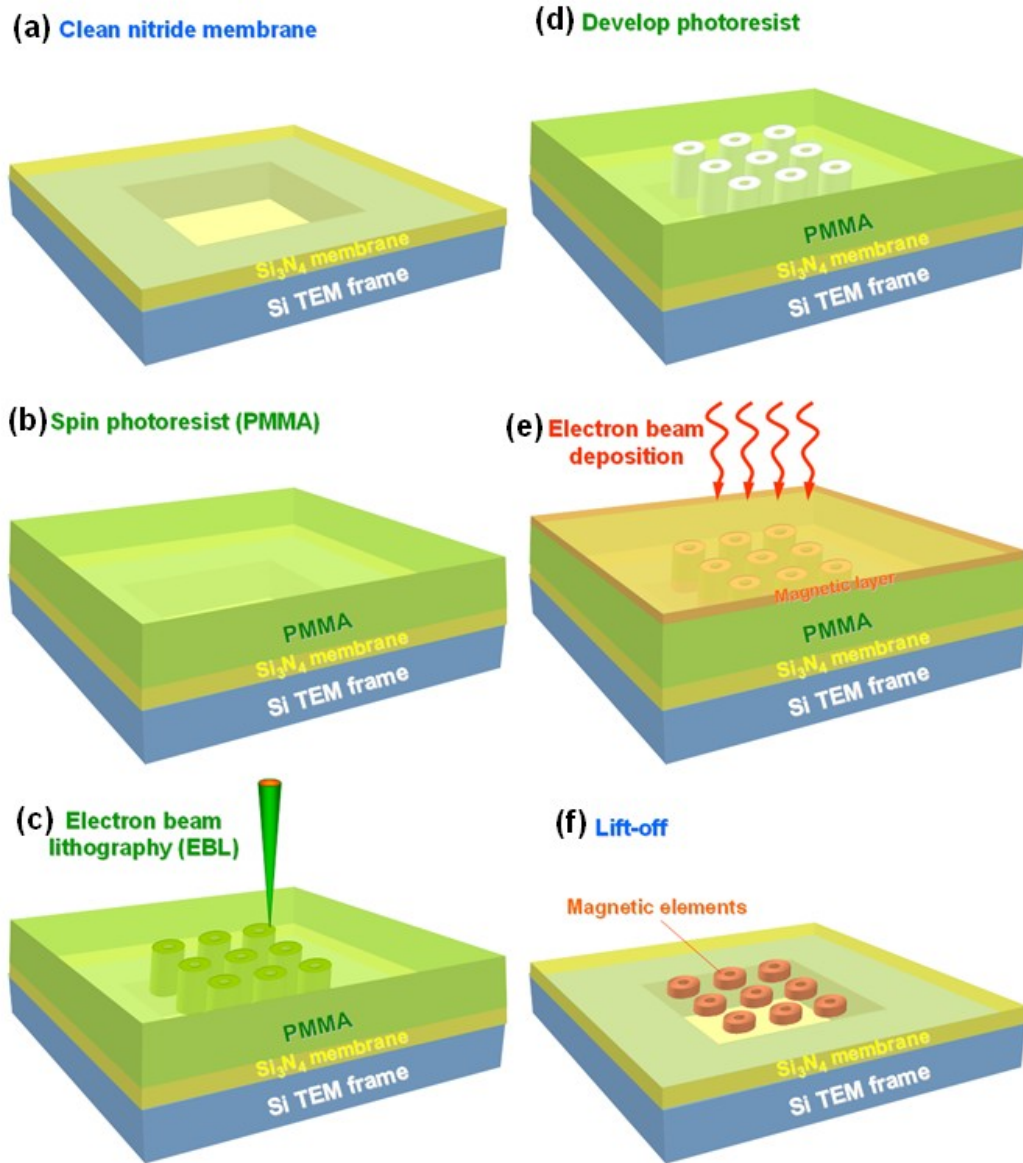


Figure 2.4. Schematic outline of EBL process: (a) cleaning membrane; (b) spinning and baking PMMA; (c) EBL exposure; (d) resist development; (e) deposition of magnetic material; (f) lift off.

by the high-resolution EBL pattern writing, and the requirement that the thickness of the resist layer should be at least 3 times thicker than the metal layer to be deposited in order to facilitate the lift-off process. This cap on the maximum resist thickness limits the scope for depositing multilayer structures with total stack heights exceeding 30 nm.

A very high area dose, $800 \mu\text{C}/\text{cm}^2$, was normally used to expose the patterns. This very high dose was essential because of the reduced backscattering and secondary electron yield from the very thin Si_3N_4 support membranes relative to a standard Si wafer. The exposed membranes were developed in a solution of 11 : 10 : 1 methyl isobutyl ketone : cellusol : methyl alcohol for 15 seconds, stopped by soaking in IPA for 20 seconds, and followed by blow-drying in nitrogen. The PMMA on the exposed areas was removed completely after these steps. Particular caution was needed for handling the nitride membrane windows during processing due to the extreme low strength and high sensitivity to pressure or stress.

Ferromagnetic thin films were then deposited on the Si_3N_4 membranes using an electron-beam evaporator (TorrVac VC-320) at a typical vacuum pressure of 3×10^{-6} Torr, usually followed by deposition of a 2-nm-thick Al layer to avoid surface oxidation. The deposition rate was kept as low as $\sim 0.5 \text{ \AA}$ per second. This slow deposition rate normally ensured uniform deposition. As-deposited samples were lifted off using Microstrip 2001 (a commercial solvent) at 70°C for 4–5 hours to remove unwanted PMMA and the overlying materials, and the expected elements were left on the membrane windows. After completion of the lift-off process, another layer of 2–3 nm Ti was deposited onto the nitride membrane, using a separate thin-film deposition system under very high vacuum, as a final step to prevent electrostatic charging during TEM observation.

2.3. Micromagnetic Simulations

Micromagnetism is a classical theory for the treatment of magnetization processes in ferromagnetic materials, and deals with the interactions between magnetic moments on sub-micrometer length scales. These interactions are governed by several competing energy terms: (i) magnetostatic energy (E_S) or demagnetization energy (E_{demag}), which originates from the classical long-range interactions between magnetic dipoles within the object; (ii) exchange energy (E_{ex}), which aligns the magnetic moments in the short range parallel or anti-parallel to each other; (iii) magnetocrystalline anisotropy energy (E_K), which correlates magnetization and crystal lattice, and orients the magnetization preferentially along certain crystallographic directions; and (iv) Zeeman energy (E_H), which rotates magnetic moments parallel to an external magnetic field. Thus, the total magnetic Gibbs free energy of the system can be expressed as:

$$E_{total} = E_S + E_{ex} + E_K + E_H \quad (2.1)$$

Numerical micromagnetic simulations, based on either finite difference or finite element methods, can resolve local arrangements of the magnetization in static situations, as well as its dynamic evolution as a function of time. The space and time resolution is on the order of nanometers and nanoseconds, respectively. For static problems where thermal fluctuations and dynamic effects are usually neglected, micromagnetic simulations start from the minimization of the total Gibbs free energy to determine the stable equilibrium states for static problems. In order to study the time-dependent dynamic response to an applied field, the Gilbert equation of motion has to be taken into account [4]:

$$\frac{\partial \mathbf{M}}{\partial t} = -|\gamma| \mathbf{M} \times \mathbf{H}_{\text{eff}} + \alpha \frac{\mathbf{M}}{M_s} \times \frac{\partial \mathbf{M}}{\partial t} \quad (2.2)$$

where γ is the gyromagnetic ratio $|\gamma| = 2.210175 \times 10^5$ m/As, α is dimensionless Gilbert

damping constant, \mathbf{H}_{eff} is effective magnetic field. This equation modifies the Landau-Lifshitz ordinary differential equation [5] by replacing the damping term, and is mathematically equivalent to the Landau-Lifshitz-Gilbert (LLG) equation:

$$\frac{\partial \mathbf{M}}{\partial t} = -\frac{|\gamma|}{1+\alpha^2} \mathbf{M} \times \mathbf{H}_{\text{eff}} - \frac{|\gamma| \alpha}{1+\alpha^2} \frac{\mathbf{M}}{M_S} \times \mathbf{M} \times \mathbf{H}_{\text{eff}} \quad (2.3)$$

In the present research, we used the object-oriented micromagnetic framework (OOMMF) software package that was developed by Donahue and Porter from National Institute of Standards and Technology (NIST) [6]. OOMMF is an open-source simulation tool based on algorithm of finite difference lattice discretizations of space and FFT. The codes are written in C++ with a Tcl/Tk algorithm interface, which provides much portability and flexibility to users.

In practical simulations, geometrical and structural parameters of the magnetic materials are obtained from TEM and electron holography measurements. Other intrinsic and technical parameters are listed in Table 2.1.

Table 2.1. Essential parameters used for practical micromagnetic simulations.

Parameters	Co	Py
Saturation magnetization (M_S : A/m)	1.4×10^6	8.6×10^5
Exchange stiffness (A: J/m)	3.0×10^{-11}	1.3×10^{-11}
Uniaxial anisotropy constant (K_1 : J/m ³)	6×10^3	—
Damping constant	0.5	0.5
Cell size (nm ³)	$5 \times 5 \times 5$	$5 \times 5 \times 5$

2.4. Characterization

2.4.1. Lorentz microscopy

Standard TEMs are not well equipped for the study of magnetic materials because the specimen is immersed in the magnetic field of the objective lens, which is usually sufficiently strong ($\sim 1.5\text{--}2$ T) to saturate the material and thus destroy any domain structure of interest. In contrast, Lorentz TEM can provide a field-free environment for imaging of magnetic materials when the normal objective lens is completely switched off. Lorentz microscopy has been used for several decades to study magnetic domain structures and magnetization reversal mechanisms in magnetic thin films and nanomagnets [7].

The interaction of electrons passing through a region of magnetic induction in the specimen can result in magnetic image contrast, because of the deflection, as indicated in Figure 2.5 (a), experienced by electrons, as determined by the Lorentz force:

$$\vec{F}_L = -e(\vec{v} \times \vec{B}) \quad (2.4)$$

where \vec{F}_L is the Lorentz force acting on an electron with elementary charge e traveling with velocity \vec{v} , and \vec{B} is the magnetic induction averaged along the electron trajectory. The direction of the vector product obeys the right-hand rule.

There are several modes of Lorentz microscopy including Fresnel mode, Foucault mode, and differential phase contrast (DPC) mode [8, 9]. In our experiments, the Fresnel imaging mode was normally used, with the Lorentz minilens defocused so that an out-of-focus image of the specimen was formed. Under these conditions, magnetic domain walls were imaged as alternate bright (convergent) and dark (divergent) lines, as shown in Figure 2.5 (b). This imaging mode is more powerful when a magnetic field is applied *in situ* so that magnetization reversal processes can be observed rather than just

imaging a static domain structure. Application of a magnetic field can be realized by tilting the specimen holder in the small vertical field caused by the partially excited objective lens. Although Lorentz TEM oftentimes offers straightforward image interpretation about magnetic information on domain and DW structures, there are still significant drawbacks of using the Fresnel mode. Quantitative information is difficult to obtain, and the direction of magnetization within any single domain cannot be easily inferred. In addition, for multilayered materials, there is no simple way of separating contributions to the images arising from the individual layers.

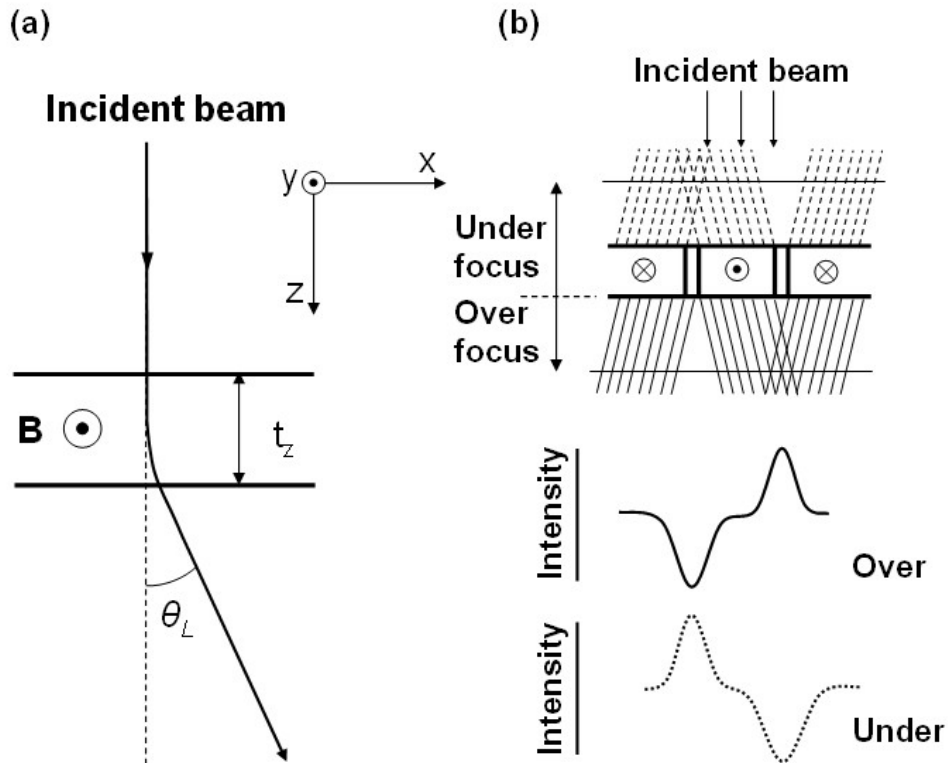


Figure 2.5. Schematic of (a) Lorentz force, and (b) Fresnel Lorentz imaging. Electrons passing through the magnetic sample are deflected due to the in-plane magnetic field, and form DW magnetic contrast at under- or over-focus conditions [9].

2.4.2. Off-axis electron holography

Electron holography was initially proposed by Gabor as a means to overcome the limitation of TEM resolution caused by the unavoidable aberrations of electromagnetic lenses [10, 11]. In contrast to conventional TEM imaging, which can only record the intensity of the electron wave passing through the specimen without any direct phase information, electron holography provides a unique method for detecting the phase change of the electron wave due to magnetic and electrical fields [9, 12–14]. The technique of electron holography depends on the interference of two (or more) coherent electron waves that combine to produce an interferogram or hologram. Off-axis electron holography is the holography mode most commonly used.

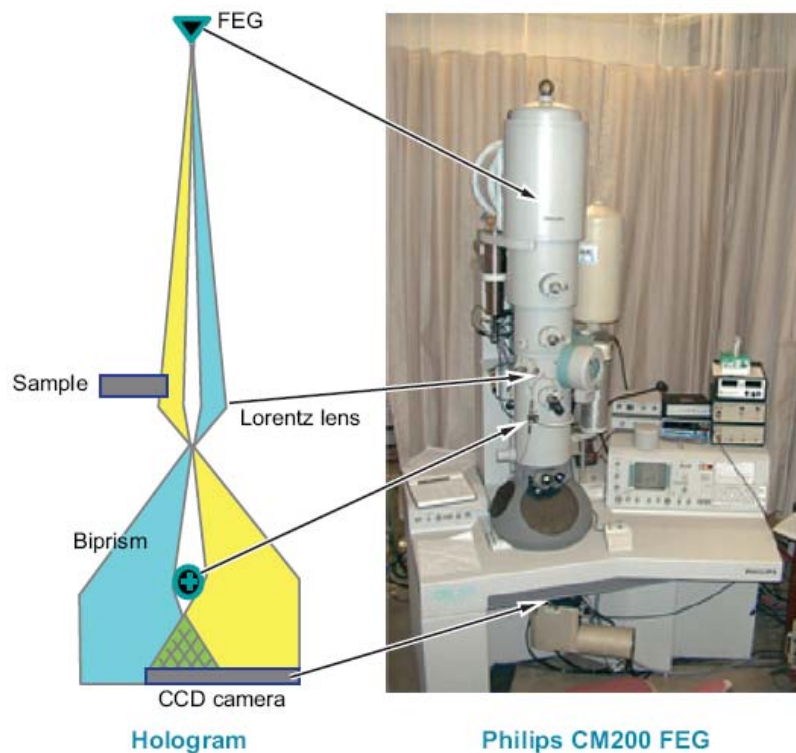


Figure 2.6. Schematic illustrating the typical configuration used for off-axis electron holography in the TEM (Philips CM200-FEG) [14].

There are three essential components for practical implementation of electron holography, as illustrated in Figure 2.6: the field-emission gun (FEG) to provide coherent incident illumination, the electrostatic biprism located below the sample to overlap the scattered (object) wave with a vacuum (reference) wave to produce an interference pattern, and the CCD camera required for quantitative recording of holograms.

Omitting the complicated electro-optics imaging theory and detailed mathematical evolution that can be found in many papers [12–16], we come directly to some basic equations that describe the formation of electron holograms. The phase shift of an electron wave that has passed through the sample, relative to the wave that has passed only through vacuum, is given in one dimension by

$$\phi(x) = C_E \int V_0(x, z) dz - \frac{e}{\hbar} \iint B_{\perp}(x, z) dx dz \quad (2.5)$$

where z is the incident beam direction, x is a direction in the plane of the sample, V_0 is the mean inner potential (MIP), B_{\perp} is the component of the magnetic induction perpendicular to both x and z , and C_E is an interaction constant, which depends on the energy of the incident electron beam.

If neither V_0 nor B_{\perp} varies with z within the sample thickness t , and provided that any electrostatic or magnetic fringing fields outside the sample are negligible, then this expression can be simplified to:

$$\phi(x) = C_E V_0(x) t(x) - \frac{e}{\hbar} \int B_{\perp}(x) t(x) dx \quad (2.6)$$

Differentiation with respect to x leads to an expression for the phase gradient of

$$\frac{d\phi(x)}{dx} = C_E \frac{d}{dx} [V_0(x) t(x)] - \frac{e}{\hbar} B_{\perp}(x) t(x) \quad (2.7)$$

Equations (2.6) and (2.7) are fundamental to the measurement and quantification of

electrostatic and magnetic fields using electron holography for phase imaging, as schematically illustrated in Figure 2.7. In practical studies of magnetic materials, the contribution to phase shifts can be due to both MIP and magnetism. Thus, a straightforward understanding of magnetic field needs to resolve uncertain factors relevant to the MIP, for instance, by using simple sample geometry.

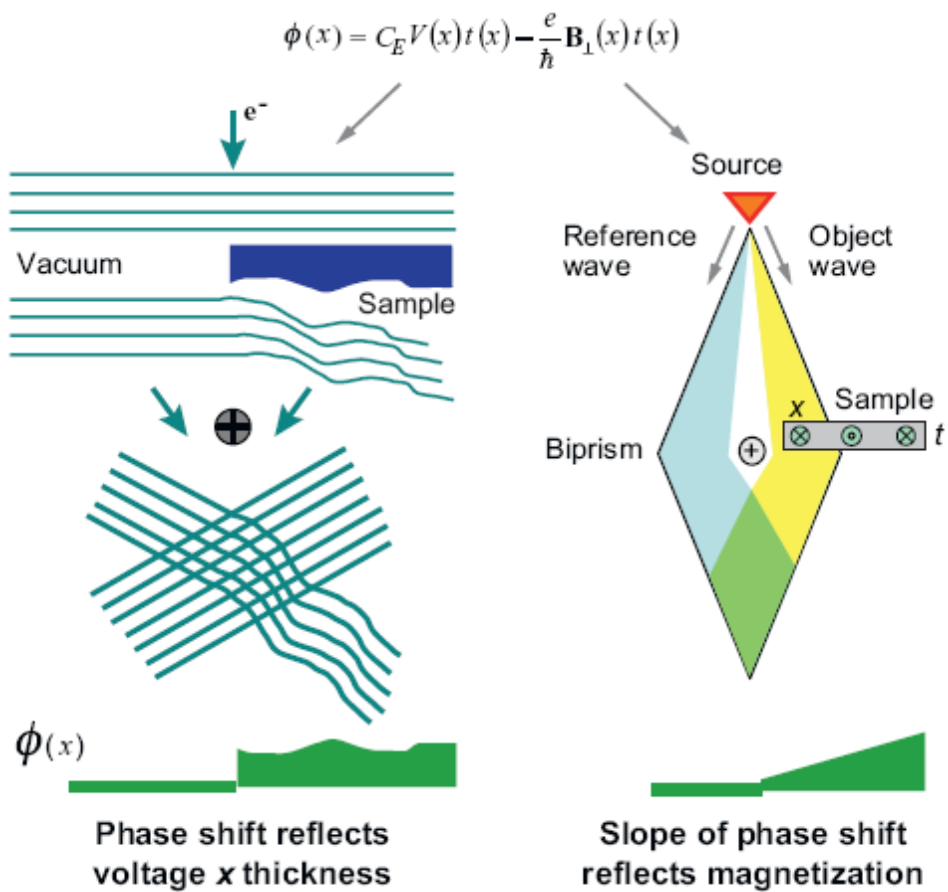


Figure 2.7. Schematic illustration contrasting the origin of phase shifts for holography of electrostatic and magnetic fields [14].

For samples of uniform thickness and composition, the first term in Equation (2.7) is zero, and thus the phase gradient is proportional to the in-plane magnetic induction. However, the MIP term $[V_0(x)t(x)]$ is likely to dominate both the phase and the phase gradient, complicating attempts to quantify the magnetization within the sample. Theoretically, the holographic amplitude image can be used to estimate the MIP contribution to the phase. However, this is difficult to do in practice due to lack of calibration of the mean-free-path for inelastic scattering of each material, as well as noise resulting from strong diffraction or defocus contrast. Several methods can be used to remove the MIP term [17], as also described in the following.

One approach involves recording a second hologram after inverting the specimen to change the sign of the magnetic induction, and then using the sum and difference of the two phase images to separate the magnetic and MIP contributions, respectively. Another alternative is to acquire two holograms at different electron energies, which only affects the MIP contribution, and thus the MIP can be calculated. However, in many practical situations, it is neither feasible to turn the specimen over, nor convenient to change the accelerating voltage during an experiment. Additional steps are then required during *in situ* experiments to fully reverse the magnetization within the specimen by tilting the holder in a residual vertical field provided by the objective lens. With pairs of phase images reconstructed from states that differ only in the opposite directions of magnetization, the magnetic and MIP contributions can be calculated by taking half of the difference, and half of the sum, respectively. This procedure ensures that dynamical contributions for small, strongly diffracting crystals are removed and justifies the use of Equation (2.7) to interpret the results. It is also important to note that this method may fail in some cases when the magnetization within the sample does not reach exactly opposite states, meaning that inversion of the sample will be necessary.

Electron holography is usually carried out through a two-step process. First, a hologram is obtained by superimposing a reference wave on an object wave which contains both amplitude and phase information about the sample. In the second step, the phase shift needs to be extracted from the hologram. This is done using the Fourier transform method. Figure 2.8 illustrates a typical holographic phase reconstruction process, using a magnetic spin-valve nanoring sample as an example [18]. A hologram of the magnetic nanoring was obtained in the region of interference fringes [Figure 2.8 (a)], with the enlargement [Figure 2.8 (b)] showing bending of the interference fringes at the edge of the nanoring. Fast Fourier transform (FFT) was carried out using the desired region of the hologram, to produce a central autocorrelation peak and two sidebands in reciprocal space, as indicated in Figure 2.8 (c). The central autocorrelation peak contains the modulus-squared of the wave function and thus cannot be used to extract any phase information. The two sidebands contain identical information apart from a change in sign of the phase. One of the two sidebands can be selected to obtain the desired phase information. The complex image [Figure 2.8 (d)] is reconstructed by obtaining an inverse Fourier transform (IFT) of the extracted side-band. The phase information can be retrieved from the reconstructed complex image by taking the arctangent of the imaginary part over the real part, followed by unwrapping the phase discontinuities that result from the fact that it is initially calculated modulo 2π . The reconstructed phase images can be expressed in the pseudo-contour mode, as shown in Figure 2.8 (e), where different colors represent equal phase values. As illustrated by the color coding, each constant phase increase of 2π corresponds to the color sequence of black-blue-green-red-yellow-white. This color scheme is useful for determining the direction of the phase shifts, which are always of concern for magnetic materials.

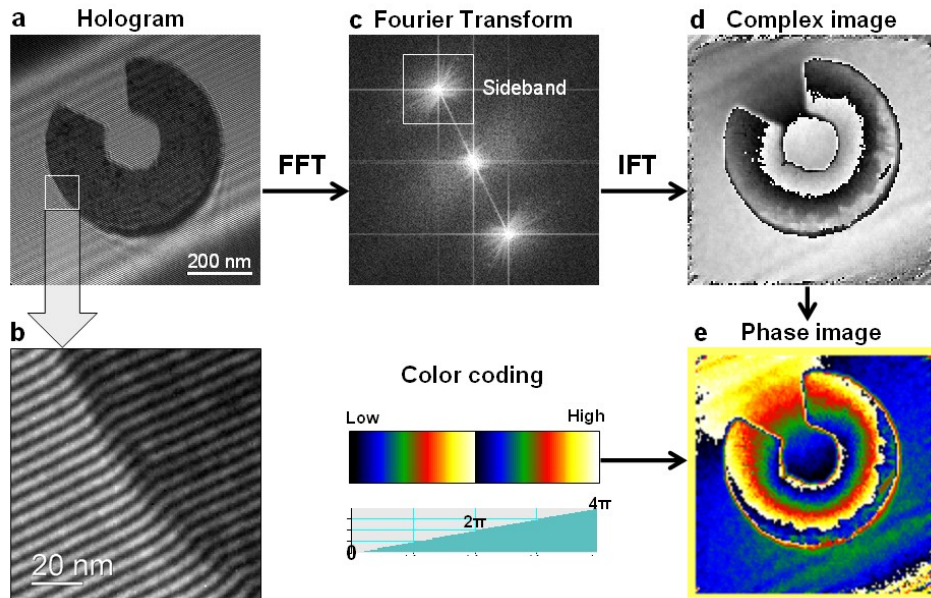


Figure 2.8. Image reconstruction process for extracting phase shifts from hologram.

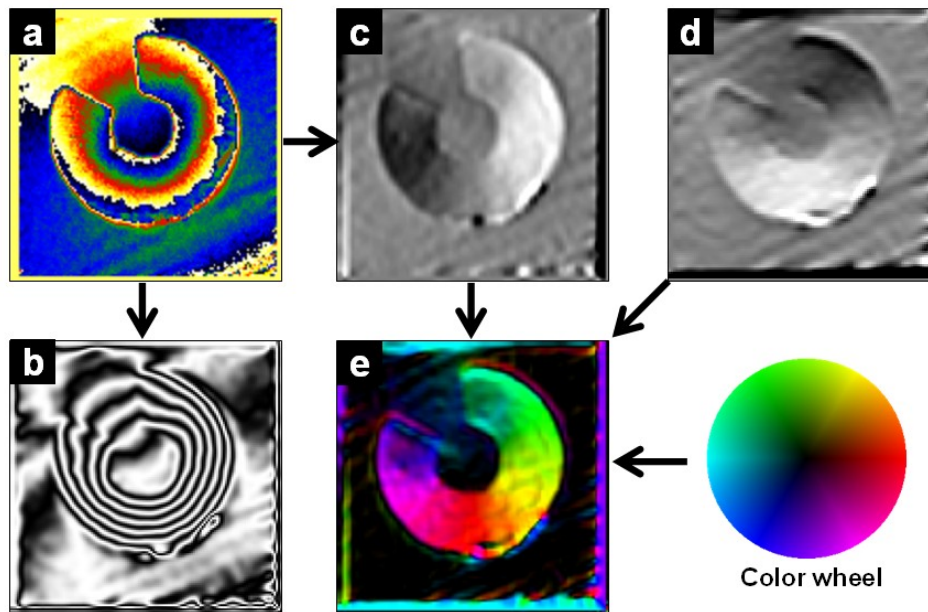


Figure 2.9. Different representation schemes for phase shifts related to magnetic field. (a) Pseudo-color phase image; (b) $8\times$ amplified phase contours; (c) x- and (d) y-gradient of phase in (a); (e) magnetic induction map using color wheel as direction reference.

For convenience, in order to clarify information about the magnetic field, including amplitude and direction, several different schemes are used for magnetic imaging representation, including pseudo-color phase image, amplified black-white phase contours, and colored magnetic induction map, as shown in Figures 2.9 (a), (b), and (e), respectively.

For pseudo-color phase images, colors represent the amplitudes of the phase, while the sequence of colors indicates the direction of phase increase (or decrease) for determining the magnetization directions based on the right-hand rule. In this particular example, the phase increases from the inner edge to the outer edge of the ring, indicating that the magnetization is in a counterclockwise (CCW) rotation. The phase image can be represented in grey-scale phase contours by applying a cosine function and then amplifying the phase, so that the contours indicate the magnetization distribution and the black-white separation quantifies the amplitude. Although this does not show the magnetization direction, this straightforward method has been widely used and accepted by researchers in this field. Another representation, the so-called magnetic induction map, has also been developed to indicate magnetization directions based on a red-green-blue (RGB) color wheel scheme. Magnetization components along x and y directions can be obtained by taking derivatives with respect to the corresponding normal orientations, as shown in Figure 2.9 (c) and (d). The vector field is then reconstructed by combining the two orthogonal gradients, and encoding with specific RGB colors. This color scheme is also widely accepted in the magnetics community, but one drawback is the lack of amplitude information. Nevertheless, one can take advantage of these last two representation schemes by coloring the amplified phase contours using the RGB color wheel. These different schemes are equivalent, and they have all been used in this dissertation depending on the specific purpose of a particular situation.

In practice, the electron holography observations of nanomagnets in this dissertation research have been performed in the Lorentz mode using the Philips-FEI CM200-FEG TEM. An *in situ* magnetic field can be applied to the specimen by partially turning on the current of the objective lens, and the desired component of the applied field in the specimen plane is obtained by tilting the sample holder, as shown in Figure 2.10 (a). The magnetization of the sample can be saturated by tilting the holder by $\pm 30^\circ$, with the in-plane component suitably chosen to exceed the coercive field of the magnetic layer(s) of interest. The remanent states can then be reached by tilting back to the horizontal position. To determine a complete hysteresis loop, a series of observations should be carried out by tilting from $+30^\circ$ to -30° and back to $+30^\circ$. At each tilt position, the overall magnetization of the entire element is calculated by taking the integral of the local magnetization along the in-plane applied field direction using dedicated scripts written in Gatan Digital Micrograph™. Before calculation, the applied field direction (tilting direction) for the phase images should be aligned to be horizontal and all of the images need to be adjusted to the original aspect ratio to ensure that foreshortening or stretching caused by tilting have no influence on the subsequent processing. The gradients of the phase shifts perpendicular to the applied field direction are then calculated for each pixel. The slopes are averaged over the whole element for each tilt with the background and element edges masked out, where the values for the $\pm 30^\circ$ tilts corresponding to full saturation are defined as unity for the M/M_s plot. These values are then used to normalize the others obtained at different tilts. Thus, the entire hysteresis loop for in-plane magnetization reversal can be quantitatively determined.

The magnitude of applied magnetic field is based on the prior calibration of the field as a function of objective lens current, as shown in Figure 2.10 (b). The field is parallel to the incident beam direction and is not sensitive to changes in specimen height.

The default value for objective lens current in normal operating mode is ~ 9880 mA, corresponding to a vertical magnetic field of ~ 1.90 T (19000 Oe). The residual field at the specimen plane is unaffected by excitation of the Lorentz minilens, and negligible in most cases.

Several important parameters need to be considered for holographic imaging, including fringe spacing, fringe overlap, fringe visibility (contrast), and field of view [12]. These parameters can be controlled by suitable combinations of accelerating voltage, extraction voltage, and biprism voltage. To ensure coherent illumination, the microscope is usually operated at 200 kV with gun lens 5 and spot size 1 setup. The fringe visibility is quite sensitive to the extraction voltage, with the optimum value of ~ 3.78 kV. The biprism voltage determines both the fringe spacing and the region of

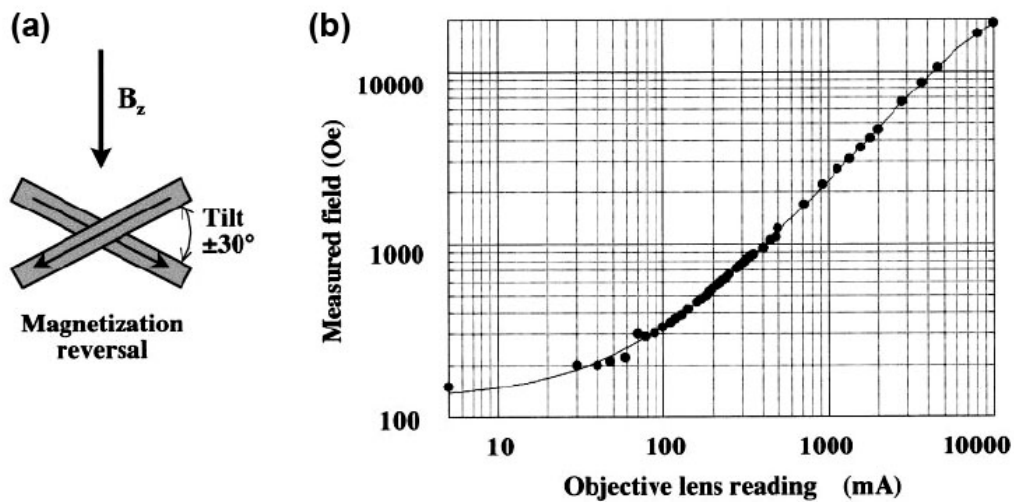


Figure 2.10. (a) Schematic diagram showing the use of specimen tilt to provide the in-plane component of the applied field needed for *in situ* magnetization reversal experiments. (b) Hall probe measurements of magnetic field in specimen plane of Philips CM200 as function of objective lens current [2].

overlap, and is typically biased to a potential of 100 V. The holographic fringe contrast is defined by

$$\mu = \frac{I_{\max} - I_{\min}}{I_{\max} + I_{\min}} \quad (2.8)$$

where I_{\max} and I_{\min} are maximum and minimum intensity, respectively, in the region of overlap of the interference fringes. The contrast can be measured by an averaged line profile across the fringes, and typical fringe contrast of ~40% can be obtained, which is more than adequate for holographic imaging and phase reconstruction.

2.5. Examples of Quantitative Phase Imaging

2.5.1. Kagome lattices

The term “spin ice” refers to a magnetic system with geometrical frustrated interactions, where the local disorder of magnetic moments appears in the ordered lattice structure [19]. Recent experiments have provided evidence suggesting the existence of deconfined magnetic monopoles in these materials, with properties analogous to the hypothetical magnetic monopoles postulated to exist in vacuum [20–26].

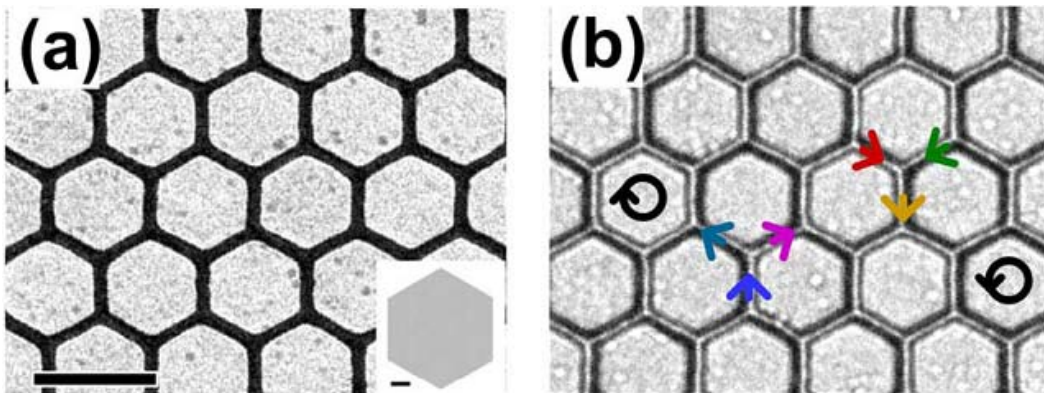


Figure 2.11. (a) In-focus, and (b) defocused, Lorentz TEM image of kagome structure. Fresnel contrast indicates clockwise and counterclockwise closed loops. [27].

Cumings and his group at the University of Maryland have recently described realization of an artificial spin ice system using a two-dimensional (2D) kagome lattice [27]. Lorentz imaging was used to demonstrate the local ice rule and as well as the occurrence of long-range dipolar interactions, as illustrated by Figure 2.11. However, many details remain to be determined about this topic. As a collaborative project, electron holography was used to characterize some typical spin-ice samples. These results also represent an example of quantitative phase imaging.

The kagome-structured spin ice samples were fabricated using conventional EBL technique, followed by metal deposition of Py ($\text{Ni}_{80}\text{Fe}_{20}$) and lift-off [27]. The designed patterns included hexagonal honeycombs with different lengths and widths, and separated three-fold “Y” shaped junctions. The Py layer is nominally 23 nm in thickness.

The kagome lattice having $\sim 1\mu\text{m}$ diagonal separation and $\sim 110\text{nm}$ lattice width was first observed, as shown in Figure 2.12. Because of the limited region of coherent illumination for electron holography, only the edges of the kagome lattice could be observed, but some irregular branch shapes were present in such regions due to errors during fabrication. The initial saturation magnetic field was applied from the top-right to the bottom-left direction, and then reverse saturated along the opposite direction. Holograms in the two opposite remanent states were thus obtained. The corresponding reconstructed phase images are shown in Figure 2.12 (a) and (b). Line profiles from the same regions but in opposite magnetic states are shown plotted, and the linear slopes caused by the magnetic fields only appear at the central part of the wire. However, these are smeared out at the wire edges due to the nonuniform thickness (or MIP) contribution. A phase image showing the pure magnetic component could be achieved by the subtraction of images, as shown in Figure 2.12 (c). Line profiles indicate a linear slope across the entire wire, but the slope remains flat elsewhere, suggesting that constant

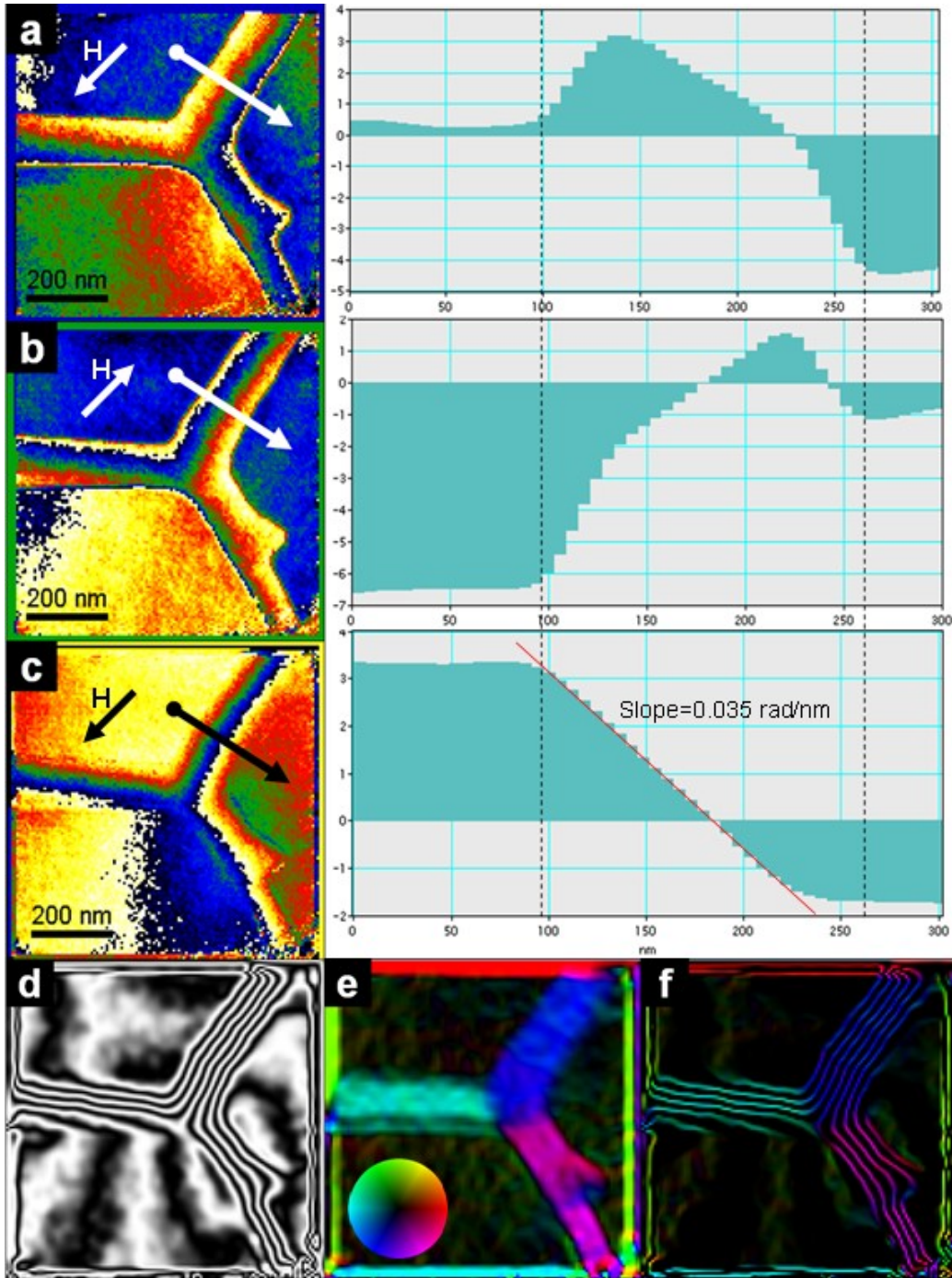


Figure 2.12. Phase images of kagome lattice composed of Py and corresponding line profiles in remanent state with: (a) saturation field pointing to bottom-left; (b) saturation field pointing to top-right; and (c) pure magnetic contribution. (d) $8\times$ amplified phase contours, (e) magnetic induction map, and (f) magnetic contour map, converted from (c).

magnetization is uniformly distributed within the wire, and that any edge effects have been completely removed. Measurements showed that the slope of the phase shifts in all three wires was 0.035 ± 0.001 rad/nm. Since the thickness of the lattice is nominally 23 nm, the corresponding magnetic induction is calculated to be 1.00 ± 0.03 T, which is a reasonable value for the saturation magnetization of Py. The phase image was converted into phase contours, magnetic induction map, and magnetic contour map, as shown in Figure 2.12 (d)–(f), respectively. These clearly indicate the directions of magnetization and the surrounding fringing fields.

At this junction of the kagome lattice, the magnetic flux comes “in” from the top-right, and then goes “out” through the left and bottom-right, thus forming an “in-out-out” configuration. The 2D mapping of the magnetic phase contours within lattice wires and the external fringing fields confirmed that the magnetization contours were continuous, and in closure loops, indicating that no magnetic monopoles were present in this area.

Similar characterization was carried out on another kagome lattice with smaller dimensions of ~ 500 nm across the diagonal and ~ 65 nm in lattice width. The corresponding phase images and magnetic induction maps are shown in Figure 2.13. The magnetic induction map in Figure 2.13 (b) clearly shows four junctions with different configurations, where one “in-out-out” configuration (I) is associated with three “in-in-out” configurations (II, III, and IV). However, only magnetic flux closures, but no evidence for monopoles, were found in the kagome lattice.

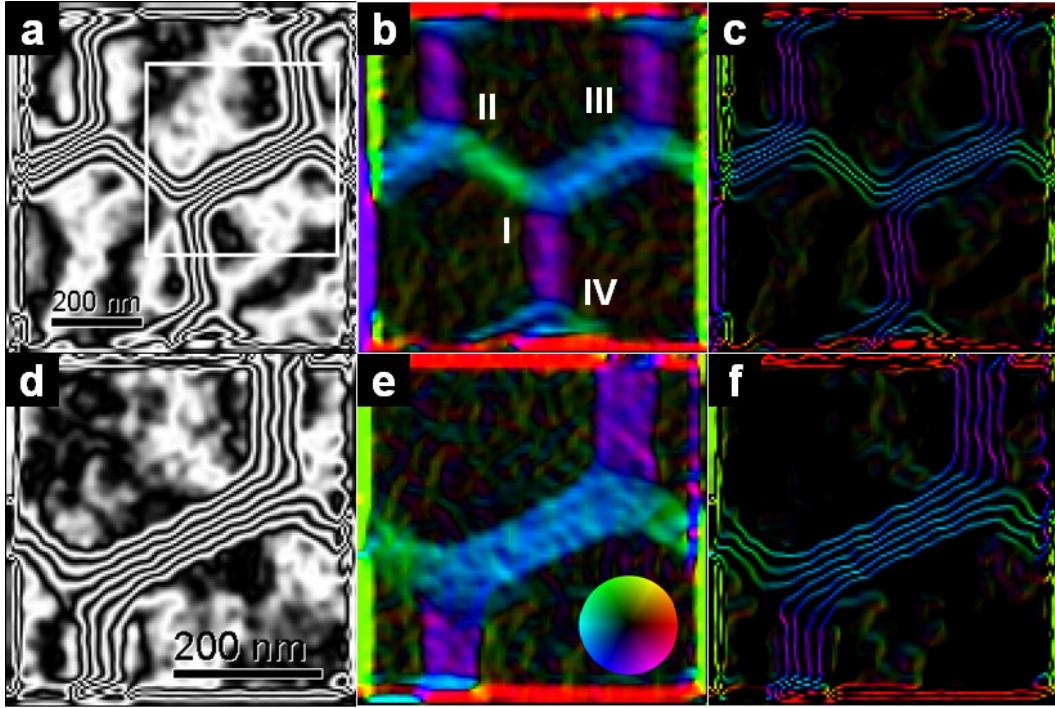


Figure 2.13. Phase contour map (12 \times amplified), magnetic induction map, and magnetic contour map of (a)–(c) 500-nm-diagonal kagome lattice, and (d)–(f) enlarged box area, respectively. Magnetization directions indicated by color wheel.

Individual Y-junctions with a 3-fold symmetry shape were observed in order to investigate any differences in properties between separated junctions and junctions in a continuous lattice. Figure 2.14 (a) shows the Lorentz image of as-fabricated Y junctions. Each branch of the Y-junction is 100 nm in width and 400 nm in length. Contaminations from EBL and lift-off processes, such as metal particles and residual chemicals, were visible on the nitride membrane. These could cause considerable noise in both imaging and reconstruction of the phase shifts. The boxed area was placed in the region of coherent illumination and a hologram was obtained, as shown in Figure 2.14 (b). The reconstructed phase contour map, magnetic induction map, and magnetic contour map are shown in Figures 2.14 (c)–(e), respectively. Noise signals caused by the contamination,

appearing as big dots or vortices in the phase contour map, did not obscure the result that the individual Y-junction was in an “in-in-out” configuration, with continuous magnetic flux.

Although no obvious evidence was found in these studies to confirm the existence of magnetic monopoles, this investigation of kagome lattices demonstrated the capability of electron holography for observing and quantifying static magnetic fields on the nanometer scale.

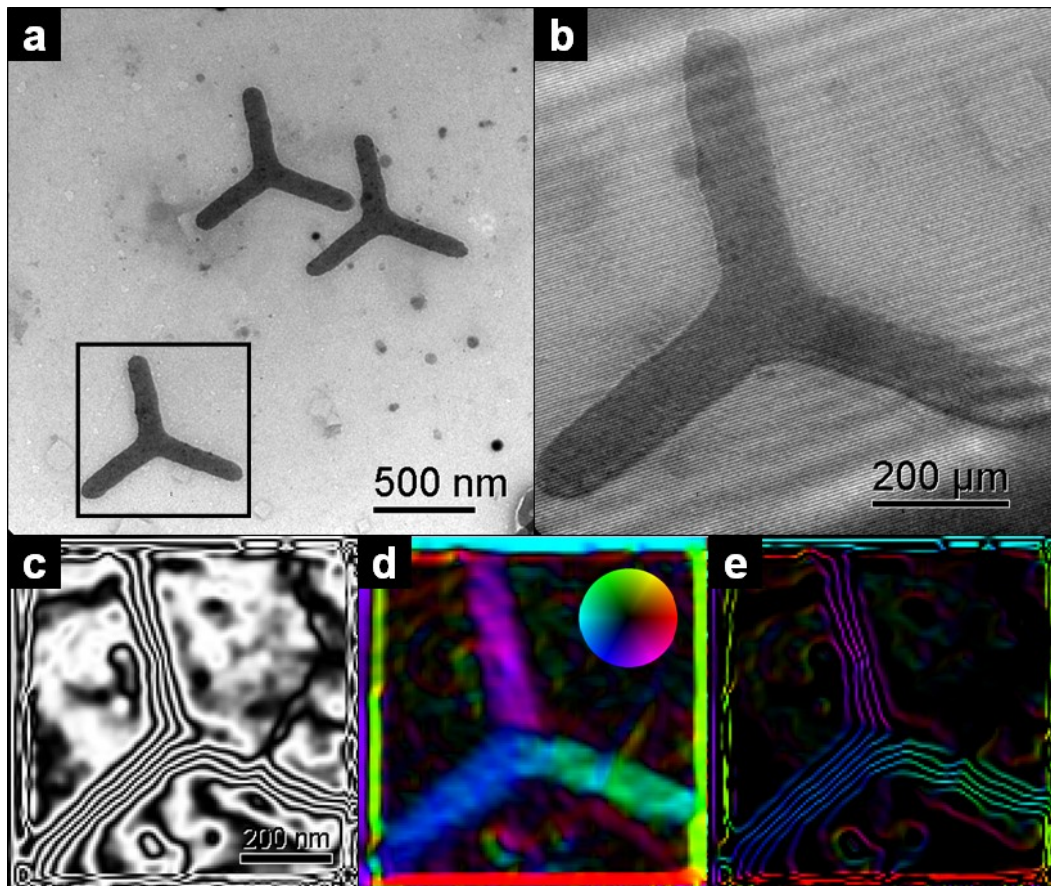


Figure 2.14. (a) Lorentz TEM image of as-fabricated Y-junctions. (b) Hologram of an individual Y-junction in boxed area of (a). (c) Phase contour map (12× amplified), (d) magnetic induction map, and (e) magnetic contour map, respectively, of the Y-junction.

2.5.2. Ferromagnetic triangles

The dynamic properties of ferromagnetic magnets with different shapes have been a topic of considerable interest with the emergence of new technological applications of patterned magnetic recording media. Uniform magnetization is desirable but oftentimes unachievable in polygonal particles due to shape anisotropy and high-order configurational anisotropy [28]. For example, micromagnetic simulations for nanoscale ferromagnets of triangular shape suggested two equilibrium states at remanence. One was the so-called “Y” state, where the magnetization fanned in from two corners towards the third along the bisector; the other was referred as the “buckle” state, where the magnetization bent toward one of the corners parallel to the edge, as indicated schematically in Figure 2.15 [29]. Particular attention has been given to these triangle magnets as a function of different shapes and external fields, in particular to find the magnetization reversal mechanism(s) and any related spin-wave confinement caused by internal fields [28–31]. Representative triangle-shaped magnets have been investigated in collaboration with Shaw (NIST) and Hillebrands (University of Kaiserslautern).

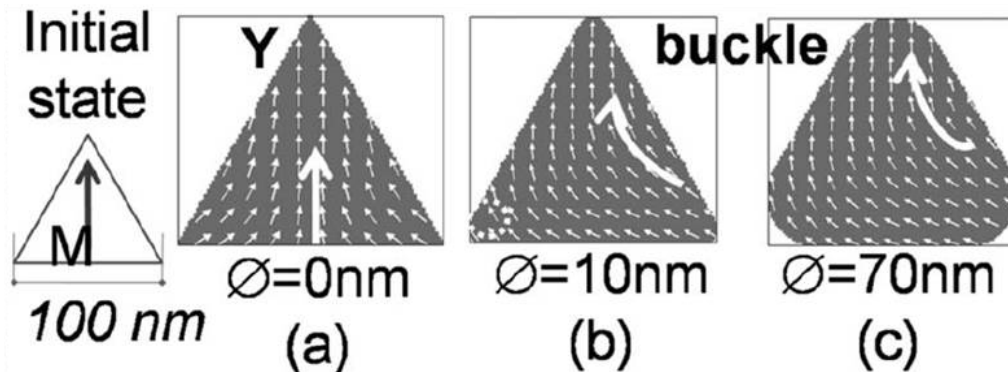


Figure 2.15. Micromagnetic simulations showing remanent configuration in: (a) Y state in a sharp triangle; and (b), (c) buckle states in rounded triangles [29].

The Py triangles were fabricated using standard EBL and etching methods. The patterned elements were all of the same thickness of 10 nm, but with different lateral dimensions, nominally, 1×1.5 , 1×1 , 0.5×1.5 , 0.5×1 (base \times height, unit in μm), as shown by the Lorentz TEM images in Figures 2.16 (a)–(d), respectively.

Each of the magnetization states of these elements during an entire hysteretic switching process was recorded at a series of tilting positions with respect to the vertical applied magnetic field. Figure 2.16 shows seven different states (1–7) for each triangle (a–d) as a function of applied field strength. The two proposed states were identified, with the buckle states visible at the remanence (a4, b4, c4, d4), whereas the Y states occurred at the saturation fields (a7, b7, c7, d7). These results are in good agreement with recent experimental and simulated results [29–31], although the proposed vortex mode was not observed. Moreover, it was found that the critical fields for the transitions between the two states varied depending on the different height-base ratios, which most likely correlates with the shape and configurational anisotropy. Comprehensive investigation for a better understanding is ongoing, but it can be concluded that electron holography has been demonstrated to provide useful insights for both static and dynamic aspects of nanoscale magnetic materials.

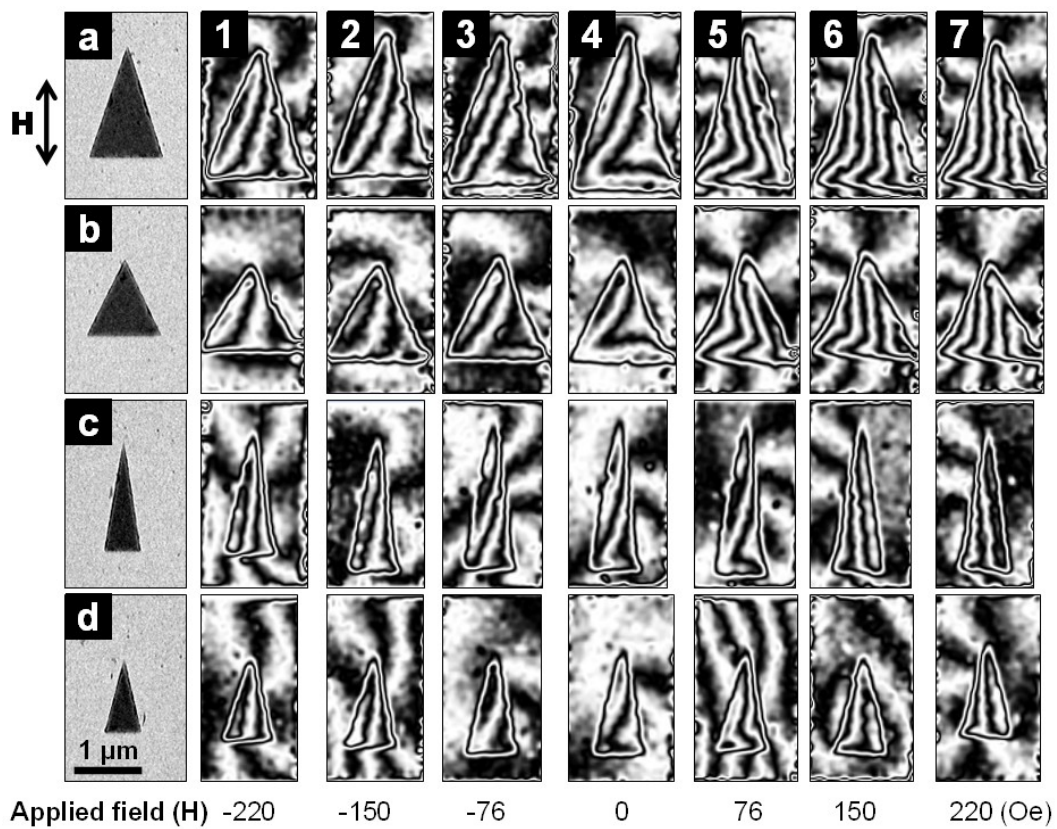


Figure 2.16. Lorentz images of Py triangles with different sizes, and corresponding phase contours (4× amplified) as function of in-plane applied field. Applied field along the long axis of the triangles.

References

- [1] M. A. McCord and M. J. Rooks, in *Handbook of Microlithography, Micromachining, and Microfabrication Volume 1*, edited by P. Rai-Choudhury, SPIE Optical Engineering Press, Bellingham, WA, Chapter 2, (1997).
- [2] R. E. Dunin-Borkowski, M. R. McCartney, B. Kardynal, M. R. Scheinfein, and D. J. Smith, *J. Microsc.* 200, 187 (2000).
- [3] T. Schrefl, D. Suess, G. Hrkac, M. Kirschner, O. Ertl, R. Dittrich, and J. Fidler, in *Advanced Magnetic Nanostructures*, edited by D. J. Sellmyer and R. Skomski, Springer, New York, Chapter 4, (2006).
- [4] T. L. Gilbert, *Phys. Rev.* 100, 1243 (1955).
- [5] L. D. Landau and E. M. Lifshitz, *Phys. Z. Sowietunion* 8, 153 (1935).
- [6] M. J. Donahue and D. G. Porter, *OOMMF User's Guide Version 1.0*, National Institute of Standards and Technology, Gaithersburg, MD (1999).
- [7] J. N. Chapman, *J. Appl. Phys.: D* 17, 623 (1984).
- [8] J. N. Chapman and A. K. Petford-Long, in *Magnetic Microscopy of Nanostructures*, edited by H. Hopster and H. P. Open, Springer-Verlag, Berlin-Heidelberg, Chapter 4, (2005).
- [9] D. Shindo and T. Oikawa, *Analytical Electron Microscopy for Materials Science*, Springer-Verlag, Tokyo, Chapter 5, (2002).
- [10] D. Gabor, *Nature* 161, 777 (1948).
- [11] D. Gabor, *Proc. Roy. Soc. London A*197, 454 (1949).
- [12] D. J. Smith and M. R. McCartney, in *Introduction to Electron Holography*, edited by E. Völkl, L. F. Allard and D. C. Joy, Kluwer Academic-Plenum Publishers, New York, Chapter 4, (1999).
- [13] R. E. Dunin-Borkowski, M. R. McCartney, and D. J. Smith, in *Encyclopedia of Nanoscience and Nanotechnology*, edited by H. S. Nalwa, American Scientific Stevenson Ranch, CA, Chapter 7, (2004).
- [14] M. R. McCartney and D. J. Smith, *Annu. Rev. Mater. Res.* 37, 729 (2007).
- [15] H. Lichte, P. Formanek, A. Lenk, M. Linck, C. Matzeck, M. Lehmann, and P. Simon, *Annu. Rev. Mater. Res.* 37, 539 (2007)
- [16] A. Tonomura, *Surf. Sci. Rep.* 20, 317 (1994).
- [17] R. E. Dunin-Borkowski, T. Kasama, A. Wei, S. L. Tripp, M. J. Hÿtch, E. Snoeck, R. J. Harrison, and A. Putnis, *Microsc. Res. Tech.* 64, 390 (2004).

- [18] M.R. McCartney, N. Agarwal, S. Chung, D.A. Cullen, M.-G. Han, K. He, L. Li, H. Wang, L. Zhou, D.J. Smith, *Ultramicroscopy* 110, 375 (2010).
- [19] L. Pauling, *J. Am. Chem. Soc.* 57, 2680 (1935).
- [20] R. F. Wang, C. Nisoli, R. S. Freitas, J. Li, W. McConville, B. J. Cooley, M. S. Lund, N. Samarth, C. Leighton, V. H. Crespi, and P. Schiffer, *Nature* 439, 303 (2006).
- [21] C. Castelnovo, R. Moessner, and S. L. Sondhi, *Nature* 451, 42 (2008).
- [22] O. Tchernyshyov, *Nature* 451, 22 (2008).
- [23] L. D. C. Jaubert and P. C.W. Holdsworth, *Nature Phys.* 5, 258 (2009).
- [24] M. J. P. Gingras, *Science*, 326, 375 (2009).
- [25] D. J. P. Morris, D. A. Tennant, S. A. Grigera, B. Klemke, C. Castelnovo, R. Moessner, C. Czternasty, M. Meissner, K. C. Rule, J.-U. Hoffmann, K. Kiefer, S. Gerischer, D. Slobinsky, and R. S. Perry, *Science* 326, 411 (2009).
- [26] T. Fennell, P. P. Deen, A. R. Wildes, K. Schmalzl, D. Prabhakaran, A. T. Boothroyd, R. J. Aldus, D. F. McMorrow, and S. T. Bramwell, *Science* 326, 415 (2009).
- [27] Y. Qi, T. Brintlinger, and J. Cumings, *Phys. Rev. B* 77, 094418 (2008).
- [28] D. K. Koltsov, R. P. Cowburn, and M. E. Welland, *J. Appl. Phys.* 88, 5315 (2000).
- [29] L. Thevenard, H. T. Zeng, D. Petit, and R. P. Cowburn, *J. Appl. Phys.* 106, 063902 (2009).
- [30] M. Jaafar, R. Yanes, A. Asenjo, O. Chubykalo-Fesenko, M. Vázquez, E. M. González, and J. L. Vicent, *Nanotechnology* 19, 285717 (2008).
- [31] F. Montoncello and F. Nizzoli, *J. Appl. Phys.* 107, 023906 (2010).

CHAPTER 3
MAGNETIZATION CONFIGURATIONS AND VORTEX-CONTROLLED
SWITCHING BEHAVIOR OF Co NANORINGS

This chapter describes the electron holography investigation of remanent states and magnetization reversal of monolayer Co nanorings, with and without slots. Vortex-controlled switching behavior has been identified, which exhibits stepped hysteresis loops with specific well-defined states including onion states, vortex states, flux-closure states, and omega states. Two distinct switching mechanisms, depending on the applied field direction relative to the slot orientation, can be attributed to the vortex chirality and shape anisotropy. Micromagnetic simulations have also been performed to confirm the experimental observations. The major results of this study have been published elsewhere [1, 2].

3.1. Introduction

Nanopatterned ferromagnetic (FM) elements have been intensively studied during the past decade due to their potential applications in high density data storage technology [3]. A reproducible magnetization reversal process with well-defined remanent states and narrow switching fields is obviously preferable for recording purposes. As the lateral dimensions of the elements are scaled down to the hundreds to tens of nanometers, their geometry plays an even more important role in determining the magnetization configuration [4]. Designs based on simple shapes, such as squares, rectangles, and other polygons, are not really suitable for data storage due to the occurrence of irregular edge domains [4–7]. Circular disks can lead to stable magnetization configurations, i.e., flux-closure (FC) states (often referred to as vortices),

without any stray field, which thus minimizes any interaction between elements. However, the presence of the central vortex limits their functionality by complicating the switching process [8, 9].

Ring-shaped nanostructures are attracting interest because their circular geometry can support FC states, as well as eliminating the high-energy central vortex core that causes irreproducibility during magnetization reversal [10–12]. Another common state obtained in ring structures after saturation is the so-called “onion” or “bi-domain” state, consisting of two semicircular head-to-head (HTH) domains separated by domain walls (DWs) [13]. The switching process then occurs out via two different modes, namely, coherent onion rotation or onion-FC-onion transition [14–16]. Several approaches have been used to obtain controllable switching mechanisms via the introduction of asymmetrical characteristics to the ring, including displacement of the central hole or cutting out a slot [16–20]. In either of these geometries, the asymmetrical shape leads predominantly to the onion-FC-onion transition via the formation and annihilation of DWs. Local spin-vortex structures often appear during the magnetization reversal, resulting in irregularities in the switching process and broadening of the switching field distribution. Thus, better understanding and more precise control of the dynamics of magnetic vortex structures are essential in order to improve the functionality of magnetic nanostructures [13, 21–22]. Based on micromagnetic simulations, a vortex-dependent magnetization process with a three-step hysteresis loop was proposed, which suggested that spin-vortex structures had caused the transform from onion state to FC state [15]. However, no direct experimental evidence for this three-step reversal mechanism has been previously reported.

In this chapter, Co nanomagnets with ring shapes were chosen for investigation, where the slots were intended to introduce geometrical restrictions that would change the

shape anisotropy and constrain any vortex excitations relative to regular rings. The sample geometries are shown schematically in Figure 3.1. The 30-nm-thick Co elements were fabricated directly onto silicon nitride TEM membrane windows using EBL and lift-off process, followed by deposition of another 3-nm-thick Ti layer in order to minimize oxidation and to prevent electrostatic charging during TEM observation. *In situ* magnetic fields with maximum in-plane components of ~ 1200 Oe at $\pm 30^\circ$ tilting positions were applied parallel or perpendicular to the slot direction, and electron holography observations to examine the remanent states and magnetization reversal were carried out using the Lorentz TEM mode.

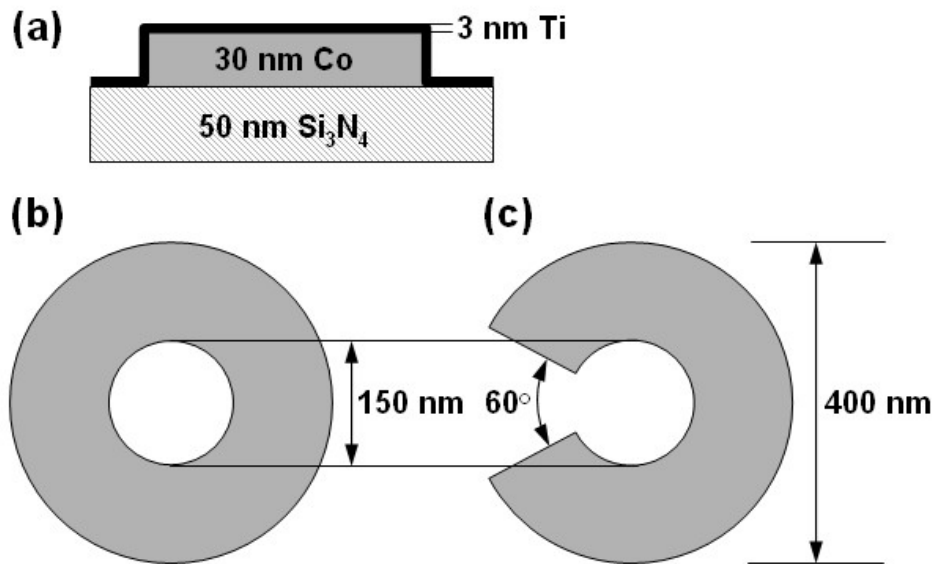


Figure 3.1. Schematics showing the geometry of Co nanoring and slotted Co nanoring, grown on thin silicon nitride TEM membranes: (a) Side view; and plan view of (b) nanoring; and (c) slotted nanoring.

3.2. Remanent States and Switching Behavior of Co Nanorings

The as-prepared Co nanorings were observed with and without applied magnetic field. Figure 3.2 (a) is a Lorentz image showing the nanorings with outer diameter of ~ 400 nm and inner diameter of ~ 150 nm. These nanorings were patterned into 3×3 arrays, with ~ 800 -nm spacing between adjacent elements to minimize any interactions. The reconstructed phase image of a Co nanoring observed at remanence is shown in Figure 3.2 (b). Phase shifts due to the magnetic contributions were extracted using a pair of holograms having opposite FC chirality, as shown in the contour map. The uniformly

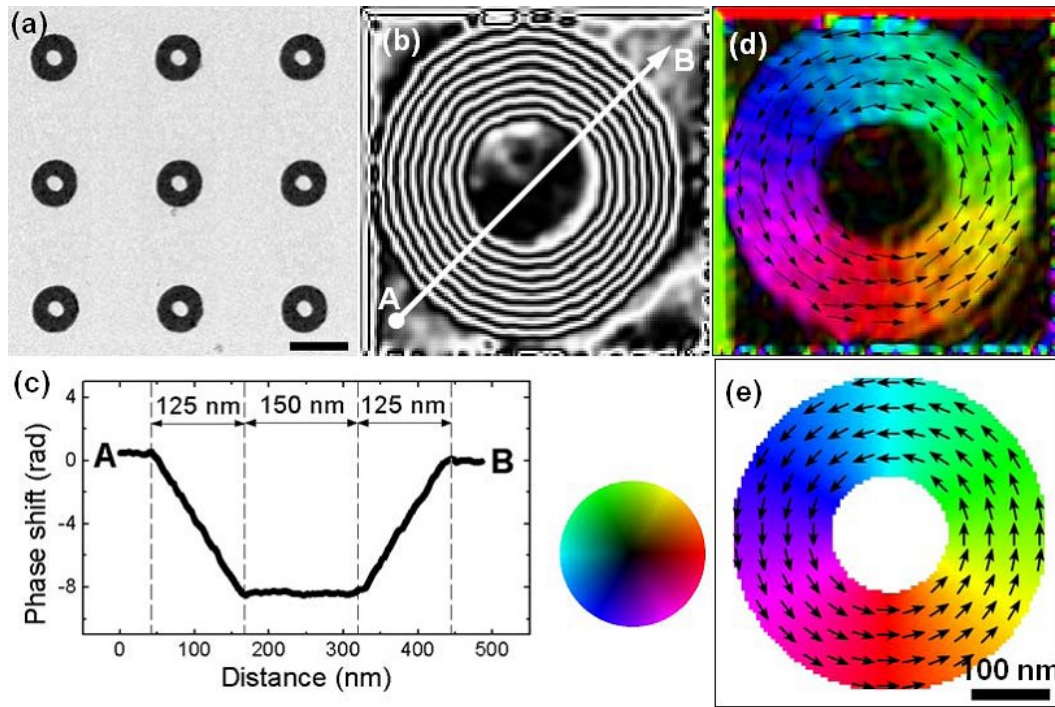


Figure 3.2. (a) Lorentz TEM image showing Co nanoring array (Scale bar indicates 500 nm). (b) Reconstructed holographic phase image of an individual nanoring showing FC state at remanence, with phase contour spacing of $\pi/3$. (c) Line profile from A to B. (d) Experimental, and (e) simulated, magnetic induction maps of the Co nanoring. Magnetization directions indicated by color wheel and overlaid arrows.

distributed contours demonstrate the FC magnetization rotation of the nanoring. The line profile, taken from position A to B, shows the linearity of the phase shifts within the nanoring and almost constant phase in external areas. The effective magnetic thickness was determined to be ~ 25 nm using phase gradient measurements and Equation 2.7. This thickness value was less than the nominal amount, but it was then used in the subsequent micromagnetic simulations. The phase image was converted into a magnetic induction map, using a color wheel for denoting particular directions, as shown in Figure 3.2 (d). The remanent induction map for the same structure, was calculated by OOMMF simulations, as shown in Figure 3.2 (e), and is in close agreement with the experimental observation.

The switching behavior of the Co nanorings when taken through a complete hysteresis cycle was then investigated in detail. Figure 3.3 shows the hysteresis loop for an individual Co nanoring. This hysteresis loop was extracted from the experimental holographic phase images, using images obtained at saturation for normalization to unity. The details of these calculations were described earlier in section §2.4.2. The hysteresis loop exhibited two steps, corresponding to transitions from the saturated onion state to the FC state, and then to the reversed onion state. A double vortex appeared during the onion-to-FC transition when the external field approached close to zero, but this did not appear to affect the shape of the hysteresis loop, nor did it cause any obvious plateau. The slight horizontal shift in the loop was attributed to a small zero error in sample tilting, however, this did not affect determination of the switching field which was found to be ~ 800 Oe.

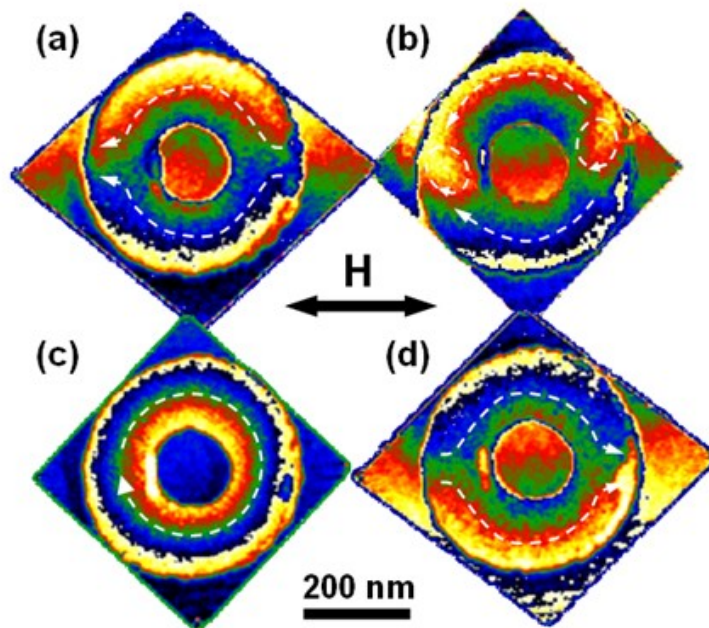
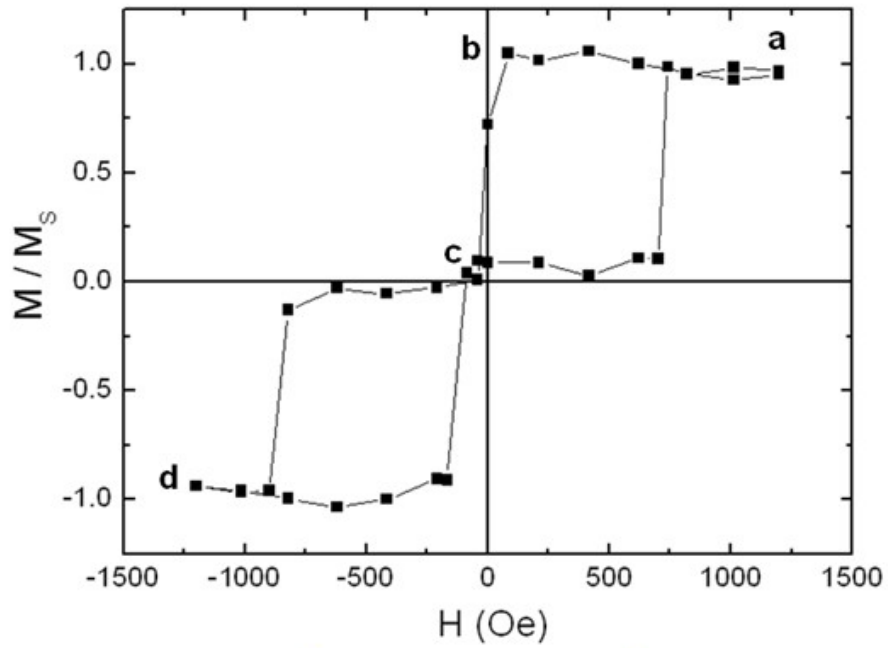


Figure 3.3. Hysteresis loop of an individual Co nanoring where a–d correspond to specific states visible in phase images: (a) onion state at saturation; (b) excitation of double-vortex; (c) FC state; (d) onion state at reverse saturation. Magnetization directions indicated by overlaid white arrows. Applied field directions indicated by the black arrow.

Figures 3.3 (a)–(d) show representative phase images corresponding to the magnetization states observed at different stages of the hysteresis loop, which are labeled with a–d. These configurations were obtained from one half of the hysteresis loop, and are opposite to those observed in the other half of the loop. The saturation configurations with strong fringing fields corresponded to the onion state and the reversed onion state, as shown in Figures 3.3 (a) and (d), respectively. By taking the color sequences into account, the directions of magnetization can be determined, as indicated by the overlaid arrows. Two vortices, both with clockwise (CW) chirality, were identified close to the domain wall (DW) region of the onion configuration, as visible in Figure 3.3 (b). The chirality of the vortex directly affects the evolution of the vortex and determines the switching mechanism, as will be discussed in detail later. The double-vortex state was formed as the external field approached the remanence condition, and it was then eliminated leaving behind a flux-closure state with CW magnetization and minimal fringing field, as shown in Figure 3.3 (c). The upper half of the element reversed first to form the FC, followed by switching of the lower half to obtain the completely reversed onion state. The presence of the FC configuration was visible as a flat plateau, and stabilized the Co nanorings.

3.3. Remanent States and Switching Behavior of Slotted Co Nanorings

As-prepared Co slotted nanorings were observed with and without applied magnetic field. Figures 3.4 (a) and (b) show Lorentz images of two sets of element arrays with the slot orientations rotated by 90° . The in-plane magnetic field was applied along the directions indicated by arrows, i.e., parallel to the slot direction in Figure 3.4 (a), and perpendicular to the slot direction in Figure 3.4 (b). For convenience, the designations SR1 and SR2 will be used to denote slotted rings with slot directions parallel, or

perpendicular, to the applied field direction, respectively. Typical elements in both arrays were observed at the remanent state after initial saturation and removal of the applied field, and the corresponding reconstructed phase images are shown in Figures 3.4 (c) and (d). Observations showed that the remanent magnetization configurations exhibited onion states when the initial saturation field was applied parallel to the slot orientation, whereas FC states were preferentially obtained with the initial saturation direction perpendicular to the slot direction.

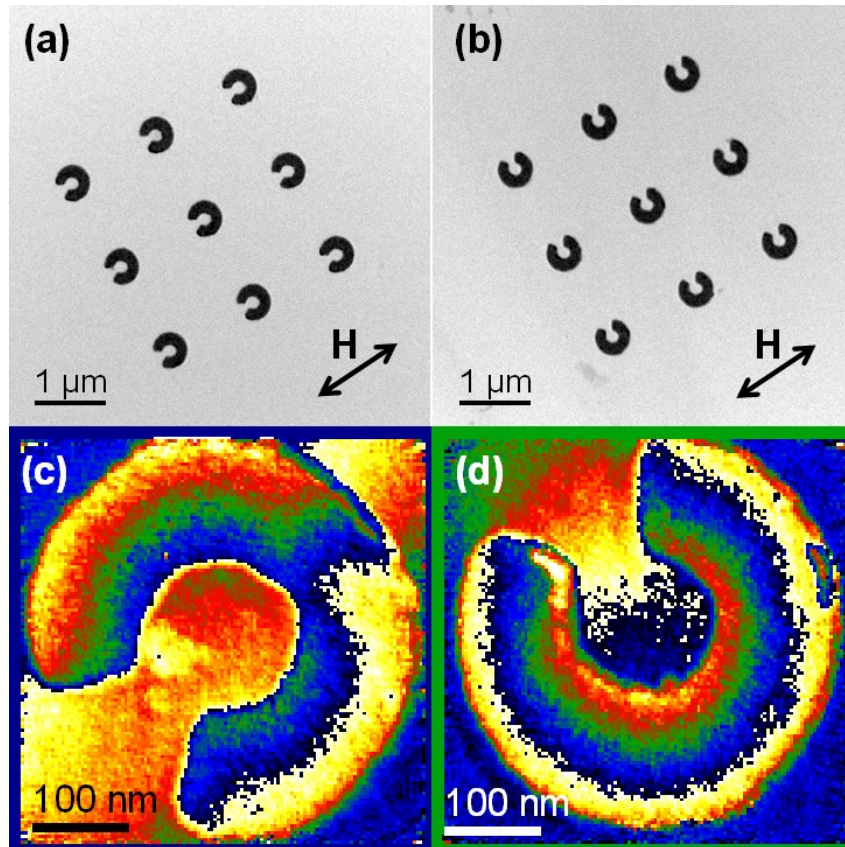


Figure 3.4. Lorentz images of Co slotted nanorings, with slot directions (a) parallel, and (b) perpendicular, to applied field directions (indicated by double arrow). Reconstructed phase images showing individual Co elements at remanence: (c) onion; and (d) FC state.

The switching behavior of the Co slotted nanorings through a complete hysteresis cycle was also observed. Figure 3.5 compares hysteresis loops for Co nanorings with in-plane field applied parallel, and perpendicular, to the slot direction. The inset schematics indicate the different magnetization configurations of each state that occur during the hysteresis cycle. For the shape SR1 with external field applied parallel to the slot, as shown in Figure 3.5 (a), the hysteresis loop exhibited three steps, corresponding to transitions between saturated onion state, vortex excitation, FC state, and reversed onion state. Conversely, when the external field was applied perpendicular to the slot direction, as shown in Figure 3.5 (b), the shape SR2 exhibited a simple one-step hysteresis loop with good squareness, indicating that the magnetization of the slotted ring reversed abruptly between FC states of opposite chirality. The switching fields were determined to be ~ 800 Oe for the shape SR1 and ~ 700 Oe for the shape SR2. It is noteworthy that the three-step hysteresis loop had been predicted by numerical simulations for ring-shaped Py elements with similar dimensions [15]. However, these experimental results are the first time that such evidence has been observed for Co slotted-ring elements.

Figure 3.6 shows representative phase images corresponding to the states at different stages of the hysteresis loop labeled a–d in Figure 3.5 (a). The saturation configurations corresponded to the onion state and the reversed onion state with strong fringing fields, as shown in Figures 3.6 (a) and (d), respectively. As indicated by the overlaid arrows, the magnetization direction in Figure 3.6 (a) was counterclockwise (CCW) in the upper half of the nanoring, and CW in the lower half, and *vice versa* in Figure 3.6 (d). A vortex with CCW chirality was identified close to the domain wall region of the onion configuration, as visible in Figure 3.6 (b). The precise location of this vortex formation could be related to local defects of the sample or possible geometrical asymmetry between the two branches. The vortex was formed as the external field

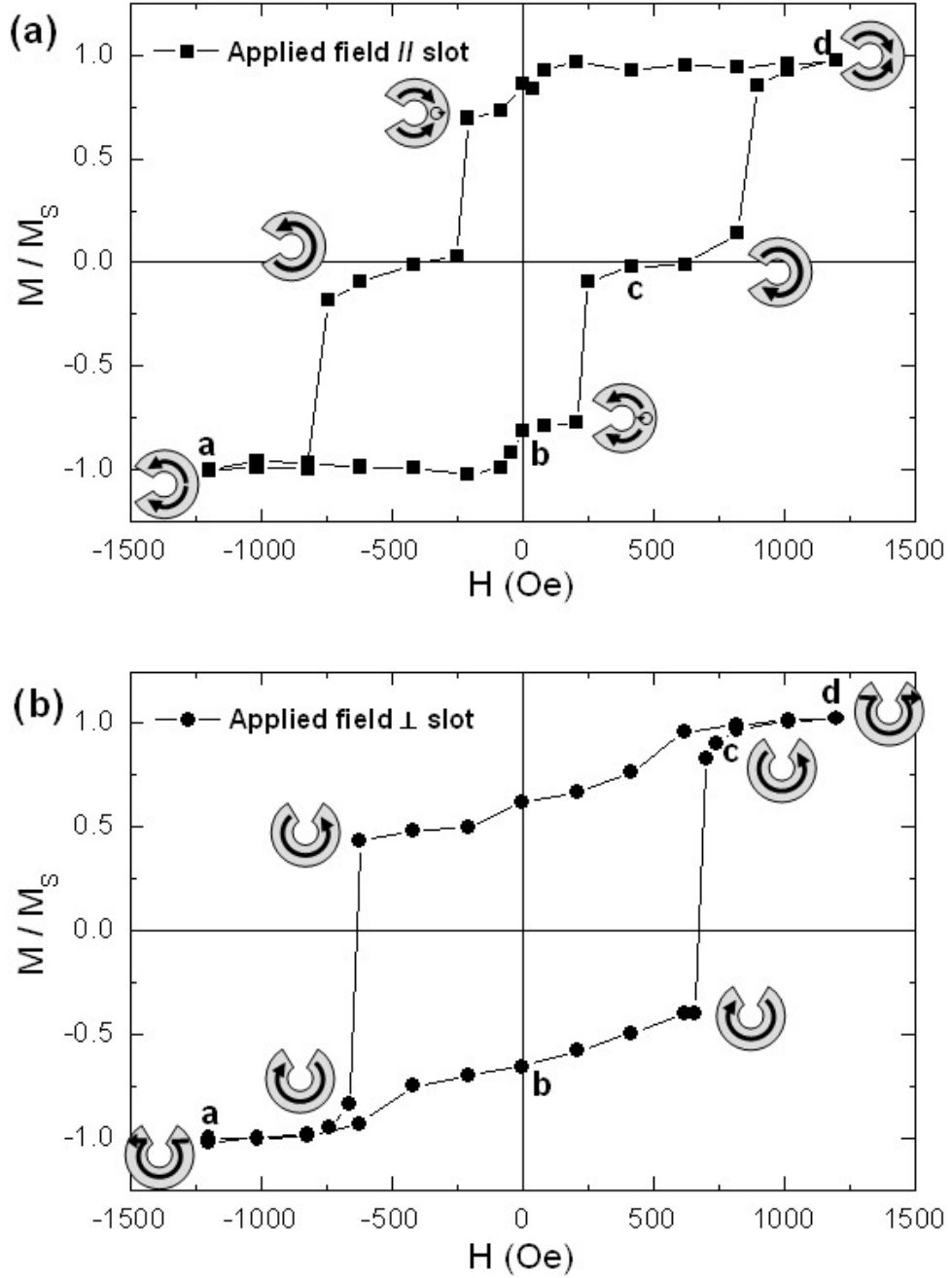


Figure 3.5. (a) Three-step, and (b) one-step, hysteresis loops for Co elements with applied field parallel, and perpendicular, to the slot direction, respectively. The inset schematics indicate the different magnetization configurations that occur during the hysteresis cycle.

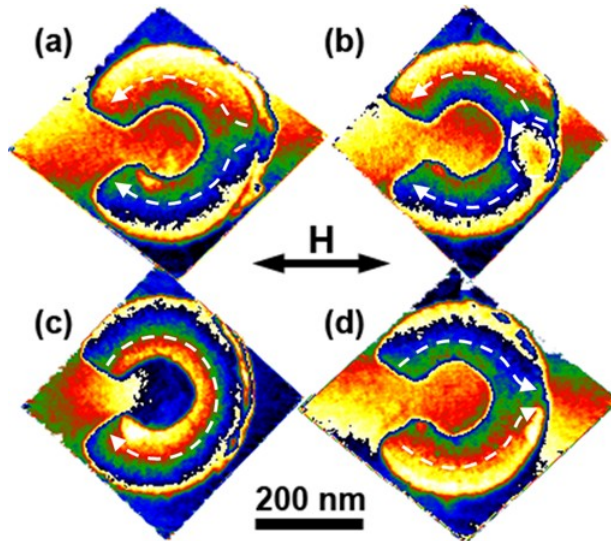


Figure 3.6. Phase images of Co nanoring (SR1) illustrating the magnetization configurations for corresponding states in the hysteresis loop in Figure 3.5 (a): (a) onion state; (b) excitation of vortex at remanence; (c) FC state; and (d) reversed onion state.

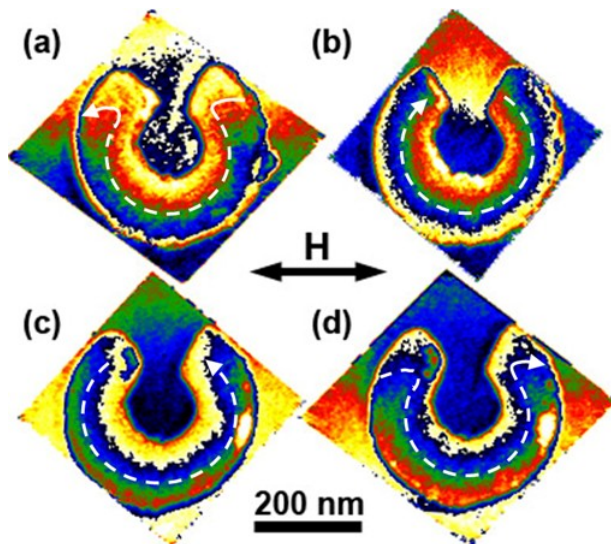


Figure 3.7. Phase images of Co nanoring (SR2) illustrating the magnetization configurations for corresponding states in the hysteresis loop shown in Figure 3.5 (b): (a) Ω state; (b) FC state of CW; (c) FC state of CCW; and (d) reversed Ω state.

approached the remanence condition, and it was then eliminated leaving behind a flux-closure state with CW magnetization and a weak fringing field, as shown in Figure 3.6 (c). The upper half of the element reversed first to form the FC state, followed by switching of the lower half to complete the FC-to-onion transition. The presence of the FC configuration stabilized the Co element, visible as a flat plateau, which was also responsible for the increase of the switching field to ~ 800 Oe, relative to ~ 700 Oe for the shape SR2. Micromagnetic simulations indicated that the transition from onion state to FC state was dependent on the evolution of the vortex. Once the vortex was formed, it could move in two alternative directions: either it would take the shorter route to the end of the associated branch, or else take the longer route towards the other end. Meanwhile, that branch also reversed its magnetization to reach the flux-closure state. The shorter distance would be preferable, although the other case could occasionally occur, as indicated in Figure 3.6 (c).

Figure 3.7 shows phase images corresponding to the states labeled a–d in the hysteresis loop of Figure 3.5 (b). When the field was applied perpendicular to the slot direction, the saturation configurations of shape SR2 appeared as “ Ω ” states, which were FCs with magnetization twisted to the direction of the external field at the slot edges, as shown in Figures 3.7 (a) and (d). As the applied field was reduced below the coercivity (~ 700 Oe), the magnetization relaxed to form a FC state with CW chirality, as visible in Figure 3.7 (b). When the applied field was decreased further to a negative coercivity value, the magnetization of the slotted ring reversed abruptly from the CW FC state to the CCW chirality, as visible in Figure 3.7 (c).

3.4. Comparison Between Experimental Results and Simulations

Micromagnetic simulations were systematically performed for both experimental geometries of regular and slotted rings, with external fields applied parallel or perpendicular to the slot direction, where applicable. The experimental and simulated results are compared in each situation, and also summarized for all three shapes of ring, SR1, and SR2. Figures 3.8 (a)–(c) show the hysteresis loops obtained from experimental electron holograms of the nanoring, and shapes SR1 and SR2, respectively. The coercive fields were determined by averaging the values from both forward and backward cycles of each specific element, as summarized in Table I. Simulated hysteresis loops from micromagnetic modeling for the ring, SR1, and SR2, are shown in Figures 3.8 (d)–(f), respectively. From comparisons between the corresponding loops, it is apparent that the experimental and simulated results are in close quantitative agreement, except that the loop in Figure 3.8 (f) exhibits a more sheared shape than that in Figure 3.8 (c).

Table 3.1. Switching fields measured from experimental and simulated hysteresis loops.

Sample	Switching fields (Oe)	
	Experimental	Simulated
Ring	~800	950±50
SR1	~800	800±100
SR2	~700	850±50

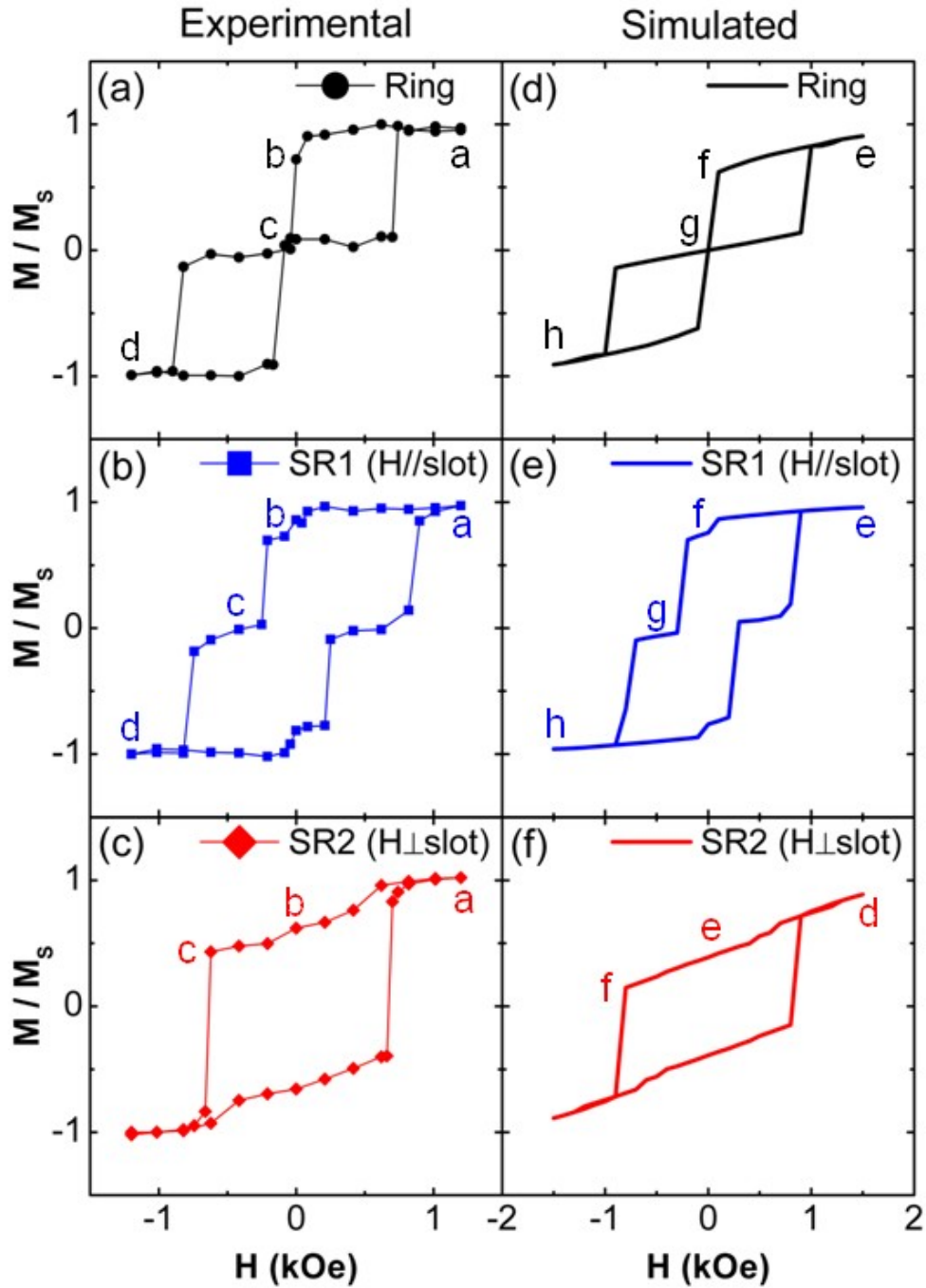


Figure 3.8. (a)–(c) Experimental, and (d)–(f) simulated, hysteresis loops for Co nanoring, slotted nanoring with applied field parallel to slot (SR1), and slotted nanoring with applied field perpendicular to slot (SR2), respectively.

The primary difference in behavior between these three geometries is that shape SR2 shows a one-step hysteresis loop, whereas shape SR1 and the regular nanoring exhibit multiple steps in their loops. These steps represent transitions between distinct and well-defined magnetization configurations, including onion state, vortex formation, and FC state. Moreover, because the occurrence of these steps corresponds to different fields, the elements show different remanent configurations. The representative states, as indicated by letter labels, are illustrated in Figure 3.9: the magnetization configurations, and colors (denoting directions), for the corresponding pairs of measured and simulated images are in excellent agreement. Detailed information about the behavior observed for each specific geometry has already been given. However, it is useful to compare the magnetization reversal and vortex evolution, which were most often observed in numerous experiments for the different shapes.

For the regular ring shape, when the strength of the applied field is decreased from initial saturation, vortices gradually form at the DW regions to minimize the total energy via reduction of the fringing field. A double-vortex (1b and 1f) forms within the onion configuration, when the field is close, but not equal, to zero. These two vortices, having the same CCW chirality, move toward each other, and then annihilate to form a simple CCW FC state at remanence (1c and 1g). Eventually, the FC state becomes a reverse onion state by reversal of the lower half-ring after the field exceeds the switching value (1d and 1h). This latter transition took place too quickly to catch any intermediate states during the observation. Thus, the overall magnetization switching process takes place via the onion-FC-onion mechanism, which is consistent with previous numerical simulations and experimental observations [14, 17].

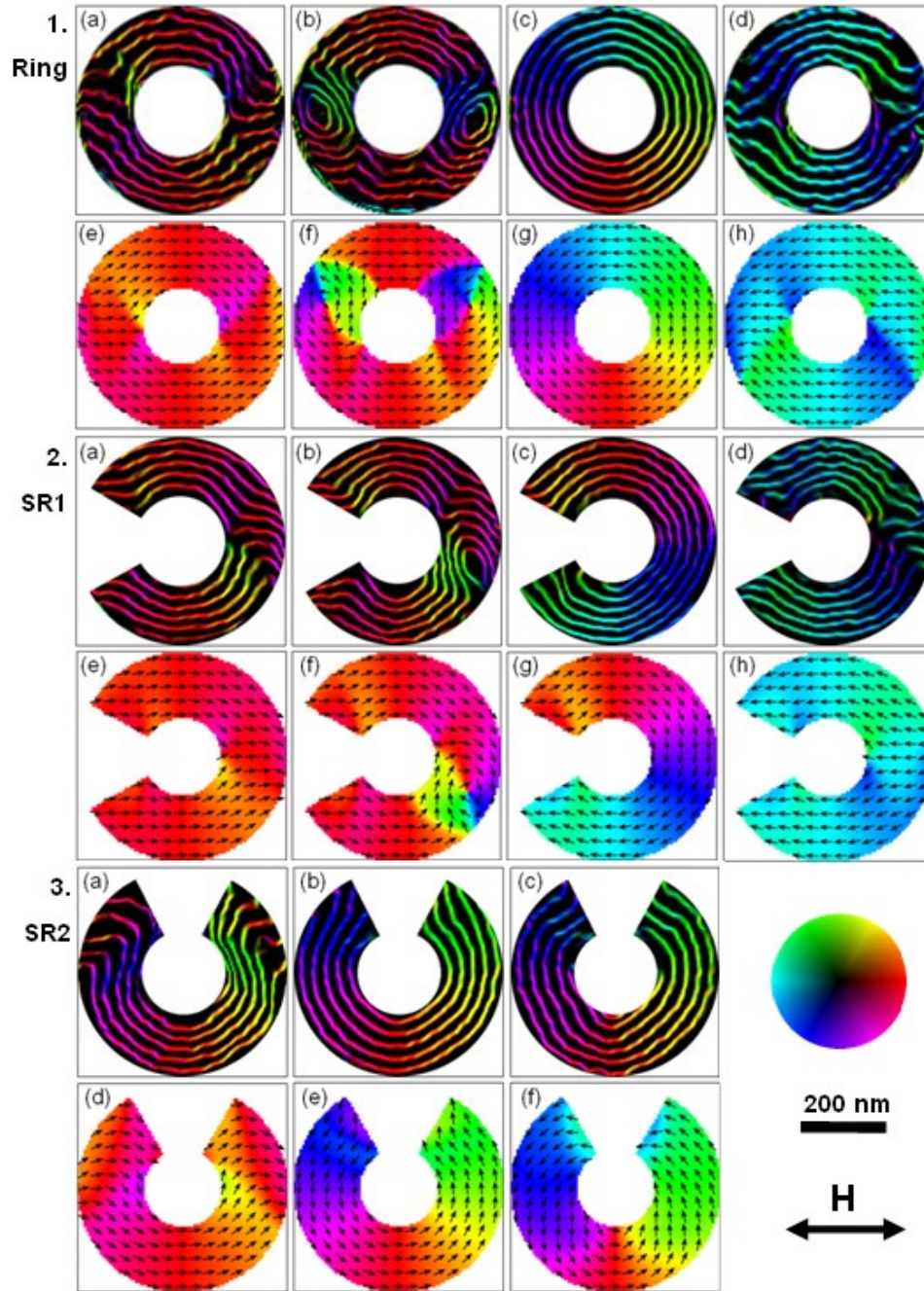


Figure 3.9. Magnetic induction maps for (1) Co ring, (2) SR1, and (3) SR2, comparing the experimental results (upper row) and simulations (lower row). Letter labels refer to corresponding states in Figure 3.8. Applied field along horizontal direction. Contour spacing of $\pi/2$. Magnetization directions indicated by color wheel or overlaid arrows.

The SR1 shape exhibits an onion state at saturation (2a and 2e), and undergoes an onion-FC-onion switching behavior, which is similar to that of the regular ring, because both shapes are symmetrical with respect to the applied field direction. However, since the presence of the slot breaks the horizontal symmetry in the region where a vortex is expected, only one vortex is formed at remanence during the onion-to-FC transition, as was indicated in images 2b and 2f. This single vortex, with clockwise (CW) chirality, moves downward through the entire lower half-branch, and then annihilates at the slot edge to form the CW FC configuration (2c and 2g). The longer path for this single vortex, which requires more energy from the applied field, provides an explanation for the postponed FC appearance relative to that observed for the regular nanoring. Finally, the upper half-branch reverses to reach the reverse onion state (2d and 2h), although no information has been observed that shows the details of this switching process.

In contrast to the multi-step switching behavior for the elements above, the SR2 shape experiences a simple one-step reversal. The saturation configuration appears as an Ω -state (3a and 3d), then relaxes into the CCW FC configuration (3b and 3e) as the applied field is reduced below the coercivity, and retains this state before reversal to the CW FC state occurs (not shown). The change in geometry causes a shape anisotropy perpendicular to the applied field direction, which in turn avoids occurrence of the onion state. However, the Ω -state might be loosely considered as greater than half of the onion configuration, showing magnetization that is more curved than the normal half-onion. The chirality reversal of the FC is thus not due to vortex motion from one slot edge to the other, but most likely involves the vortex that emerges at the lower central part of the inner ring edge, as indicated in image 3c and 3f, which sweeps downward across the ring. This result suggests that the FC-to-onion transitions might also be achieved via a similar process for the nanoring and SR1 samples.

3.5. Discussion

3.5.1. Effects of vortex chirality on switching mechanisms

Based on these observations for the ring and SR1 samples, it appears that the vortex chirality is primarily responsible for the direction of vortex movement and which subsequent configuration is obtained. Thus, a general rule for vortex behavior after onion states can be proposed as a function of the magnetization chiralities of the vortex and the semicircular half-onions. For a vortex with specific chirality present between two semicircular HTH domains, it would be preferable to move toward the half-onion branch with *opposite* chirality, and then subsequently to form an FC state with the *same* chirality, as illustrated in Figure 3.10. From the phenomenological point of view, a vortex can be associated with two half-onion branches: on the side having the half-onion of the same chirality, the magnetization gradually merges into the vortex, whereas on the other side having the half-onion of the opposite chirality, abrupt changes in direction occur at the boundary, as indicated by the obvious contrast of colors. Reduction of exchange energy would require enlargement of regions with similar magnetization, thus leading to the proposed vortex motion. Under this vortex-motion rule, either switching mode could be realized in regular rings: onion-FC-onion transition for double-vortex having the same chirality, and coherent onion rotation for double-vortex having opposite chiralities, as depicted in Figure 3.10 (b) and (c), respectively. The coherent rotation mode did not occur in our experiments, due to intentional removal of the slots. However, only the onion-FC-onion switching mode was identified in regular rings. This contrasts with previously identified cases that showed both modes [14, 17], thus implying strong dependence of the switching mechanism on the lateral dimensions and thickness of the element. Theoretical simulations indicate that similar probabilities for occurrence of either CW or CCW chirality of the vortex would require absolute symmetry of both

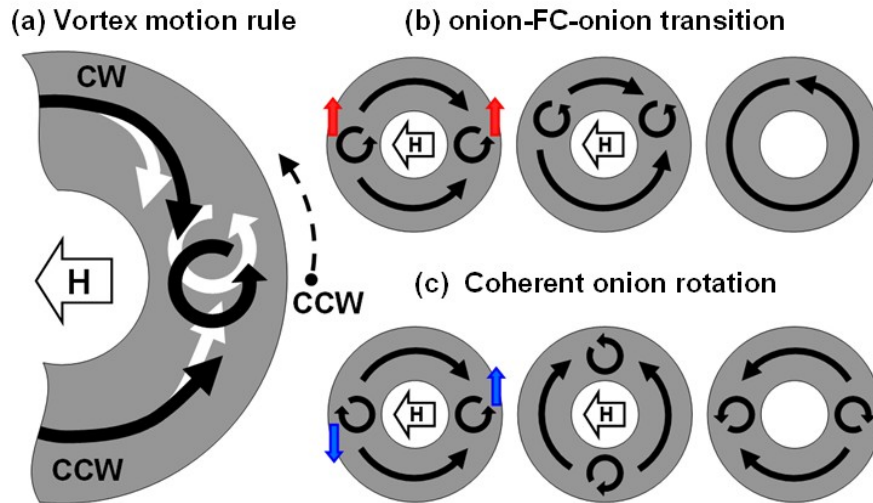


Figure 3.10. Schematics showing vortex controlled switching mechanism for nanorings: (a) vortex motion rule; (b) onion-FC-onion transition; and (c) coherent onion rotation.

element shape and initial magnetization configuration with respect to the in-plane field direction, almost independent of any out-of-plane field. In practice, due to shape variations of an actual element and/or the presence of other defects, one particular vortex chirality would be preferably present and would then predominate during the subsequent reversal.

3.5.2. Effects of shape anisotropy on switching fields

The shape anisotropy of the elements plays a major role in determining the transitions during switching, in terms of affecting the demagnetization field and stray fields around the sample. Since the magnetization was mostly distributed in circular arrangements, FC states in the regular nanorings with little stray field or demagnetization field provide the most stable configurations. In contrast, onion states exhibit much larger stray fields due to magnetization leakage, and have increased demagnetization field within elements due to surface dipole moments. The FC states in slotted rings are,

however, in a situation between the above two states: demagnetization fields slightly increase due to surface dipoles at the slot, but are still less than those in onion states. These suppositions have been confirmed by calculation of demagnetization energies for the Co nanoring and SR1 samples, as shown in Figure 3.11. These OOMMF simulations also indicate that other energies involved, for example, anisotropy energy and exchange energy, are much lower (on an order of magnitude scale) than the demagnetization energy, which is therefore most likely to dominate the switching fields for FC-to-onion transitions. For example, the FC-to-onion transition in the regular nanoring leads to greater increase of demagnetization energy compared to the SR1 shape, and thus results in higher switching field. Overall, the shape anisotropy affects the demagnetization energy within the elements, which in turn causes the switching field changes, consistent with the trends indicated in Table 3.1.

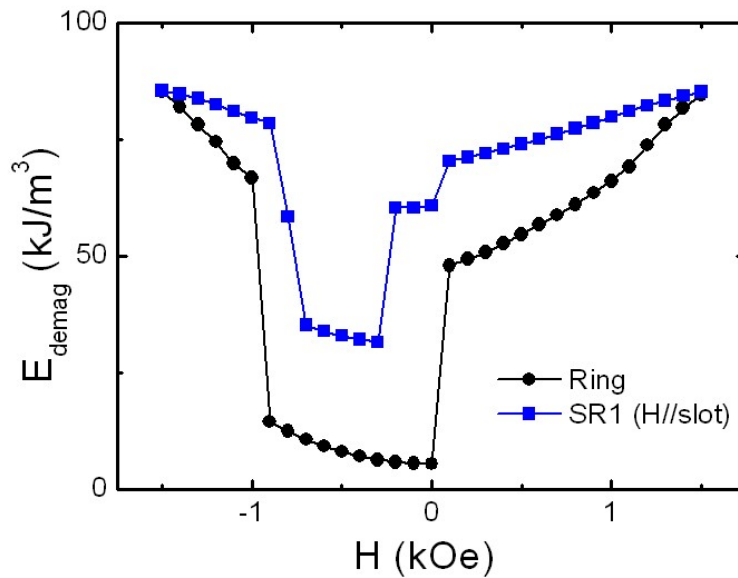


Figure 3.11. Demagnetization energy as a function of applied field for Co nanoring and SR1 shape, as calculated from OOMMF simulations. The calculation is obtained from the forward hysteresis half-cycle (from positive field to negative field).

3.6. Conclusions

The behavior of Co nanorings and slotted nanorings, with orthogonal magnetic fields applied with respect to the slot direction, has been investigated using off-axis electron holography and micromagnetic simulations. The hysteresis loops were quantitatively measured and well-defined states, i.e., onion states, FC states, and vortex formation, were identified for different types of elements, also showing excellent agreement with simulations. The Co nanorings and slotted nanorings with parallel fields exhibited multi-step switching behavior via onion-FC-onion mode, involving the formation and annihilation of single- or double-vortex states. The chirality of the vortex (or vortices) that formed following formation of the onion states was responsible for the switching mechanism. In contrast, slotted rings with perpendicular fields underwent one-step switching by abrupt chirality reversal of the FC states. Introduction of the slot caused shape anisotropy, which in turn affected the switching fields in terms of demagnetization energy. Overall, it can be concluded that the combination of electron holography with micromagnetic simulation provides a powerful approach for extracting detailed information about the switching behavior of nanoscale magnetic elements.

References

- [1] K. He, N. Agarwal, D. J. Smith, and M. R. McCartney, *IEEE Trans. Magn.* 45, 3885 (2009).
- [2] K. He, D. J. Smith, and M. R. McCartney, *J. Appl. Phys.* 107, 09D307 (2010).
- [3] C. A. Ross, *Annu. Rev. Mater. Res.* 31, 203 (2001).
- [4] R. P. Cowburn, *J. Phys. D* 33, R1 (2000).
- [5] R. E. Dunin-Borkowski, M. R. McCartney, B. Kardynal, S. S. P. Parkin, M. R. Scheinfein, and D. J. Smith, *J. Microsc.* 200, 187 (2000).
- [6] T. Schrefl, J. Fidler, K. J. Kirk, and J. N. Chapman, *J. Magn. Magn. Mater.* 175, 193 (1997).
- [7] H. Wang, H. Hu, M. R. McCartney, and D. J. Smith, *J. Magn. Magn. Mater.* 303, 237 (2006).
- [8] R. P. Cowburn, D. K. Koltsov, A. O. Adeyeye, M. E. Welland, and D. M. Tricker, *Phys. Rev. Lett.* 83, 1042 (1999).
- [9] C. A. F. Vaz, L. Lopez-Diaz, M. Kläui, J. A. C. Bland, T. L. Monchesky, J. Unguris, and Z. Cui, *Phys. Rev. B* 67, 140405(R) (2003).
- [10] S. P. Li, D. Peyrade, M. Natali, A. Lebib, Y. Chen, U. Ebels, L. D. Buda, and K. Ounadjela, *Phys. Rev. Lett.* 86, 1102 (2001).
- [11] S. P. Li, W. S. Lew, J. A. C. Bland, M. Natali, A. Lebib, and Y. Chen, *J. Appl. Phys.* 92, 7397 (2002).
- [12] M. Kläui, C. A. F. Vaz, L. Lopez-Diaz, and J. A. C. Bland, *J. Phys.: Condens. Matter* 15, R985 (2003).
- [13] J. Rothman, M. Kläui, L. Lopez-Diaz, C. A. F. Vaz, A. Beloch, J. A. C. Bland, Z. Cui, and R. Speaks, *Phys. Rev. Lett.* 86, 1098 (2001).
- [14] H. Hu, H. Wang, M. R. McCartney, and D. J. Smith, *J. Appl. Phys.* 97, 054305 (2005).
- [15] M. F. Lai, C. N. Liao, Z. H. San, C. P. Lee, Y. P. Hsieh, and T. F. Ho, *J. Appl. Phys.* 103, 07C517 (2008).
- [16] M. H. Park, Y. K. Hong, S. H. Gee, D. W. Erickson, and B. C. Choi, *Appl. Phys. Lett.* 83, 329 (2003).
- [17] F. Q. Zhu, G. W. Chern, O. Tchernyshyov, X. C. Zhu, J. G. Zhu, and C. L. Chien, *Phys. Rev. Lett.* 96, 027205 (2006).

- [18] L. Huang, M. A. Schofield, and Y. Zhu, *Appl. Phys. Lett.* 95, 042501 (2009).
- [19] H. Hu, H. Wang, M. R. McCartney, and D. J. Smith, *Phys. Rev. B* 73, 153401 (2006).
- [20] N. Agarwal, M. R. McCartney, and D. J. Smith, *J. Appl. Phys.* 102, 023911 (2007).
- [21] T. Pokhil, D. Song, and J. Nowak, *J. Appl. Phys.* 87, 6319 (2000).
- [22] J. K. Ha, R. Hertel, and J. Kirschner, *Phys. Rev. B* 67, 224432 (2003).

CHAPTER 4

MAGNETIZATION CONFIGURATIONS AND SWITCHING BEHAVIOR OF Co/Cu/Py SPIN-VALVE SLOTTED NANORINGS

This chapter describes investigation of the different remanent configurations and switching behaviors of multilayer Co/Cu/Py spin-valve slotted nanorings, as a function of the applied field direction relative to the slot directions. It was found that the Co and Py layers can be aligned parallel at saturation and antiparallel at remanence due to the interlayer coupling. Two-step and three-step hysteresis loops were quantitatively determined for slots perpendicular, or parallel, to the applied field, respectively. Magnetization configurations at each stage were directly visualized, and switching mechanisms were also proposed. The results of these studies have been published elsewhere [1, 2].

4.1. Introduction

The spin valve (SV) basically consists of two ferromagnetic (FM) layers separated by a nonmagnetic metallic spacer. The switching fields of the FM layers are usually different, with one layer being magnetically soft, while the other is either intrinsically hard or else exchange-pinned to an adjacent antiferromagnetic layer. The magnetization of the two layers can be switched independently, and thus parallel and antiparallel coupling can be achieved. The giant magnetoresistance (GMR) of the multilayers depends on the change in resistance for the relative magnetization directions of the two layers [3].

Since their discovery in 1986 [4], and because of their useful GMR properties,

spin-valve structures have been intensively studied for technological applications such as magnetic sensors and magnetic random access memory (MRAM), as well as being of fundamental interest due to the variety of magnetization states and the strong interactions between adjacent ferromagnetic layers [5–13]. Micromagnetic simulations have also been carried out to investigate magnetostatic coupling, magnetization reversal mechanisms, and dynamic interactions [10–13]. However, experimental visualization of magnetization distributions for coupled multilayers is still challenging, because most magnetometry techniques lack the resolution or sensitivity to characterize individual nanostructures or the capability to provide quantitative information. Lorentz microscopy has been widely used to characterize the domain structures of monolayer magnetic elements [14]. However, due to the often complicated coupling in spin-valve multilayers, this technique is not readily capable of interpreting changes in magnetic contrast within multilayer elements. Off-axis electron holography represents a powerful approach for characterization of spin-valve structures, because it can measure phase shifts quantitatively and thus extract unique micromagnetic information.

In this chapter, the Co/Cu/Py (where Py = Ni₈₁Fe₁₉) system was selected for the SV elements, and slotted rings with different outer/inner diameters (OD/ID) and slot angles (α) were chosen for the SV element shapes, as shown in Figure 4.1. Elements of different sizes were patterned into 3×3 arrays, with the separation between elements at least twice the OD, and the separation between arrays even greater, to eliminate any possibility of magnetostatic interactions. A variety of combinations of geometrical parameters, with nominal OD/ID of 300/100, 400/100, 400/200, 500/200, 600/200 nm, and slot angles of 30°, 60°, 90°, were patterned onto the silicon nitride membranes using standard EBL and lift-off methods (details as described in §2.2).

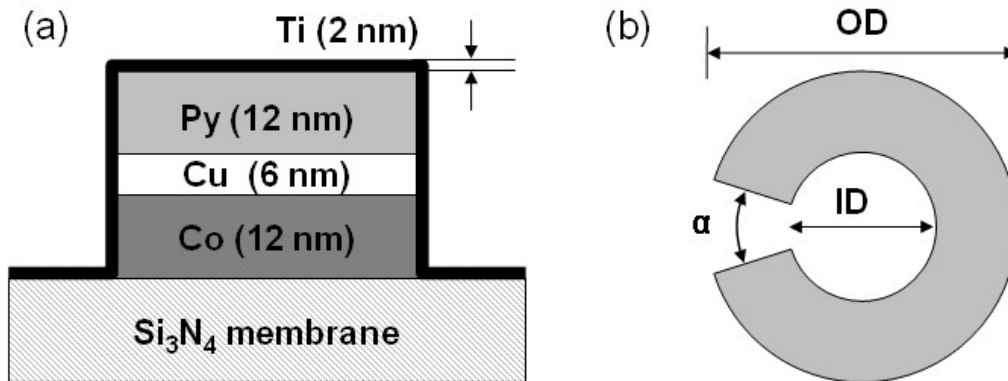


Figure 4.1. Schematics illustrating (a) the structure of trilayer stack, and (b) the shape of slotted ring, for Co/Cu/Py SV elements.

4.2. Magnetization Configurations and Interlayer Coupling at Remanent State

As-prepared elements were observed in the Lorentz TEM mode, with the magnetic field applied parallel or perpendicular to the slot bisecting direction. Figure 4.2 (a) shows a typical 3×3 element array of SV elements with nominal $OD/ID = 400/200$ nm and $\alpha = 60^\circ$ at remanent state (although the actual inner diameter is ~ 150 nm after fabrication). Figure 3.2 (b) shows an under-focused Lorentz image, which clearly displays Fresnel contrast within the elements but differences between the different states are not easily distinguished. Thus, detailed information about the magnetization behavior cannot be easily extracted or interpreted using this technique.

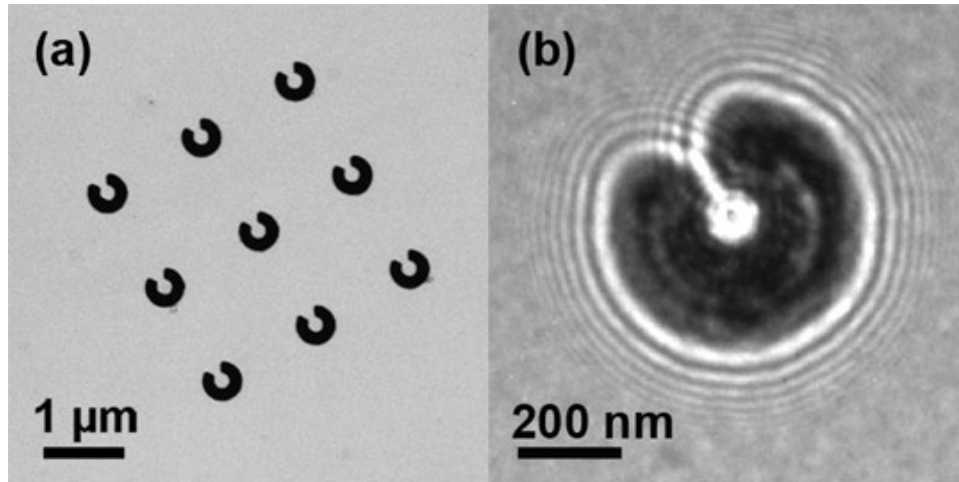


Figure 4.2. (a) In-focus image showing as-prepared array of Co/Cu/Py SV elements (OD/ID= 400/200nm, $\alpha = 60^\circ$); (b) defocused Fresnel image of single Co/Cu/Py SV element in remanent state.

Off-axis electron holograms of SV elements at remanent state were recorded, and typical reconstructed phase images are shown in Figure 4.3. Based on observations of several arrays of elements, it was found that the onion state was primarily obtained when the initial in-plane saturation field was applied parallel to the slot direction, as shown in Figure 4.3 (a), whereas the flux-closure (FC) state was dominant when the saturation field was applied perpendicular to the slot direction, as visible in Figure 4.3 (b). For better visualization of the magnetization configurations, equiphase contours have been superimposed on the phase images, with the contour lines along the direction of magnetic induction, so that the contour density is then proportional to the magnitude of the magnetization (M_s). The measured phase shift perpendicular to the applied field direction was ~ 1.65 rad across the ring in Figure 4.3 (b). The slightly decreased contour density and therefore M_s for the element in Figure 4.3 (a) is likely to be due to the stronger fringing field for the onion state which decreased the net measured magnetic field,

compared with the FC state in (b). In comparison with the phase shifts expected for monolayer Co slotted rings [15], it was clear that the remanent state of the trilayer structure was dominated by the magnetically more massive Co layer, as seen previously for several simple Co/Au/Ni SV trilayer shapes [13], while the occasional presence of extra vortices (not shown) was likely due to local coupling with the Py layer.

Further quantitative analysis clarified the interactions between the Co and Py layers at remanent state. Figures 4.4 (a) and (b) show the phase images at remanence after saturation in opposite directions: these are both FC states, with chirality of counterclockwise (CCW), and clockwise (CW), respectively. Line profiles were plotted

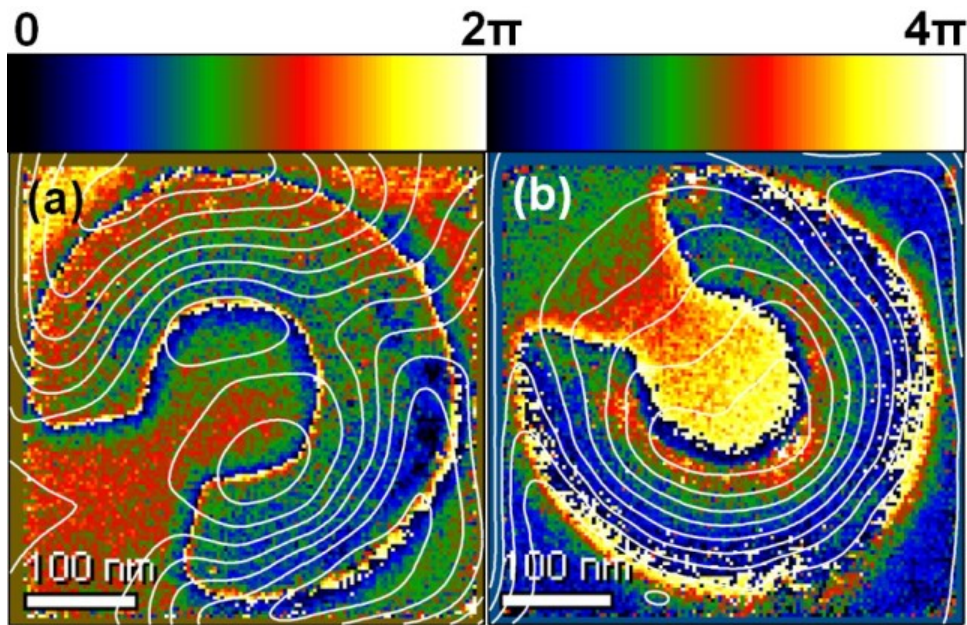


Figure 4.3. Reconstructed holographic phase images of Co/Cu/Py SV elements showing different remanent configurations: (a) onion state; (b) FC state. Initial saturation direction from bottom-left to top-right. Color bar shows phase in images ranging from 0 to 4π . Equiphase contours represent phase shifts due to magnetic induction, with contour spacing of 0.2 radians.

out at the same positions of the elements, as shown in Figure 4.4 (c). Measurements show that the slopes of the phase shifts inside the SV elements are -0.0401 rad/nm and 0.0126 rad/nm, corresponding to 2.67 T CCW and 0.84 T CW, respectively. These values are well matched with the sum and difference of the magnetization of separate Co and Py layers, indicating that both parallel and antiparallel configurations can exist at remanence. Although the antiparallel state should be favored in order to minimize demagnetization

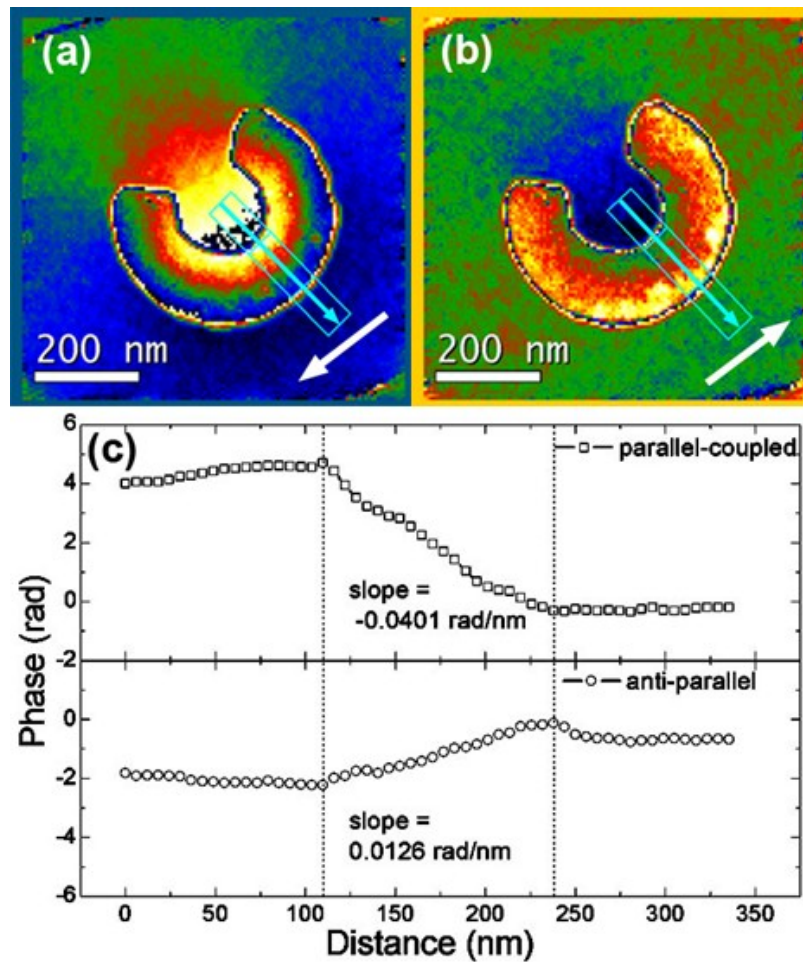


Figure 4.4. Phase images of (a) parallel- and (b) antiparallel-coupled configurations of slotted SV element at remanent state. (c) Corresponding line profiles after removal of MIP contributions. Saturation directions indicated by white arrows.

energy, the occasional occurrence of parallel states probably illustrates that the switching field for the Py layer is quite close to remanence.

The effect of the SV element size on remanent configuration was also studied. Based on observations of several individual elements for each size, it was found that the remanent states of small elements (OD/ID = 300/100 nm) exhibited stable flux closures with consistently antiparallel configurations. As the diameter and width of the rings was increased, this magnetization state became unstable, and parallel-coupled configurations and/or vortices started to appear, typically when the OD was ≥ 500 nm. In addition, changing the slot angle from 30° to 90° did not seem to affect remanence very much. Thus, nanorings with OD/ID of 400/200 nm and slot angle of 60° were chosen for investigation of typical switching behavior.

4.3. Switching Behavior of Slotted Nanorings

Switching behavior of the SV elements was investigated by a sequence of specimen tilting in an *in situ* applied vertical magnetic field. The objective lens current was slightly turned on and set to ~ 1000 mA, corresponding to a vertical magnetic field of ~ 2400 Oe. Thus, an in-plane field with maximum of ~ 1200 Oe at $\pm 30^\circ$ tilting positions could be applied parallel or perpendicular to the slot direction.

4.3.1. Applied field perpendicular to slot direction

Experimental values of the in-plane magnetization within individual SV nanorings with applied field perpendicular to slot direction were extracted from reconstructed phase images at different specimen tilting angles and normalized to unity at saturation, using the method described in section §2.4.2. Figure 4.5 illustrates entire hysteresis loops for a specific SV element through a major cycle, where both layers were completely reversed, as well as a minor cycle, where only the soft (Py) layer was

swapped but the hard (Co) layer remained unchanged. The major hysteresis loop indicated two steps, corresponding to separate reversals of the Py and Co layers, respectively. The overlaid schematics indicate the different magnetic coupling between the two layers: parallel coupled Ω -states at saturation (a and d), antiparallel coupled FC states (c and f) at remanence, and parallel coupled FC states (b and e) as intermediate states in between. Figure 4.6 shows representative magnetization configurations corresponding to states a–c in the forward cycle of the hysteresis loop, and *vice versa* in the other half cycle. The Co layer dominated the magnetization change from Ω - to FC-state, while reversal of the Py layer reduced the contour density. It was found that the

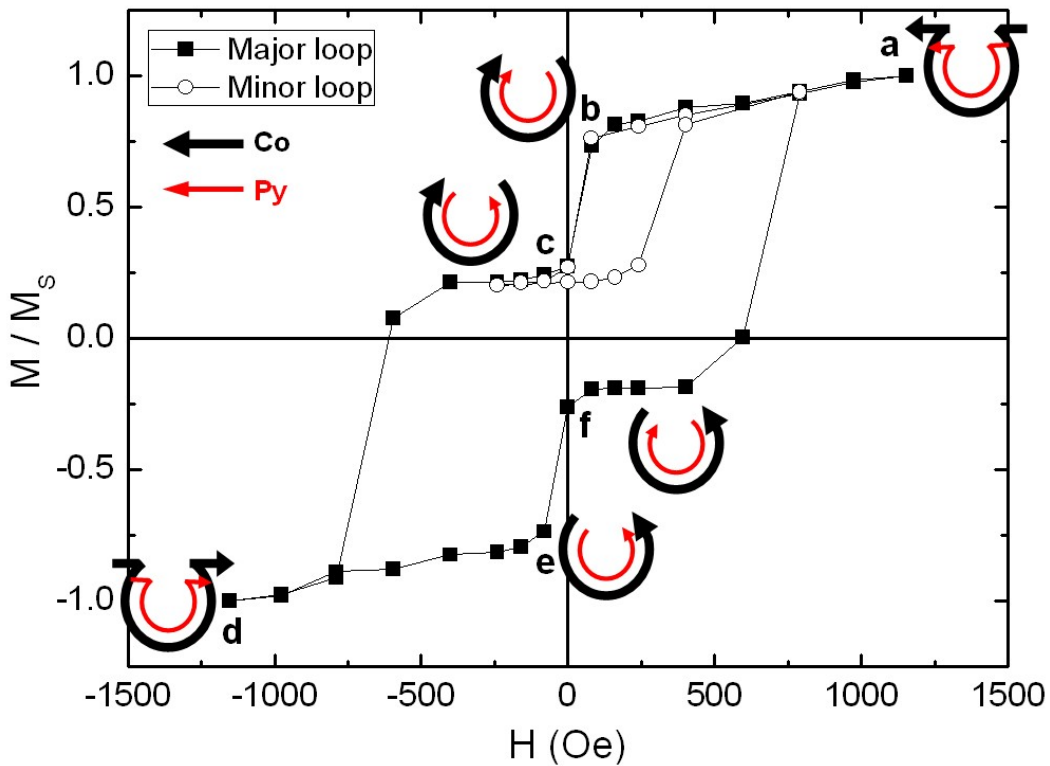


Figure 4.5 Hysteresis loops for Co/Cu/Py SV element through major and minor cycles. Applied field perpendicular to the slot direction. Insert schematics indicate different magnetic coupling between Co and Py layers during the hysteresis cycle.

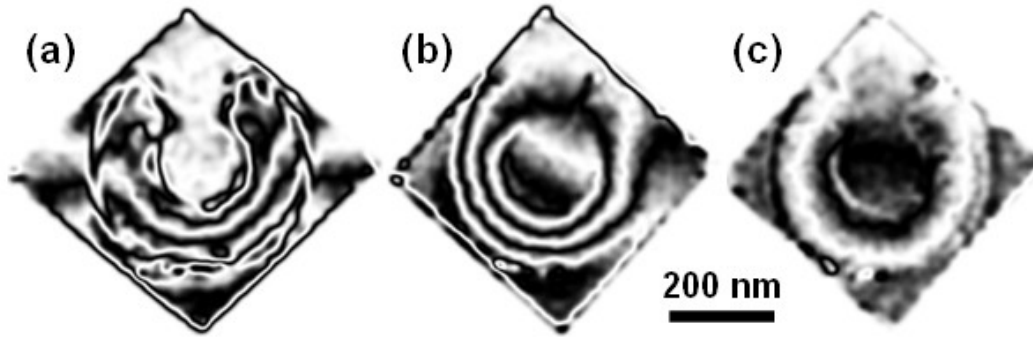


Figure 4.6. Phase contour (4× amplified) images showing representative magnetization states corresponding to labels a–c in Figure 4.7: (a) parallel coupled Ω -state; (b) parallel coupled FC; (c) antiparallel coupled FC.

switching field for the Py layer was very close to remanence, which would explain the observations of both parallel and antiparallel remanent states. The switching fields needed to reverse both ferromagnetic layers were on the order of 700 Oe, which is consistent with the coercivity of monolayer Co reported in Chapter 3.

The minor hysteresis cycle, as shown in Figure 4.5, was also performed in order to examine the switching behavior of the free (Py) layer. The entire minor loop exhibited a shift with respect to remanence, which is analogous to the exchange bias effect observed in the ferromagnetic/antiferromagnetic (FM/AFM) system. However, the direction of shift is along the positive field direction, which is contrary to the negative shift in the FM/AFM structure. This is due to the interlayer coupling of the underlying hard Co layer, which provided a biasing field along its saturation direction. The bias magnetic field was determined to be ~ 200 Oe, and the coercivity of the Py layer was measured to be ~ 150 Oe, corresponding to the half width of the minor loop. This property of the minor hysteresis loop could prove to be useful for applications of hard disk reading head, MRAM, and magnetic sensors.

4.3.2. Applied field parallel to slot direction

The switching behavior of the Co/Cu/Py SV elements through a complete hysteresis cycle was also investigated for the applied field parallel to the slot direction. Figure 4.7 illustrates an entire loop measured directly from the experimental holographic phase images, followed by normalization to unity at saturation, where the slight horizontal shift of the loop is attributed to a zero error in sample tilting. The different magnitudes of M/M_s for the upper and lower half of the hysteresis loop is probably attributable to the shift of the entire hysteresis loop, which is possibly caused by the residual vertical magnetic field. It is suspected that the decreasing magnitudes of the plateaus are because the magnetization is gradually rotating away from the saturation

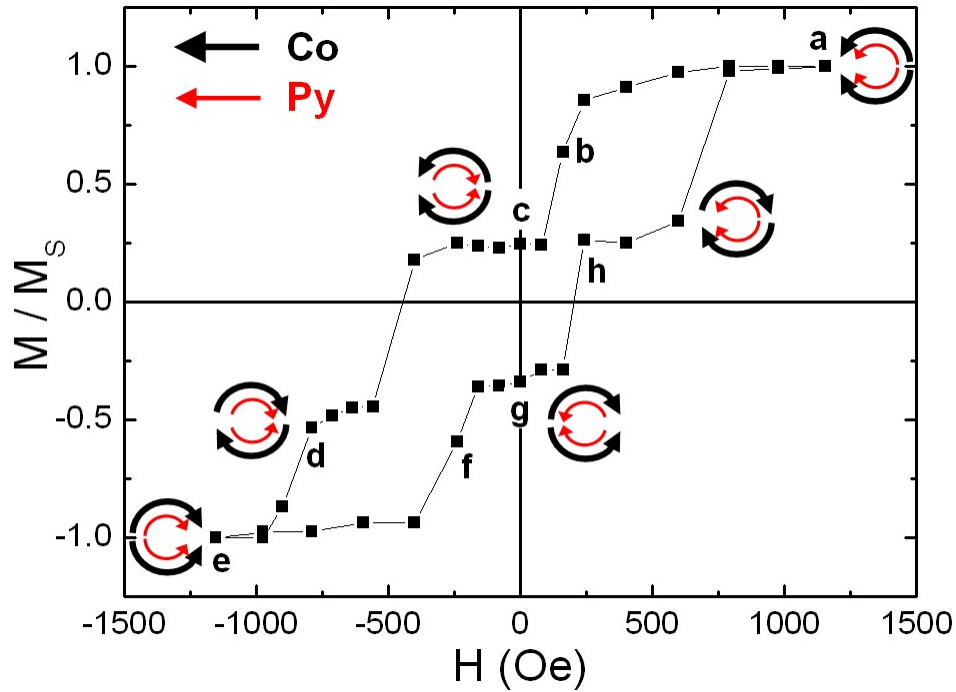


Figure 4.7. Three-step hysteresis loops for Co/Cu/Py SV nanoring with applied magnetic field parallel to the slot direction. Insert schematics indicate different magnetic coupling between Co and Py layers with onion configurations during the hysteresis cycle.

state as the applied field starts to be reduced. However, this decrease is relatively small compared with the reversal of layers.

Unlike the two-step hysteresis loop for the SV element with external field applied *perpendicular* to the slot direction, this loop exhibited three steps when the field was applied *parallel* to the slot. The overlaid schematics indicate the different configurations of the onion states: parallel-coupled onion states at saturation (a and e) and antiparallel-coupled onion states (c and g) at remanence, as well as two extra intermediate states (d and h) consisting of half-parallel-coupled and half-antiparallel-coupled. The occurrence of these extra intermediate states stabilized the Co layer, in effect delaying its full reversal until a switching field of ~ 800 Oe was reached, which is to be compared with the value of ~ 700 Oe obtained with the field applied perpendicular to the slot.

Figure 4.8 shows representative phase images corresponding to the labels a–h in different stages of the hysteresis loop in Figure 4.7. Each configuration could be considered as a combination of onion state and flux closure with parallel or anti-parallel coupling between the separate Co and Py layers. The parallel-coupled saturation states and the antiparallel-coupled remanent states of the onion configuration can be identified, as shown in (a) (e) and (c) (g), respectively. The transition from saturation to remanence was observed, as shown in (b) and (f). The upper half of the Py layer reversed first to form a FC state, followed by reversal of the other half, while the Co layer remained in the onion state. The intermediate states between remanence and reverse saturation were visualized, as shown in (d) and (h), in which the upper half of the Co layer first switched from the onion state to flux closure, and then the other half reversed at higher field values to form the opposite onion state. The results indicate that the Py and Co layers both performed a two-step switching mechanism: from onion state to FC state and from flux-closure to reverse onion state.

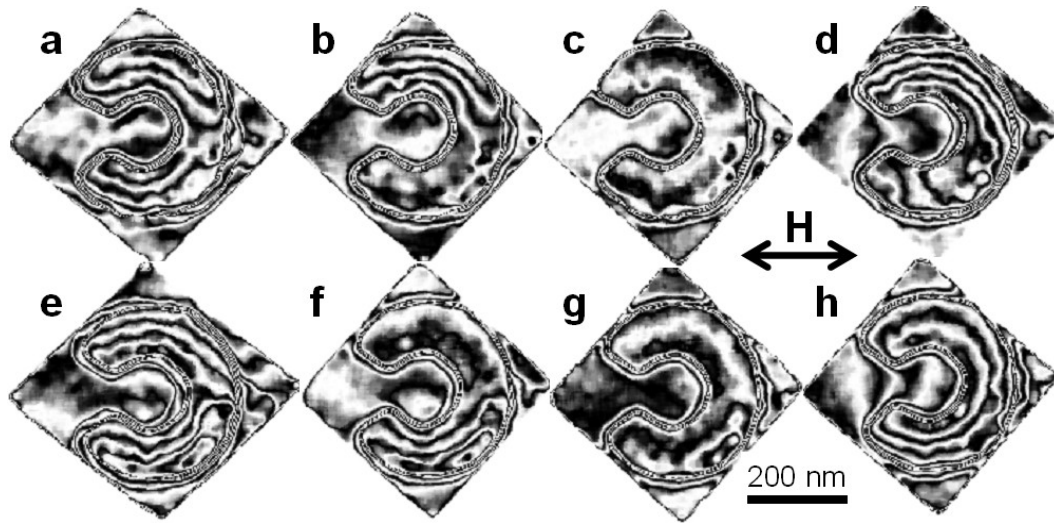


Figure 4.8. Phase contour ($4\times$ amplified) images of SV element illustrating the magnetization configurations of corresponding states in the hysteresis loop of Figure 4.7. Applied fields are parallel to the slot direction, horizontally from right to left for (a)–(d), and from left to right for (e)–(h).

The three-step hysteresis loop can be schematically drawn with regard to the behavior of the individual Co and Py layers, as shown plotted in Figure 4.9. The lack of flatness of the plateaus would be due to the gradually reduced alignments of the magnetization. The Co layer exhibited a two-step hysteresis loop with two plateaus corresponding to flux-closure states, which is in good agreement with the previous experimental data from monolayered Co elements. The Py layer showed a simple hysteresis loop without obvious steps due to the narrow switching field distribution, although extra steps might be visible if more data could be obtained. It is noteworthy that the Py layer underwent a reverse *clockwise* loop, where magnetization reversal occurred before the remanence condition, unlike normal hysteresis. This behavior is due to the strong antiparallel coupling with the Co layer, which is magnetically harder, and thus dominates the overall behavior of the SV structure.

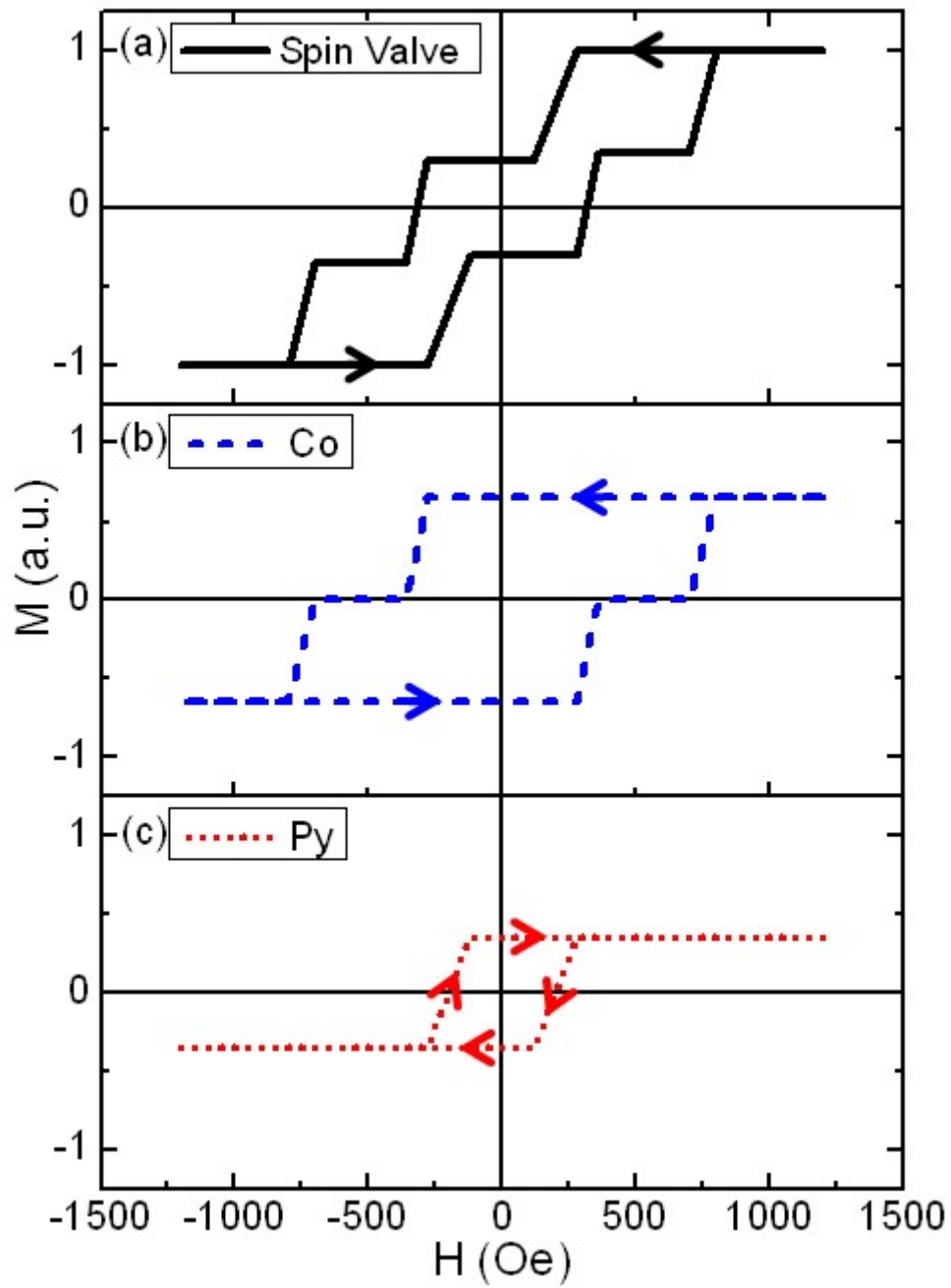


Figure 4.9. (a) Schematic hysteresis loop after Figure 4.7. Magnetic components separated to represent the individual behavior of (b) Co, and (c) Py layers.

4.4. Conclusions

The remanent magnetization configurations and switching behavior of Co/Cu/Py slotted nanoring SV elements as function of applied field direction relative to the slot orientation have been characterized using off-axis electron holography. At the remanent condition, the Co and Py layers align in the antiparallel-coupled configuration, with predominant states in FC or onion states with the applied field perpendicular or parallel to the slot direction, respectively. The SV nanorings exhibited multi-step switching mechanisms, which is attributed to intrinsic coercivity difference and magnetic coupling between the Co and Py layers. When the external field was applied perpendicular to the slot, the elements underwent a two-step hysteresis loop, corresponding to separate reversal of Py and Co layer. When the external field was applied parallel to the slot, the spin valve showed a well-defined three-step hysteresis loop, corresponding to transitions between saturation, remanence, and intermediate states. In the latter situation, both Co and Py layers performed a two-step switching mechanism via onion-FC-onion transition.

References

- [1] K. He, D. J. Smith, and M. R. McCartney, *J. Appl. Phys.* 105, 07D517 (2009).
- [2] K. He, D. J. Smith, and M. R. McCartney, *Appl. Phys. Lett.* 94, 172503 (2009).
- [3] B. Dieny, *J. Magn. Magn. Mater.* 136, 335 (1994).
- [4] P. Grünberg, R. Schreiber, Y. Pang, M. B. Brodsky, and H. Sowers, *Phys. Rev. Lett.* 57, 2442 (1986).
- [5] B. Dieny, V. S. Speriosu, S. S. P. Parkin, B. A. Gurney, D. R. Wilhoit, and D. Mauri, *Phys. Rev. B* 43, 1297 (1991).
- [6] K. S. Buchanan, K. Yu. Guslienko, A. Doran, S. D. Bader, and V. Novosad, *Phys. Rev. B* 72, 134415 (2005).
- [7] C. A. Ross, F. J. Castaño, E. Rodriguez, S. Haratani, B. Vögeli, and H. I. Smith, *J. Appl. Phys.* 97, 053902 (2005).
- [8] C. K. Lim, J. N. Chapman, M. Rahman, A. B. Johnston, and K. O'Donnell, *J. Magn. Magn. Mater.* 238, 301 (2002).
- [9] F. B. Mancoff and S. E. Russek, *IEEE Trans. Magn.* 38, 2853 (2002).
- [10] J. G. Zhu, Y. F. Zheng, and G. A. Prinz, *J. Appl. Phys.* 87, 6668 (2000).
- [11] Z. Li and S. Zhang, *Phys. Rev. B* 68, 024404 (2003).
- [12] G. X. Li and S. X. Wang, *IEEE Trans. Magn.* 39, 3313 (2003).
- [13] D. J. Smith, R. E. Dunin-Borkowski, M. R. McCartney, B. Kardynal, and M. R. Scheinfein, *J. Appl. Phys.* 87, 7400 (2000).
- [14] J. N. Chapman, *J. Phys. D: Appl. Phys.* 17, 623 (1984).
- [15] N. Agarwal, M. R. McCartney, and D. J. Smith, *J. Appl. Phys.* 102, 023911 (2007).

CHAPTER 5
MAGNETIC DOMAIN-WALL MOTION IN NOTCHED PERMALLOY
NANOWIRES

This chapter describes the characterization of domain-wall (DW) propagation driven by an *in situ* magnetic field within Permalloy nanowires (Py NWs), using off-axis electron holography and Lorentz microscopy. DWs were directly observed and different aspects of their behavior, including nucleation, injection, pinning, depinning, relaxation, and annihilation, were studied. A unique asymmetrical DW pinning behavior was also identified, which was attributed to DW chirality relative to the sense of rotation around the notch. The transverse DWs could be relaxed into vortex DWs, and then annihilated in a reversed field. Micromagnetic simulations were performed to provide further information in support of the experimental observations. Results from this investigation have been published elsewhere [1].

5.1. Introduction

Magnetic domains and DW motion in ferromagnetic NWs have recently attracted intense interest due to their potential significance from the viewpoints of both practical applications and fundamental science [2–5]. Magnetic logic and memory devices, where the key issue is to manipulate the DW configurations using magnetic fields and/or spin-polarized current originating from the spin-transfer torque effect, have been theoretically proposed and demonstrated experimentally [2–6]. Detailed knowledge of DW nucleation and propagation is essential for development of these devices. Artificial NW constrictions of different geometries fabricated as trapping sites for DWs have been investigated using

both numerical simulations and experimental observations [7–16]. Such constrictions can be considered as potential wells or barriers depending on their shape and the injected DW structure [7–10]. Experimental studies of DW pinning and depinning have involved indirect measurements of magnetization hysteresis loops and magnetoresistance changes of the entire NW or regions distant from the DW trapping site [2–8]. However, these techniques typically lack an ability to provide direct visualization of the DW behavior, e.g., type and position.

Nanoscale observation of magnetization distributions around DW trapping sites is important, but remains challenging. Limited studies of magnetic DWs, mostly vortex DWs (VDWs), have been reported using magnetic force microscopy (MFM) [18], photoemission electron microscopy (PEEM) [13], magnetic transmission x-ray microscopy (MTXM) [14], scanning electron microscopy with polarization analysis (SEMPA) [19], Lorentz microscopy [9–11], and electron holography [15–17].

In this chapter, magnetic-field-driven DW motion in Py NWs has been investigated using off-axis electron holography and Lorentz microscopy. Figure 5.1 sketches the design of the Py NW, where the notch on one side of the NW is employed as a geometrical constriction to trap the DW, and the nucleation pad at one end of the NW is designed to provide control of the chirality [clockwise (CW), counterclockwise (CCW)] of the injected DW [9]. The Py NWs were fabricated using the standard EBL and lift-off process. A Philips-FEI CM200 FEG TEM was operated in Lorentz mode with an *in situ* magnetic field of ~440 Oe applied in the vertical direction by partially exciting the objective lens. The desired in-plane component, which caused DW motion during observation, was then obtained by tilting the holder in the field within the range of $\pm 20^\circ$.

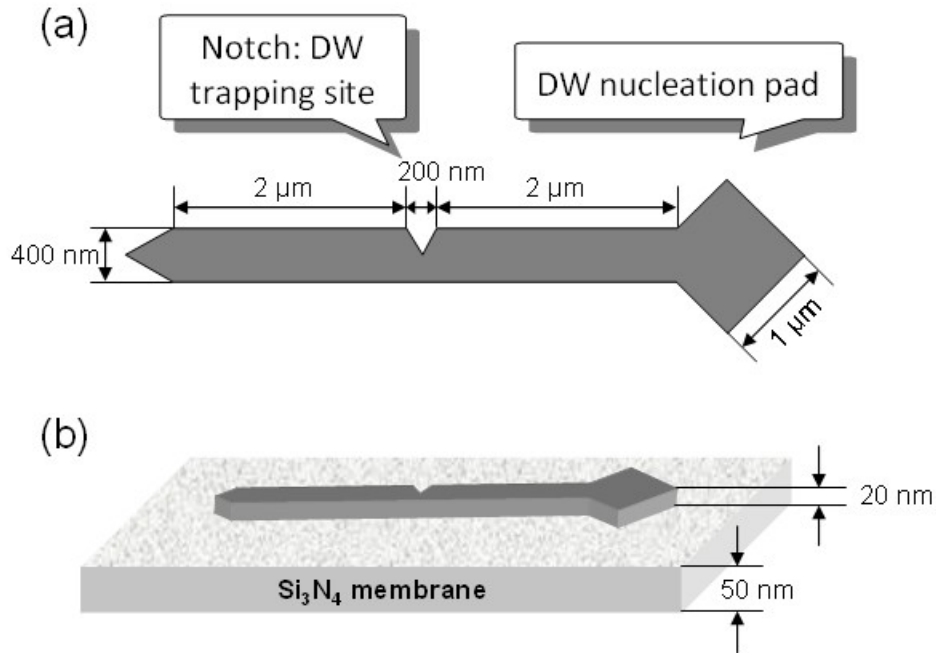


Figure 5.1. Schematic drawings showing the design of Py NWs: (a) plan-view showing shape and dimensions; (b) 3D view showing Py NW on the amorphous nitride membrane.

5.2. Remanent States

Figure 5.2 (a) shows the Lorentz TEM image of a typical Py NW. The NW geometry is well-defined with dimensions of $\sim 5 \mu\text{m}$ in length, $\sim 400 \text{ nm}$ in width, and $\sim 20 \text{ nm}$ in nominal thickness. A diamond-shape pad was connected to the wire at one end for DW nucleation, whereas a sharp wedge was used at the other end to prevent DW nucleation. The actual notch was in trapezoidal shape, with depth of $\sim 200 \text{ nm}$ and opening of $\sim 300 \text{ nm}$, rather than the designed equilateral triangle shape. The shape deviation was likely due to the slightly over-exposed photoresist mask during EBL patterning. However, this should not affect the property of the notch to trap DWs during their motion.

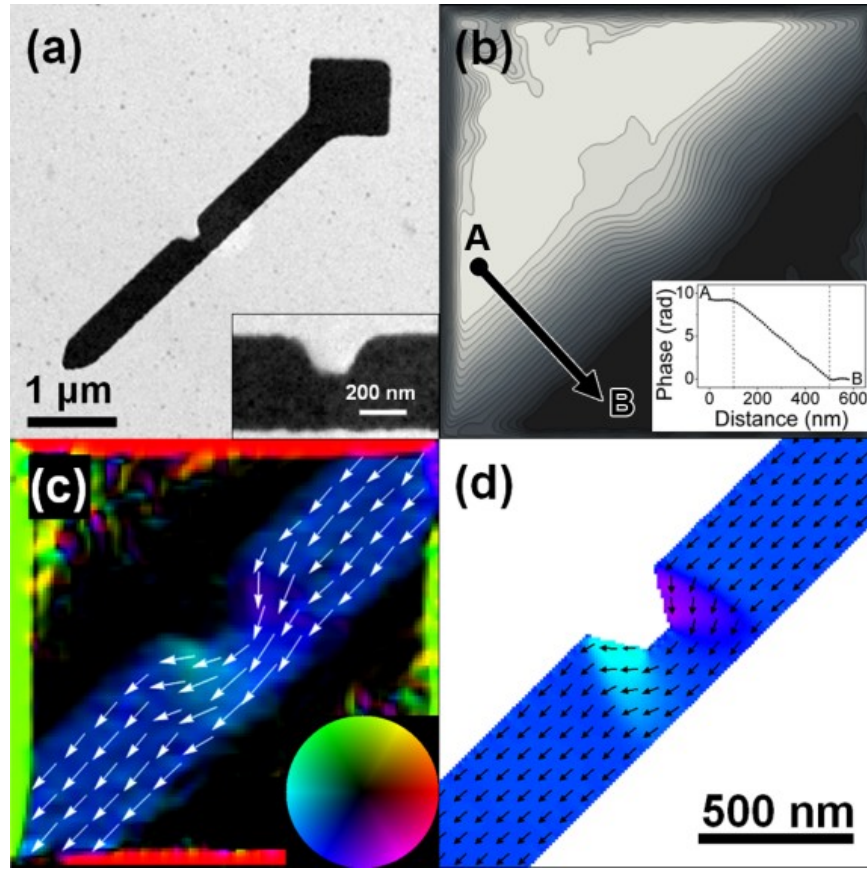


Figure 5.2. (a) Lorentz image of Py nanowire as fabricated, with inset showing enlarged view of trapezoid notch. (b) Phase shift; (c) reconstructed magnetic induction map; and (d) calculated magnetic induction map; of Py nanowire at remanent state. Field directions indicated by color wheel or overlaid arrows.

Figure 5.2 (b) shows the magnetic contribution to the phase shift across a typical NW, as extracted from pairs of electron holograms taken at the remanent state after initial saturation in opposite directions. The equiphase contours represent the distribution of magnetic induction, and line profile from A to B is plotted in the figure inset. The linear change of phase from one side of the NW to the other side indicates uniformly distributed magnetic induction along the NW, although the induction becomes curled in the vicinity of the notch. From the measured phase shift of ~ 9 rad across the NW, the magnetically

effective thickness was calculated to be ~ 15 nm. This value is less than the nominal thickness of 20 nm, most likely due to some oxidization of the Py layer, and was used in the micromagnetic simulations. In order to clarify magnetization directions, the phase images were converted into magnetic induction maps, using a color wheel for denoting specific directions, as shown in Figure 5.2 (c). The remanent induction map for the same structure, as calculated by OOMMF simulations and shown in Figure 5.2 (d), was in close agreement with the experimental observation. The magnetization curling around the notch can be either CW (as shown) or CCW, depending on the initial saturation direction, which is also defined in this study as the chirality (or sense of rotation) of the notch.

5.3. Asymmetrical Domain-Wall Pinning Behavior

The DW motion as a function of the in-plane applied field strength was investigated using both Lorentz TEM and electron holography. The larger field of view provided by Lorentz TEM observation provides a simple way to detect DWs within the entire NW, whereas electron holography enables closer visualization and detailed quantification of specific local domain structures at higher magnifications. The upper part of Figure 5.3 shows a montage of Lorentz TEM images of the same Py NW but with different in-plane magnetic fields, where the positions of the DWs are visible with black or white (Fresnel) contrast. Detailed magnetic induction maps from the specific indicated regions were reconstructed from corresponding holographic phase images and these are shown below each Lorentz image. Following initial saturation along top-right direction, DW nucleation was observed at the remanent state, as illustrated in Figure 5.3 (I). The NW formed a single-domain state, with a 45° DW between the wire and the nucleation pad, which was in a four-domain flux-closure (FC) configuration. The rotation of the FC states can be defined as the chirality of the nucleation pad, which correlates with the

black-white contrast of the DWs and central spots: white for CW, and black for CCW. An *in situ* magnetic field was applied opposite to the initial saturation direction (bottom-left, as indicated by the black arrow), and then its strength was gradually increased to initiate DW movement. When the applied field reached ~ 54 Oe, the DW was injected into the NW, as shown in Figure 5.3 (II). A triangular transverse DW (TDW) formed between the two head-to-head (HTH) domains, which was different from the VDW formation reported previously [9,10,17–19], and it was still attached by a common DW to the nucleation pad. As the field was further increased to ~ 71 Oe, as shown in Figure 5.3 (III), the TDW became pinned at the notch, where the magnetic induction became kinked between two HTH domains. When the applied field reached ~ 137 Oe, the TDW became depinned from the notch, resulting in an abrupt reversal of the remainder of the NW, as indicated in Figure 5.3 (IV).

A backward or reverse half-cycle was carried out, with the initial saturated magnetization pointing toward the narrow end of the NW, and the direction of the increasing field toward the pad. Representative states that occurred during DW motion for this situation are shown in Figures 5.3 (V) – (VII), respectively. DW nucleation was again observed at the remanence condition, and the nucleation pad was retained in the same CW FC state as in the forward cycle by careful control of the magnetizing process [9]. DW injection into the NW was initiated at the higher field of ~ 95 Oe. However, DW pinning at the notch did not occur during this half-cycle, and the DW instead simply passed through the notch to achieve the reversed state. The principal difference between these two situations is the relative orientation of the nucleated DW. The black DW in Figure 5.3 (V) is parallel to the front edge of the notch, whereas the black DW in Figure 5.3 (I) is not. These observations suggest that the asymmetrical DW pinning behavior is directly related to the geometry, or chirality, of the TDW relative to the notch.

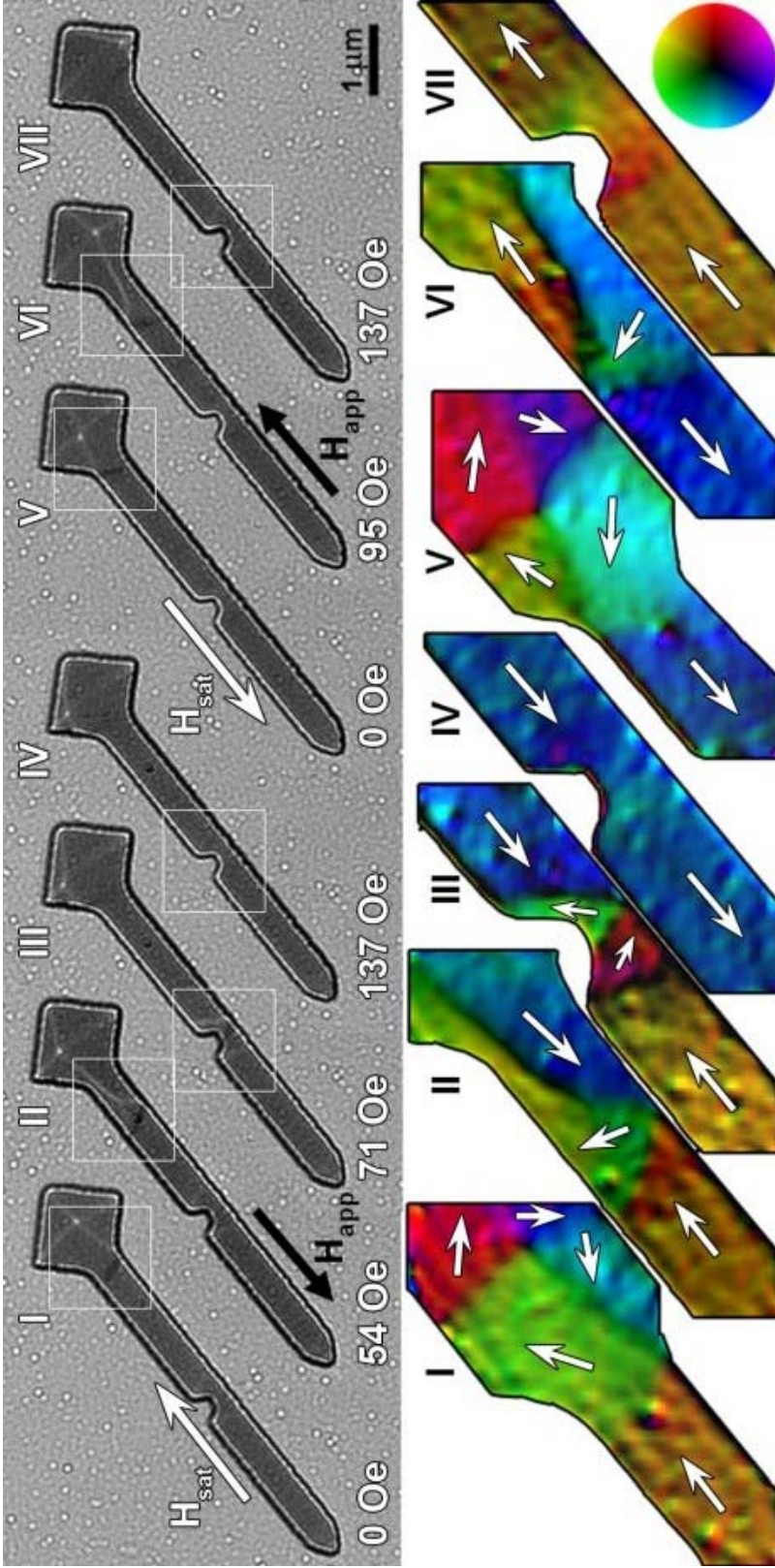


Figure 5.3. Montage showing representative states during DW motion indicated in Fresnel images (top) and corresponding magnetic induction maps (bottom), as extracted from pairs of holograms. (I) DW nucleation, (II) DW injection, (III) DW pinning, and (IV) DW depinning, during forward half-cycle. (V) DW nucleation, (VI) DW injection, and (VII) DW pass-through, for reverse half-cycle. Directions in magnetic induction maps indicated by color wheel or overlaid arrows.

Detailed schematics showing the well-defined states observed during DW propagation are sketched in Figure 5.4 (a), and the corresponding range of measured fields based on repeated observations are summarized in Figure 5.4 (c). Since one specific chirality could be obtained and retained in the pad during repeated cycles, the position and orientation of the nucleated DWs could be manipulated by controlling the saturation direction of the wire and the pad chirality. As visible in states I and V, the DW bisected the deflected magnetic flux. After injection (states II and VI), the triangular TDW had the same chirality as the pad, i.e. CW, irrespective of whether the triangular portion was downward (∇) or upward (\wedge). Due to the different local chirality, which was dependent on the saturation direction, the TDW then had two alternative behaviors. If the notch had opposite chirality, i.e. CCW in state II, the TDW could easily move to the right side of the notch due to the similarly oriented upward magnetization, but it then had to overcome the downward magnetization on the other side of the notch to pass through. In this situation, the notch effectively acted as a potential well and the TDW was trapped (state IV). Conversely, when the TDW had the same chirality as the notch (CW in state VI), it passed easily through the notch without any pinning, i.e., the notch then had no obvious effect on the wire reversal. These connections between the chiralities of the pad, TDW, and the notch, are not only limited to the observations above, but should also be applicable in more general situations, which are described in more detail in a following section.

This asymmetrical DW pinning behavior was also qualitatively predicted by simulations, as shown in Figure 5.4 (b). Some small differences between simulated and measured switching fields were observed, most likely due to local structural variations, such as defects and the notch profile. The calculated hysteresis loop indicated that an extra plateau, corresponding to the DW pinning, was present only in one half-cycle,

which could also be evident from the MOKE measurements described in Ref. [12]. The critical fields for each representative states were well-defined and distributed in a narrow range for repeated measurements, as plotted in Figure 5.4 (b). This demonstrates the reproducibility of this asymmetrical DW motion, implying possible utilization for future DW architectures, such as a logic gate.

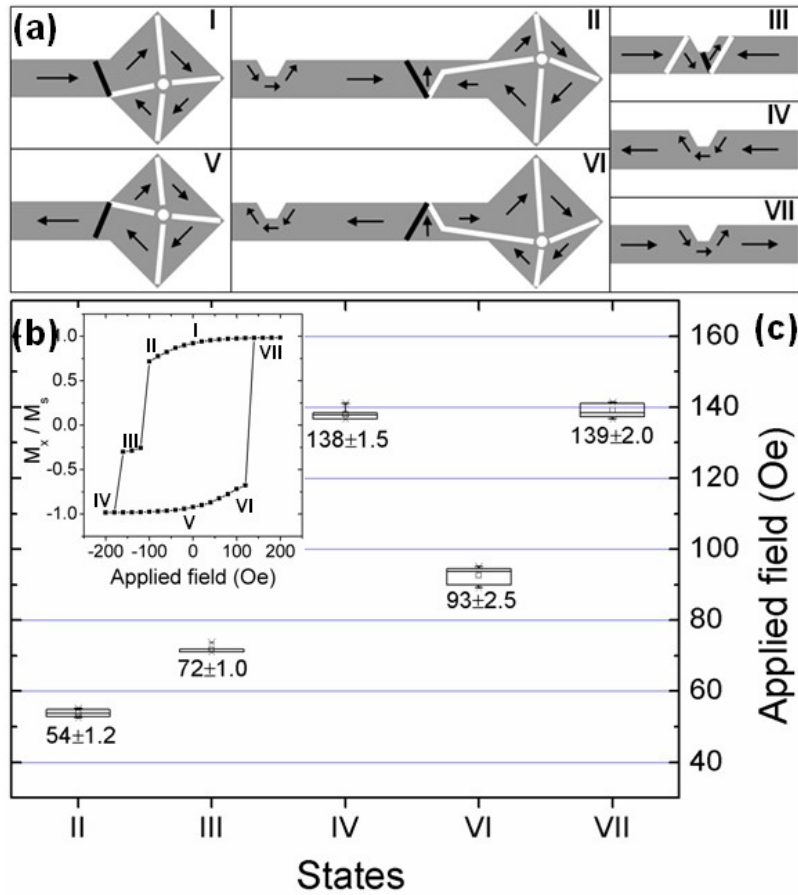


Figure 5.4. (a) Schematics of representative configurations, corresponding to states I – VII in Figure 5.3, respectively. (b) Simulated hysteresis loop showing extra plateau labeled III due to asymmetrical DW pinning during nanowire reversal. (c) Distribution of critical fields needed to emerge specific well-defined states (II, III, IV, VI, and VII) during DW propagation.

5.4. Domain Wall Relaxation and Annihilation

From the above studies, only TDWs were found during the entire DW motion. However, as shown in Figure 5.5, a transition from TDW to VDW was observed when the TDW relaxed at remanent condition after being trapped at the notch. The TDW could be successfully controlled to appear in the Py NW, and then pinned at the notch as a stable state with a certain applied field (~ 72 Oe). At this point, the in-plane magnetic field was removed and the entire NW was in the remanent condition. It was found that the DW then changed its configuration from a transverse wall to a vortex, as clearly visible as a white spot in Figure 5.5 (b). The VDW was still attached to the notch, with the vortex center set back on the reversed portion of the NW. This relaxation of the VDW is due to minimization of energy caused by the large fringing field around the notch, especially in the pinning state.

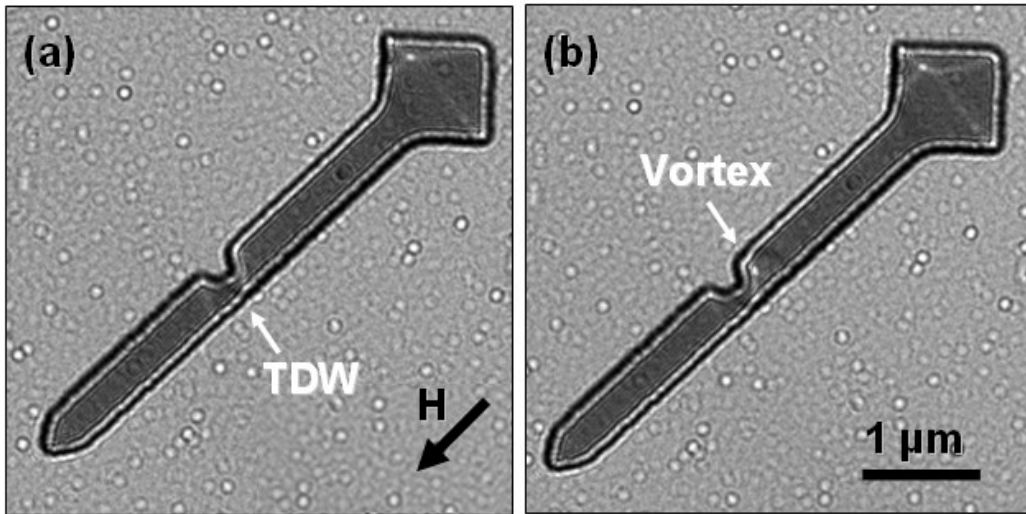


Figure 5.5. Defocused Fresnel images showing (a) TDW pinning at the notch with applied field (H) of ~ 72 Oe, and (b) relaxation of VDW at remanent state.

Micromagnetic simulations were performed using the OOMMF software in order to confirm these trends. The out-of-plane field was included in the simulations, but was found to have little effect on either the DW configurations or the switching process. Figure 5.6 compares the experimental and simulated magnetic induction maps, illustrating DW pinning at the notch [(a) and (b)], and formation of a VDW after relaxation in zero field [(c) and (d)]. These magnetization configurations, and colors between the corresponding states, match consistently except for the appearance of a little vortex core at the wire surface near the notch edge shown in Figure 5.6 (b). This transformation of a TDW to a VDW configuration after relaxation at zero field from the pinning state has not been previously reported.

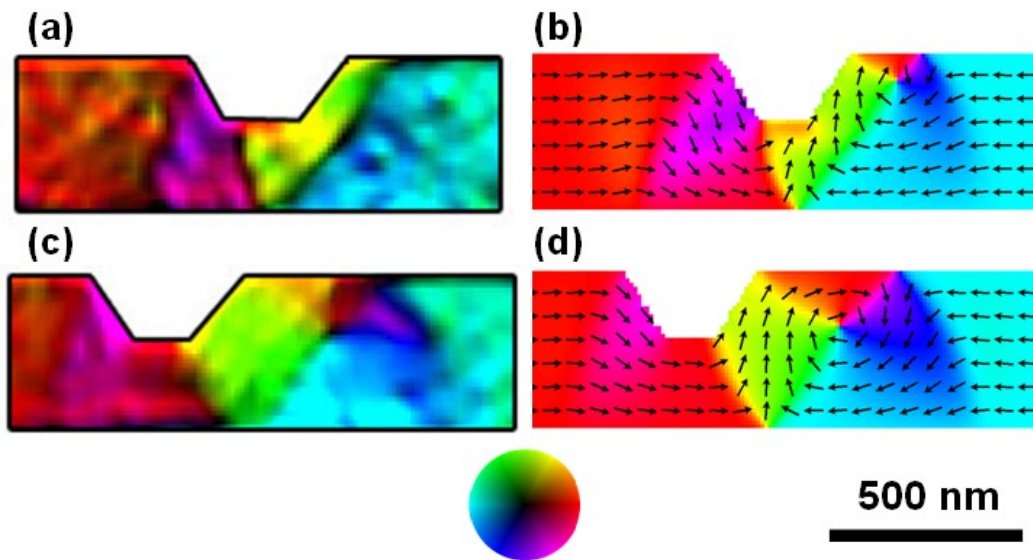


Figure 5.6. (a) Experimental, and (b) simulated, magnetic induction maps for DW pinning state. (c) Experimental, and (d) simulated, magnetic induction maps of VDW obtained after NW relaxation in zero field. Directions indicated by color wheel.

The reversed depinning behavior of DW after the pinning state was also investigated. The external field was applied along the same direction to the initial saturation field (pointing to the pad) immediately after the DW pinning at the notch. The strength of the field was gradually increased, while Lorentz images were accordingly recorded until the DW again reached the saturation state. Typical DW configurations, including pinning, depinning, attraction, and annihilation, were identified as taking place during DW annihilation, as shown in Figure 5.7 (a). Detailed magnetization distributions were quantitatively extracted from electron holograms, and then converted into magnetic induction maps, as illustrated in Figures 5.7 (b)–(e). By controlling the initial chirality of the magnetic field, the TDW could be pinned at the notch, as visible in state I of Figure 5.7 (a), and then relaxed to a VDW (not shown) at remanence. When the field was increased in the opposite direction up to ~ 56 Oe, the VDW became dissociated from the notch, forming a configuration consisting of a vortex core and an associated TDW, as shown in state II. Meanwhile, another TDW having the opposite chirality to the VDW was nucleated at the nucleation pad. As the field was further increased to ~ 91 Oe, the associated TDW moved away from the notch, while the other TDW with opposite chirality was initiated from the nucleation pad and injected into the NW: these two DWs with opposite chirality attracted each other, as shown in state III. Finally, when the applied field reached ~ 94 Oe, the two DWs annihilated to reach the saturation state of the NW, as indicated in state IV. The enlarged phase contour images and corresponding magnetic induction maps clearly indicate the detailed properties of the DWs, including configuration, chirality, and position. The correlation of the chiralities between vortex, TDWs, and nucleation pad, are crucial to their propagation.

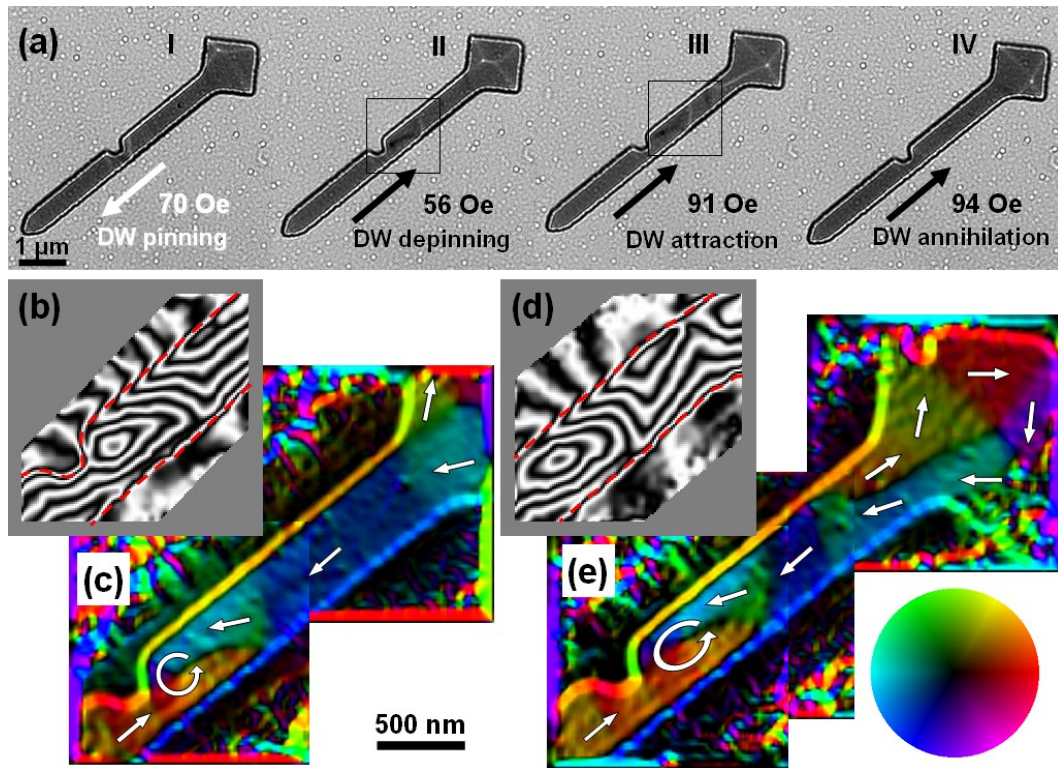


Figure 5.7. (a) Defocused Fresnel images showing representative states during DW annihilation: (I) DW pinning at the notch; (II) DW depinning from the notch; (III) two DWs attracting each other; (IV) DW annihilation. Applied field direction for each state as indicated by white and black arrows. Holographic phase image and corresponding magnetic induction map of boxed region in state II, and III, shown in (b) (c), and (d) (e), respectively. The NW profile in phase images is indicated by the red dashed lines. Magnetization directions in magnetic induction maps indicated by color wheel or overlaid arrows.

Detailed schematics showing these well-defined states observed during DW depinning and annihilation are sketched in Figure 5.8 (a), and the corresponding range of measured fields based on repeated observations are summarized in Figure 5.8 (b). The DW pinning state, as shown in state I of Figure 5.8 (a), could be obtained as the same as the state III in Figure 5.4 (a). As the applied field was switched to the opposite direction, the TDW would be dragged toward the pad direction, leaving behind a vortex core and a stretched TDW, as indicated in state II. The formed vortex had the opposite (CCW) chirality to the original TDW (CW), which might be different to the situation where the VDW was formed after enough time to ensure that the relaxation was complete. Once this CCW vortex formed, it would be stuck to the notch because both had the same

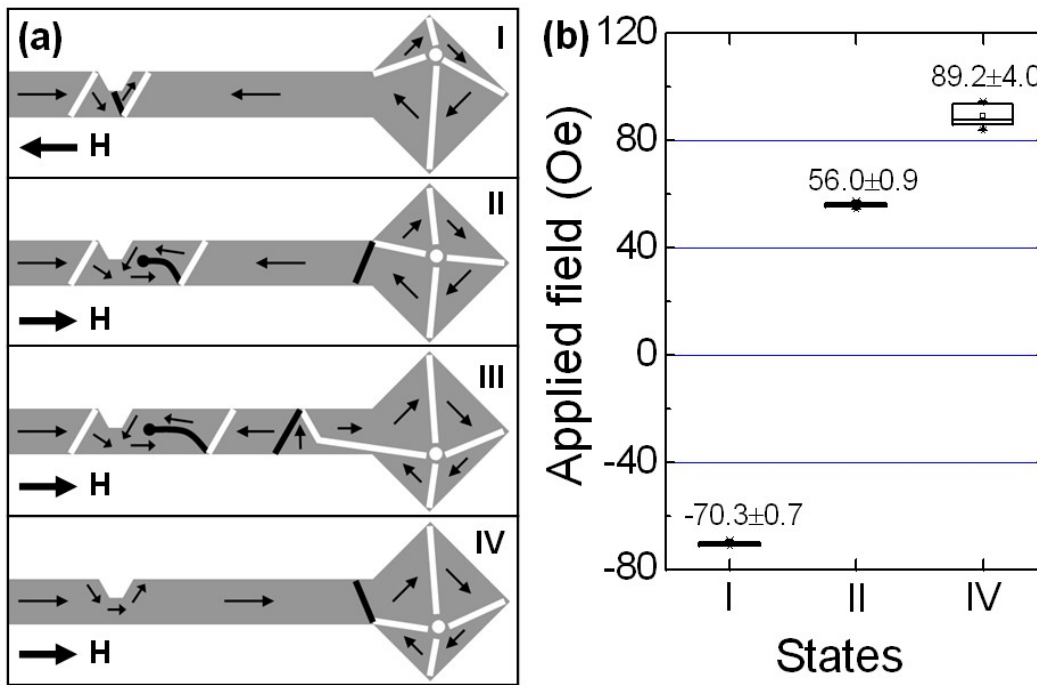


Figure 5.8. (a) Schematics of representative configurations, corresponding to states I – IV in Figure 5.7, respectively. (b) Distribution of critical fields needed to emerge specific well-defined states (I, II, and IV) during DW annihilation.

chirality, resulting in an energetically stable state. As the field increased, the TDW was extended even more and attracted to another TDW with CW chirality injected from the pad, as shown in state III. However, this state could only occasionally be recorded, since it was an unstable intermediate state which would most likely disappear in a very short period of time. When the field was large enough to overcome the attachment between the vortex core and the notch, the two TDWs would finally annihilate to achieve a saturation state exactly the same as the initial saturation. It was also found from repeated measurements that the critical fields to achieve each representative state were well defined and distributed in a narrow range, as plotted in Figure 5.8 (b). These fields were consistent with corresponding values measured from the pinning cycles of the DW motion, which demonstrates the reproducibility of DW propagation, as well as the similar effect of the notch serving as a potential well.

5.5. Discussion

The motion of DWs in Py NWs has been experimentally observed in several situations. All of these cases are systematically summarized, and discussed in a more general situation. In order to clarify the entire process of DW motion under different circumstances, as well as to illustrate the relationships between chiralities of nucleation pad, DWs, and the local notch area, a comprehensive diagram can be developed as schematically shown in Figure 5.9.

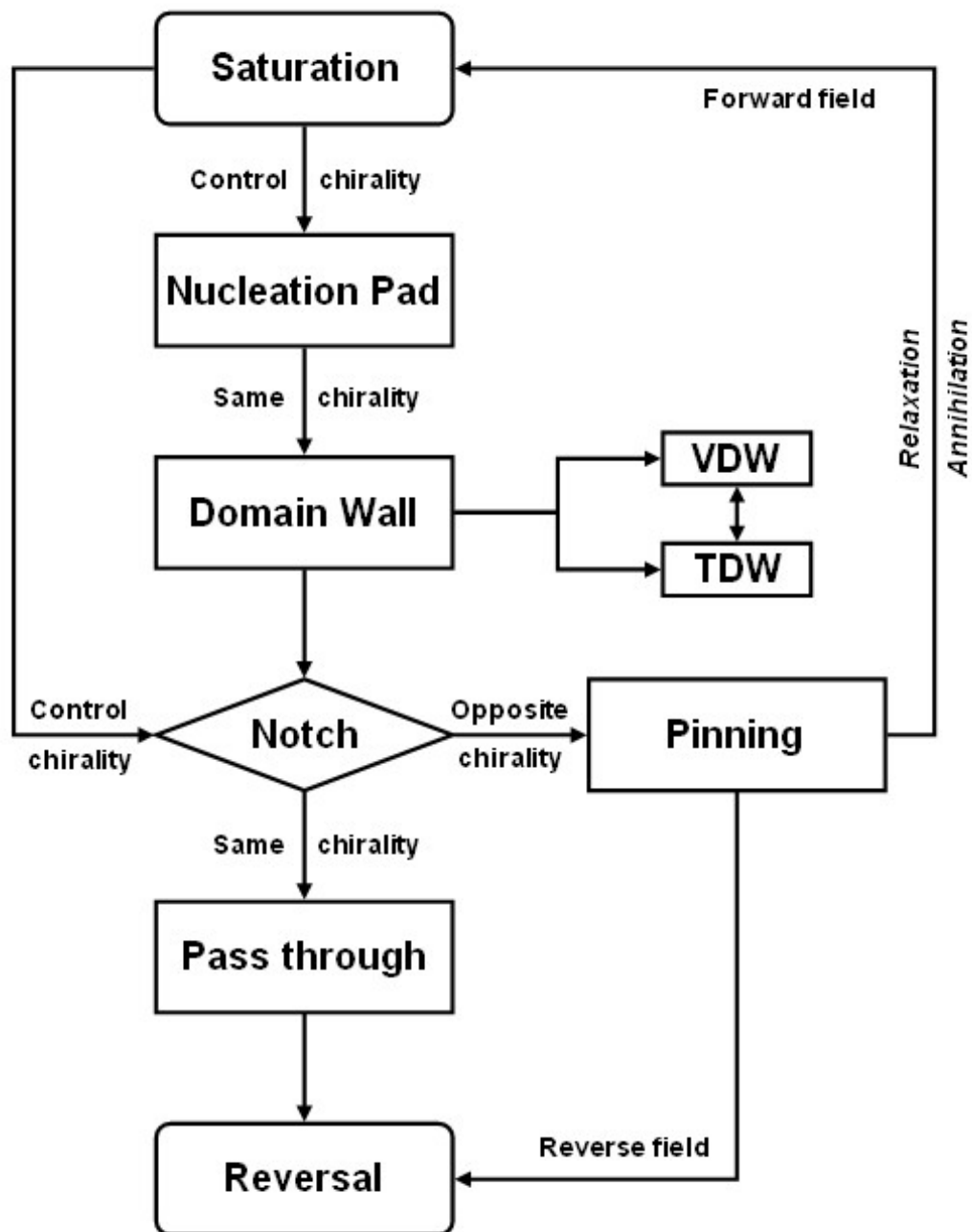


Figure 5.9. Schematic diagram illustrating the entire process and representative stages during DW propagation, also indicating correlation between chiralities of the nucleation pad, DWs, and notch.

It is apparent that the chirality of the local notch is directly determined by the direction of the initial saturation field, and the chirality of the nucleation pad can also be controlled, or at least retained, by the pad shape and the applied field. In general, the chirality of DWs is the same as the nucleation pad, regardless of their specific form, i.e., either transverse, or vortex, wall. This means that the DW chirality is, to some extent, controllable relative to the notch chirality. When a DW travels in the NW and encounters a notch, it will either simply pass through the notch if both have the same chirality, or otherwise be pinned at the notch. After the pinning state, the DW has two options depending on applied field direction. One is that the DW is released from the notch to reach reversal state, when the field is applied along the reverse direction (to the sharp tip). Conversely, when the field is applied along the forward direction (to the pad), the DW is dissociated from the notch to form a vortex core and TDW, followed by attraction and annihilation with another TDW having opposite chirality to achieve the saturation state. The two configurations of DWs, TDW and VDW, can be transformed from one to another after the pinning state, which could be determined by specific mechanisms, with no unambiguous relationship between their chiralities.

5.6. Conclusions

The motion of DWs along a Py NW with a trapezoidal notch has been observed and quantified using electron holography and Lorentz microscopy. Typical DW configurations, including nucleation, injection, pinning, depinning, relaxation, attraction, and annihilation, have been identified to take place during DW propagation.

Triangular TDWs having the same or opposite chirality as the notch, depending on the initial orientation of the nucleated DW, could be injected into the NW and then interact with the notch. The notch either served as a potential well where the TDW was

trapped, or else it had no obvious effect on the reversal process, as indicated by the pass-through of the TDW.

The TDW could be transformed to a VDW by complete relaxation in remanent condition after being pinned at the notch. The VDW could be depinned from the notch under a forward field applied toward the nucleation pad, then attracted and annihilated with another TDW with opposite chirality to reach the saturation state.

The critical fields needed to create these representative DW configurations were well defined, consistently reproducible, and distributed within a narrow range. The chiralities between the nucleation pad, DWs, and local notch, which are crucial to the DW propagation, could also be controlled by manipulating the external field and the shape of the nucleation pad. The nature of the DW properties causing this asymmetrical DW motion could be useful for future device design.

References

- [1] K. He, D. J. Smith, and M. R. McCartney, *Appl. Phys. Lett.* 95, 182507 (2009).
- [2] D. A. Allwood, G. Xiong, C. C. Faulkner, D. Atkinson, D. Petit, and R. P. Cowburn, *Science* 306, 1688 (2005).
- [3] D. A. Allwood, G. Xiong, M. D. Cooke, C. C. Faulkner, D. Atkinson, N. Vernier, and R. P. Cowburn, *Science* 296, 2003 (2002).
- [4] S. S. P. Parkin, M. Hayashi, and L. Thomas, *Science* 320, 190 (2008).
- [5] M. Hayashi, L. Thomas, R. Moriya, C. Rettner, and S. S. P. Parkin, *Science* 320, 209 (2008).
- [6] M. Hayashi, L. Thomas, R. Moriya, C. Rettner, X. Jiang, and S. S. P. Parkin, *Phys. Rev. Lett.* 97, 207205 (2006).
- [7] D. Petit, A. V. Jausovec, D. Read, and R. P. Cowburn, *J. Appl. Phys.* 103, 114307 (2008).
- [8] H. T. Zeng, D. Read, D. Petit, A. V. Jausovec, L. O'Brien, E. R. Lewis, and R. P. Cowburn, *Appl. Phys. Lett.* 94, 103113 (2009).
- [9] D. McGrouther, S. McVitie, and J. N. Chapman, *Appl. Phys. Lett.* 91, 022506 (2007).
- [10] K. J. O'Shea, S. McVitie, J. N. Chapman, and J. M. R. Weaver, *Appl. Phys. Lett.* 93, 202505 (2008).
- [11] C. W. Sandweg, N. Wiese, D. McGrouther, S. J. Hermsdoerfer, H. Schultheiss, B. Leven, S. McVitie, B. Hillebrands, and J. N. Chapman, *J. Appl. Phys.* 103, 093906 (2008).
- [12] S. Lepadatu, A. Vanhaverbeke, D. Atkinson, R. Allenspach, and C. H. Marrows, *Phys. Rev. Lett.* 102, 127203 (2009).
- [13] L. Thomas, C. Rettner, M. Hayashi, A. Doran, and A. Scholl, *Appl. Phys. Lett.* 87, 262501 (2005).
- [14] M. Y. Im, L. Bocklage, P. Fischer, and G. Meier, *Phys. Rev. Lett.* 102, 147204 (2009).
- [15] M. Kläui, H. Ehrke, U. Rüdiger, T. Kasama, R. E. Dunin-Borkowski, D. Backes, L. J. Heyderman, C. A. F. Vaz, J. A. C. Bland, G. Faini, E. Cambril, and W. Wernsdorfer, *Appl. Phys. Lett.* 87, 102509 (2005).
- [16] D. Backes, C. Schieback, M. Kläui, F. Junginger, H. Ehrke, P. Nielaba, U. Rüdiger, L. J. Heyderman, C. S. Chen, T. Kasama, R. E. Dunin-Borkowski, C. A. F. Vaz, J. A. C. Bland, *Appl. Phys. Lett.* 91, 112502 (2007).

- [17] F. Junginer, M. Kläui, D. Backes, U. Rüdiger, T. Kasama, R. E. Dunin-Borkowski, L. J. Heyderman, C. A. F. Vaz, and J. A. C. Bland, *Appl. Phys. Lett.* 90, 132506 (2007).
- [18] A. Yamaguchi, T. Ono, S. Nasu, K. Miyake, K. Mibu, and T. Shinjo, *Phys. Rev. Lett.* 92, 077205 (2004).
- [19] W. C. Uhlig, M. J. Donahue, D. T. Pierce, and J. Unguris, *J. Appl. Phys.* 105, 103902 (2009).

CHAPTER 6

SUMMARY AND FUTURE WORK

6.1. Summary

The research described in this dissertation has involved the quantitative nanoscale phase imaging of a variety of magnetic nanostructures, including patterned thin-film nanomagnets and nanowires, primarily using the technique of off-axis electron holography as well as Lorentz microscopy.

The magnetic behavior of Co nanorings and slotted nanorings, in terms of orthogonal magnetic fields applied with respect to the slot direction, has been investigated using electron holography and micromagnetic simulations. Hysteresis loops were quantitatively measured and well-defined states, including onion states, flux-closure (FC) states, and vortex formation, were identified for different types of elements, also showing excellent agreement with simulations. The Co nanorings and slotted Co nanorings with parallel fields exhibited multi-step switching behavior via onion-FC-onion mode, involving the formation and annihilation of single- or double-vortex states. In contrast, slotted rings with perpendicular fields underwent one-step switching by abrupt chirality reversal of the FC states. It was found that the chirality of the vortex (or vortices) was primarily responsible for the switching mechanism. Introduction of the slot caused shape anisotropy, which in turn affected the switching fields in terms of demagnetization energy.

Remanent magnetization configurations and switching behavior of slotted Co/Cu/Py spin-valve nanorings as a function of applied field direction relative to the slot orientation have been characterized using electron holography. At the remanent condition, the Co and Py layers would align in coupled antiparallel configurations, with

the predominant states being FC or onion when the applied field was perpendicular or parallel to the slot direction, respectively. The spin-valve nanorings exhibited multi-step switching mechanisms, which was attributed to the intrinsic coercivity differences as well as magnetic coupling between Co and Py layers. When the external field was applied perpendicular to the slot, the elements underwent a two-step hysteresis loop, corresponding to separate reversal of the Py and Co layers. When the external field was applied parallel to the slot, the spin-valve elements exhibited well-defined three-step hysteresis loops, resulting from the two-step switching of both Co and Py layers via onion-FC onion transition mechanism.

Domain-wall (DW) motion along a notched Py nanowire (NW) was directly observed and quantified using electron holography and Lorentz microscopy. Typical DW configurations, including nucleation, injection, pinning, depinning, relaxation, attraction, and annihilation, were identified to take place during DW propagation. It was found that the transverse DWs (TDWs) could interact in a different manner with the notch, depending on the relative chiralities. The notch either served as a potential well to trap TDWs with opposite chirality, or else it had no obvious effect on TDWs with the same chirality, as indicated by a simple pass-through. The TDW pinned at the notch could be transformed to VDW by complete relaxation in remanent condition, which could also be depinned from the notch and then annihilated with another TDW. The critical fields for these representative DW configurations were well-defined, consistently reproducible, and distributed over a narrow range. The correlation of the chiralities between the nucleation pad, DWs, and local notch was demonstrated, suggesting that these fundamental DW properties could be useful for future device design.

Overall, off-axis electron holography was shown to be a unique and powerful technique able to provide visualization and quantification of magnetic materials with

spatial resolution on the nanometer scale. Moreover, the combination of electron holography with Lorentz microscopy and micromagnetic simulations opens up a strong approach to explore novel magnetic materials and provide valuable insights into their important properties and behavior.

6.2. Future Work

6.2.1. Electron holography of nanomagnet arrays

The studies described in Chapters 3 and 4 have provided much useful information, in particular revealing the mechanism(s) responsible for magnetization reversal of individual ferromagnetic and spin-valve nanomagnets. However, the interaction between elements over an entire array may affect both the remanent magnetization configuration and the switching behavior, especially when the elements are densely patterned for ultra-high density recording applications. A future electron holography study could be applied to a closely spaced array of individual elements in order to understand the collective behavior, such as reproducibility of stable remanent state, switching field distribution, and fringing field over entire element arrays. Moreover, the scope of interest could be extended to other material systems, for example but not limited to, magnetic tunnel junctions (MTJ) and exchange-bias (EB) structures.

It is feasible to fabricate multilayered MTJ and EB structures using the electron-beam lithography (EBL) and sputtering systems. One challenge could be the limited region of coherent illumination which circumscribes the field of view necessary for studying the entire array. Nevertheless, several essential geometrical parameters could be adjusted to optimize the electron holography examination at lower magnification without losing much spatial resolution. Another alternative would be to scale down the dimensions of the elements, so that a larger number of elements could be recorded in

electron holograms. This approach would also provide a useful perspective for fulfilling the demand of industrial applications.

6.2.2. Current-induced DW motion

The motion of DWs driven by *in situ* magnetic fields has been successfully studied in Chapter 5. Another aspect of this subject, i.e., spin-polarized-current-induced DW motion, is of great interest for future studies involving quantitative electron holography. In order to realize this purpose, additional testing structures and on-site electrodes will need to be integrated on the silicon nitride TEM membrane windows. A special TEM sample holder capable of *in situ* application of spin currents through multiple contacts is also needed. Preliminary results are available for fabricating this type of sample. Figure 6.1 shows SEM and TEM images of such a nitride membrane sample, with two notched Py NWs on top and two pairs of gold testing electrodes attached. Special precautions need to be taken during fabrication, in order to ensure solid connection between the NWs and the electrodes, as well as proper alignment of the electrodes with the contacts of the dedicated TEM holder, as illustrated in Figures 6.2 (a) and (b).

Based on previous experience of passing current through NWs, some practical problems might be expected. One big issue is to limit the overall current density in order to avoid too much heat output that might melt the NWs or even destroy the membrane substrate. It has been suggested to apply short current pulses rather than DC currents to initiate the DW motion, as shown in Figure 6.2 (c). Another challenge is to make fast and precise measurements according to feedback from the magnetoresistance changes of the Py NW. Overall, the success of this investigation should lead to important results for both scientific and technological advances.

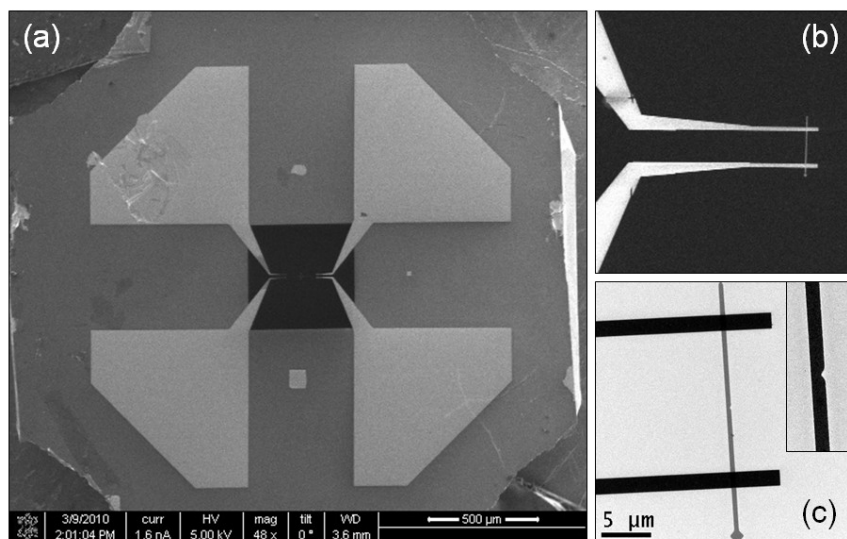


Figure 6.1. SEM images showing (a) overview, and (b) enlarged view, of Py NW with integrated testing electrodes. (c) TEM images showing a notched Py NW attached to two electrodes.

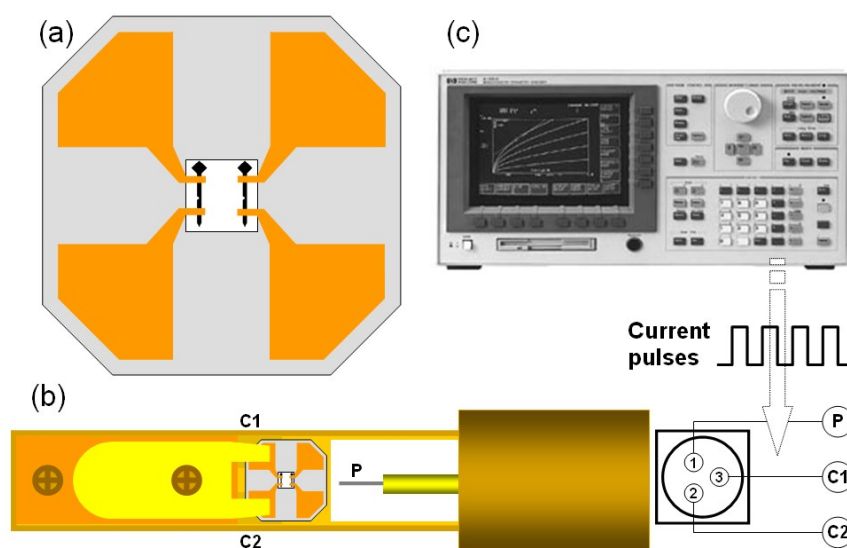


Figure 6.2. Schematics showing: (a) Py NWs with electrodes integrated on a silicon nitride membrane window; (b) *in situ* biasing TEM specimen holder having a special 2-point contact cartridge to load the membrane sample; (c) Electronic instrument to generate current pulses and measure corresponding response signals from the NW.

APPENDIX
RELEVANT PUBLICATIONS

I. Peer-Reviewed Journal Articles

- [1] **K. He**, D. J. Smith, M. R. McCartney, “Direct Observation of Magnetic Domain Wall Propagation in NiFe Nanowires”, *Microscopy and Microanalysis*, 16 (Suppl. 2), 574 (2010).
- [2] (Invited Review) M. R. McCartney, N. Agarwal, S. Chung, D. A. Cullen, M. -G. Han, **K. He**, L. Li, H. Wang, L. Zhou, D. J. Smith, “Quantitative phase imaging of nanoscale electrostatic and magnetic fields using off-axis electron holography”, *Ultramicroscopy*, 110, 375 (2010).
- [3] (Invited) **K. He**, D. J. Smith, M. R. McCartney, “Effects of vortex chirality and shape anisotropy on magnetization reversal of Co nanorings”, *J. Appl. Phys.* 107, 09D307 (2010).
- [4] **K. He**, D. J. Smith, M. R. McCartney, “Observation of asymmetrical pinning of domain walls in notched Permalloy nanowires using off-axis electron holography”, *Appl. Phys. Lett.* 95, 182507 (2009).
- [5] **K. He**, N. Agarwal, D. J. Smith, M. R. McCartney, “Vortex Formation during Magnetization Reversal of Co Slotted Nanorings”, *IEEE Trans. Magn.* 45, 3885 (2009).
- [6] **K. He**, D. J. Smith, M. R. McCartney, “Direct visualization of three-step magnetization reversal of nanopatterned spin-valve elements using off-axis electron holography”, *Appl. Phys. Lett.* 94, 172503 (2009).
[Featured as *Front Cover paper*, and selected for May 11, 2009 issue of *Virtual Journal of Nanoscale Science & Technology*.]
- [7] **K. He**, D. J. Smith, M. R. McCartney, “Remanent States and Magnetization Reversal of Nanopatterned Spin Valve Elements using Off-Axis Electron Holography”, *J. Appl. Phys.* 105, 07D517 (2009).

II. Invited and Contributed Conference Presentations (Peer-Reviewed)

- [1] **K. He**, D. J. Smith, M. R. McCartney, “Quantitative observation of vortex-controlled magnetization reversal of Co nanorings using electron holography”, 17th International Microscopy Congress (IMC17), Rio de Janeiro, Brazil, September 19–24, 2010.
- [2] **K. He**, D. J. Smith, M. R. McCartney, “Direct observation of magnetic domain wall propagation in notched permalloy nanowires using Lorentz microscopy and electron holography”, 17th International Microscopy Congress (IMC17), Rio de Janeiro, Brazil, September 19–24, 2010.
- [3] **K. He**, D. J. Smith, M. R. McCartney, “Direct observation of magnetic domain wall propagation in NiFe nanowires”, *Microscopy and Microanalysis (M&M)*

2010 Conference, Portland, OR, August 1–5, 2010.

- [4] (Invited) **K. He**, D. J. Smith, M. R. McCartney, “Effect of shape anisotropy on magnetization reversal of Co nanorings”, 11th Joint MMM-Intermag Conference, Washington, DC, January 18–22, 2010.
- [5] **K. He**, N. Agarwal, D. J. Smith, M. R. McCartney, “Vortex formation during magnetization reversal of Co slotted nanorings”, International Magnetics Conference (Intermag 2009), Sacramento, CA, May 4–8, 2009. [*Best Student Paper*]
- [6] **K. He**, D. J. Smith, M. R. McCartney, “Remanent states and magnetization reversal of nanopatterned spin valve elements using off-axis electron holography”, 53rd Magnetism and Magnetic Materials (MMM) Conference, Austin, TX, November 10–14, 2008.